FEDERAL UNIVERSITY OF SÃO CARLOS
CENTER OF EXACT SCIENCES AND TECHNOLOGY
POST-GRADUATE PROGRAM IN MATERIALS SCIENCE AND ENGINEERING

SYNTHESIS AND CHARACTERIZATION OF BIOSILICATE/F18 BIOGLASS SCAFFOLDS FOR DENTAL APPLICATION

Claudia Patricia Marin Abadia

São Carlos-SP
2019

FEDERAL UNIVERSITY OF SÃO CARLOS
CENTER OF EXACT SCIENCES AND TECHNOLOGY
POST-GRADUATE PROGRAM IN MATERIALS SCIENCE AND ENGINEERING

SYNTHESIS AND CHARACTERIZATION OF BIOSILICATE/F18 BIOGLASS SCAFFOLDS FOR DENTAL APPLICATION

Claudia Patricia Marin Abadia

Thesis submitted to the Post-graduate Program of Materials Science and Engineering (PPG-CEM/UFSCar) as a partial fulfillment of requirement for the award of the degree of DOCTOR IN MATERIALS SCIENCE AND ENGINEERING.

Supervisor: Dr. Edgar Dutra Zanotto

Co-supervisor: Dr. Murilo Camuri Crovace

Scholarship: CAPES/PROEX

São Carlos-SP
2019

DEDICATION

To my family.

VITAE OF THE CANDIDATE:

Master in Organic and Biological Chemistry of the University of São Paulo - Brazil (2014).

Bachelor in Chemistry of the University of Valle - Colombia (2007).

UNIVERSIDADE FEDERAL DE SÃO CARLOS

Centro de Ciências Exatas e de Tecnologia
Programa de Pós-Graduação em Ciência e Engenharia de Materiais

Folha de Aprovação

Assinaturas dos membros da comissão examinadora que avaliou e aprovou a Defesa de Tese de Doutorado da candidata Claudia Patricia Marin Abadia, realizada em 16/10/2019:

EDZanotto
Prof. Dr. Edgar Dutra Zanotto
UFSCar

ARodrigues
Profa. Dra. Ana Candida Martins Rodrigues
UFSCar

Profa. Dra. Marina Trevelin Souza
UFSCar

Fernanda Canduri
Profa. Dra. Fernanda Canduri
USP

Vera Lucia Arantes
Profa. Dra. Vera Lucia Arantes
USP

ACKNOWLEDGMENTS

I would like to express my gratitude to my supervisor Prof. Edgar Dutra Zanotto for the continuous support during my Ph.D. research.

I would like to express my sincere gratitude to my co-supervisor Murilo Camuri Crovace for all his important contributions to my Ph.D. research.

I would like to thank Prof. Stephanie Willerth for allowing me to do *in vitro* tests in her laboratory.

I thank prof. Dulcina Maria Pinatti Ferreira de Souza for her help with the rheological tests.

I thank all staffs of LaMaV for their collaboration during my Ph.D. research.

I thank FAPESP project number 2013/07793-6 for economic support.

I thank ELAP for the scholarship.

To CAPES - Coordenação de Aperfeiçoamento de Pessoal de Nível Superior for the financial support to carry out this work with a scholarship.

This study was financed in part by the Coordenação de Aperfeiçoamento de Pessoal de Nível Superior - Brasil (CAPES) - Finance Code 001.

My special thanks go to my family.

RESUMO

SÍNTESE E CARACTERIZAÇÃO DE ANDAIMES DE BIOSILICATE/F18 BIOVIDRO PARA APLICAÇÃO ODONTOLÓGICA

O Biovidro F18 e o Biosilicato são biomateriais com uma alta bioatividade. No entanto, os *scaffolds* de Biosilicato apresentam baixa resistência mecânica, o que impede sua aplicação clínica. Por essa razão, nosso interesse foi desenvolver *scaffolds* combinando o Biosilicato e o F18 para incrementar as propriedades mecânicas do material. Inicialmente, empregando-se os modelos de Ryshkewitch e de Ashby & Gibson, foi calculada a resistência mecânica teórica máxima de um *scaffold*. Os *scaffolds* de Biosilicato foram preparados através da técnica de réplica e, em seguida, foram recobertos várias vezes com uma suspensão de F18, de forma a eliminar defeitos e, portanto, reforçar a sua estrutura. Os *scaffolds* obtidos foram caracterizados em relação à microestrutura, porosidade total, abertura média das células e resistência mecânica à compressão. Os resultados mostraram que os *scaffolds* apresentam uma porosidade total de 82%, com abertura média de células de 525 µm e resistência mecânica à compressão de 3,3 MPa, valores compatíveis com os *scaffolds* comerciais à base de hidroxiapatita ou β-TCP. As análises de Microscopia Eletrônica de Varredura mostraram que o F18 ajudou a eliminar defeitos superficiais e infiltrou-se parcialmente na estrutura oca dos *scaffolds*, aumentando significativamente sua resistência mecânica. A diferenciação osteogênica *in vitro* de células-tronco mesenquimais foi avaliada usando os *scaffolds* de Biosilicato recobertos com Biovidrio, assim como os íons liberados pelo biomaterial. A expressão gênica foi avaliada utilizando a metodologia de PCR após 21 dias em meio osteogênico. A expressão de fatores associados à diferenciação osteogênica foram medidas usando Q-PCR. Além disso, avaliou-se a produção da enzima fosfatase alcalina e a mineralização. A atividade de diversos fatores foi significativamente aumentada na presença dos *scaffolds* ou de seus produtos de dissolução. Estes resultados mostram que os *scaffolds* desenvolvidos neste trabalho possuem grande potencial para aplicações em odontologia.

Palavras-chave: Biosilicato; Biovidro F18; *Scaffold*; Recobrimento; Diferenciação osteogênica.

ABSTRACT

In this work, Biosilicate scaffolds were synthesized using the foam replica technique. Biosilicate is highly bioactive, biodegradable, antibacterial, and non-toxic. Despite of these properties, Biosilicate scaffolds present low mechanical strength, limiting their clinical applications. Therefore, our aim was to increase the mechanical properties of the Biosilicate scaffolds by several F18 glass coatings. First, the Ryshkewitch and Ashby & Gibson models were used to calculate the maximum theoretical compressive strength of the scaffolds in function of their porosity, taking into account the ideal conditions found in the literature. Biosilicate scaffolds were prepared through the foam replica technique; then, they were coated several times with F18 Bioglass slurry to eliminate their defects and reinforce their structures. The scaffolds were characterized by microstructure, total porosity, average cell size, and compressive strength. The material exhibited a total porosity of 82%, an average cell size of 525 μm, and compressive strength of 3.3 (± 0.3) MPa, values in the range of commercial scaffolds based on Hydroxiapatite and β-TCP. Scanning Electron Microscopy showed that F18 bioglass helped to remove surface defects and partially infiltrated the hollow Biosilicate-struts, increasing significantly the resistance of the material. Also, *in vitro* osteogenic differentiation of human Adipose-derived mesenchymal Stem Cells (hASCs) was evaluated using F18 glass-coated Biosilicate scaffolds and their ionic dissolution products. Gene expression profiles of cells were evaluated using the RT^2 Profiler PCR microarray on day 21. Mineralizing tissue-associated proteins and osteogenic differentiation factor expressions were measured using Q-PCR. Additionally, alkaline phosphatase enzyme production and extracellular matrix mineralization were evaluated. The alkaline phosphatase activity, mineralization and bone-related gene expression of hASCs were significantly enhanced upon stimulation with both scaffolds and their ionic extracts. This work evidenced that F18 glass-coated Biosilicate scaffolds have a high potential for dental applications.

Keywords: Biosilicate; F18 glass; Scaffold; Coating; Osteogenic Differentiation.

PUBLICATIONS

The thesis defense was held in the modality closed to the public

Conferences:

MARIN, C.P.; CROVACE, M.C.; ZANOTTO, E.D. *Synthesis and characterization of Biosilicate/F18 bioglass composite scaffolds.* Poster presented at the 34th Annual Meeting of The Canadian Biomaterials Society. University of Victoria. Victoria, Canada. May 2018.

MARIN, C.P.; CROVACE, M.C.; ZANOTTO, E.D. *Síntesis y caracterización de compositos de Biosilicato y Biovidrio F18*. Poster presented at the 24° Congreso Asociación Latinoamericana de Operatoria Dental y Biomateriales (ALODYB). Quito, Ecuador. October 2017.

TABLE OF CONTENTS

LIST OF TABLES

LIST OF FIGURES

NOMENCLATURE - LIST OF ABBREVIATIONS

ACTB	Actin, beta
ACVR1	Activin A receptor, type I
ACVR2B	Activin receptor type-2B
AHSG	Alpha-2-HS-glycoprotein
ALP	Alkaline phosphatase
AM medium	High Glucose DMEM with glutamine, 10% FBS, and 1% Penicillin
ANXA5	Annexin A5
APS	Average particle size
ARS	Alizarin Red S
ASC	Adipose-derived stem cells
BCIP	5-Bromo-4-Chloro-3-Indolyl Phosphate
BCIP/NBT	5-Bromo-4-chloro-3-indolyl phosphate/Nitro blue tetrazolium
BGLAP	Bone gamma-carboxyglutamate protein
BGN	Biglycan
BMP	Bone morphogenetic protein
BMP1	Bone morphogenetic protein 1
BMP2	Bone morphogenetic protein 2
BMP3	Bone morphogenetic protein 3
BMP4	Bone morphogenetic protein 4
BMP5	Bone morphogenetic protein 5
BMP6	Bone morphogenetic protein 6
BMP7	Bone morphogenetic protein 7
BMPR1A	Bone morphogenetic protein receptor, type IA
BMPR1B	Bone morphogenetic protein receptor, type IB
BMPR2	Bone morphogenetic protein receptor, type II (serine/threonine kinase)
BO	Bridging oxygen
BSP	Bone sialoprotein
BTE	Bone tissue engineering
CALCR	Calcitonin receptor

$CaMgSi_2O_6$	Diopside
$Ca_2MgSi_2O_7$	Akermanite
$Ca_7MgSi_4O_{16}$	Bredigite
CDH11	Cadherin 11, type 2, OB-cadherin (osteoblast)
COL I	Collagen, type I
COL1A1	Collagen, type I, alpha 1
COL1A2	Collagen, type I, alpha 2
COL2A1	Collagen, type II, alpha 1
COL3A1	Collagen, type III, alpha 1
COL5A1	Collagen, type V, alpha 1
COL10A1	Collagen, type X, alpha 1
COL14A1	Collagen, type XIV, alpha 1
COL15A1	Collagen, type XV, alpha 1
COMP	Cartilage oligomeric matrix protein
CSF1	Colony stimulating factor 1 (macrophage)
CSF2	Colony stimulating factor 2 (granulocyte-macrophage)
CSF3	Colony stimulating factor 3 (granulocyte)
CTSK	Cathepsin K
DLX5	Distal-less homeobox 5
DMEM	Dulbecco's Modified Eagle's Medium
e-ASCs	Equine adipose-derived stem cells
ECM	Extracellular matrix
EDTA	Ethylenediamine tetraacetic acid
EDX	Energy-dispersive X-ray spectroscopy
EGF	Epidermal growth factor
EGFR	Epidermal growth factor receptor
ES	Embryonic stem
EthD-1	Ethidium homodimer-1
FA	Focal adhesion
FBS	Fetal Bovine Serum
FGF	Fibroblast growth factor
FGF1	Fibroblast growth factor 1 (acidic)

FGF2	Fibroblast growth factor 2 (basic)
FGF4	Fibroblast growth factor 4
FGF8	Fibroblast growth factor 8
FGFRs	Fibroblast growth factors receptors
FGFR1	Fibroblast growth factor receptor 1
FGFR2	Fibroblast growth factor receptor 2
FN1	Fibronectin 1
F18 glass	SiO_2-Na_2O-K_2O-CaO-MgO-P_2O_5
GAPDH	Glyceraldehyde-3-phosphate dehydrogenase
GDF10	Growth differentiation factor 10
GLI1	GLI family zinc finger 1
HA	$Ca_{10}(PO4)_6(OH)_2$
HA	Hydroxyapatite
HCA	Hydroxycarbonate apatite
hBMSCs	Human bone marrow mesenchymal stem cells
HH	Hedgehog
hMSCs	Human mesenchymal stem cells
HPRT1	Hypoxanthine phosphoribosyltransferase 1
ICAM1	Intercellular adhesion molecule 1
IGF	Insulin-like growth factor
IGF1	Insulin-like growth factor 1 (somatomedin C)
IGF2	Insulin-like growth factor 2 (somatomedin A)
IHH	Indian hedgehog
iPS	Induced pluripotent stem
ITGA1	Integrin, alpha 1
ITGA2	Integrin, alpha 2 (CD49B, alpha 2 subunit of VLA-2 receptor)
ITGA3	Integrin, alpha 3 (antigen CD49C, alpha 3 subunit of VLA-3 receptor)
ITGAM	Integrin, alpha M (complement component 3 receptor 3 subunit)
ITGB1	Integrin, beta 1 (fibronectin receptor, beta polypeptide, antigen CD29 includes MDF2, MSK12)
LLLT	Low-level laser therapy

MAPK	Mitogen-Activated Protein Kinases
MIC	Minimal inhibitory concentration
MMP2	Matrix metallopeptidase 2
MMP8	Matrix metallopeptidase 8 (neutrophil collagenase)
MMP9	Matrix metallopeptidase 9
MMP10	Matrix metallopeptidase 10 (stromelysin 2)
MODM	Mesenchymal Stem Cell Osteogenic Differentiation Medium
MSC	Mesenchymal stem cells
MSCM	Mesenchymal Stem Cell Medium
$Na_2CaSi_2O_6$	Sodium-calcium silicate
$NaCaPO_4$	Sodium-calcium phosphate
nBGs	Nano-bioactive glass
NBT	Nitroblue Tetrazolium
NFKB1	Nuclear factor of kappa light polypeptide gene enhancer in B-cells 1
NOG	Noggin
1N2C3S	Soluble non-phosphate crystal phase
OCN	Osteocalcin
PBS	Phosphate buffered saline
PDGFA	Platelet-derived growth factor alpha polypeptide
PHEX	Phosphate regulating endopeptidase homolog, X-linked
PLLA	Poly (L-lactide acid)
*p*NP	p-Nitrophenol
pNPP	p-Nitrophenyl phosphate
ppi	Pores per inch
RGD	Argenine, glycine and aspartic acid (Arg-Gly-Asp)
RPLP0	Ribosomal protein, large, P0
RUNX2	Runt-related transcription factor 2
SBF	Simulated body fluid
SEM	Scanning electron microscopy
SERPINH1	Serpin peptidase inhibitor, clade H (heat shock protein 47), member 1, (collagen binding protein 1)

Si-CaP	Silicate-substituted calcium phosphate
SMAD1	SMAD family member 1
SMAD2	SMAD family member 2
SMAD3	SMAD family member 3
SMAD4	SMAD family member 4
SMAD5	SMAD family member 5
SOX9	SRY (sex determining region Y)-box 9
SP7	Osterix
SPP1	Osteopontin
TEM	Transmission Electron Microscopy
TGFB1	Transforming growth factor-beta 1
TGFB2	Transforming growth factor, beta 2
TGFB3	Transforming growth factor, beta 3
TGFBR1	Transforming growth factor, beta receptor 1
TGFBR2	Transforming growth factor, beta receptor II (70/80kDa)
TNF	Tumor necrosis factor
TNFSF11	Tumor necrosis factor (ligand) superfamily, member 11
TRIS	Tris-(hydroxymethyl)
TWIST1	Twist homolog 1 (Drosophila)
VDR	Vitamin D (1,25- dihydroxyvitamin D3) receptor
VEGF	Vascular endothelial growth factor
VEGFA	Vascular endothelial growth factor A
VEGFB	Vascular endothelial growth factor B
WNT	Wingless-int
XRD	X-ray Powder Diffraction

1 INTRODUCTION AND OBJECTIVES

The modern lifestyle has created certain habits in the population and work environments that have increased accidents, obesity, as well as life expectancy. This has produced great clinical demand in joint and bone repair as a result of trauma or chronic diseases. Worldwide, approximately 15 million bone fracture cases are estimated annually, where 9.0 million correspond to osteoporotic fractures. Moreover, it has been found that one of the most frequently transplanted tissue is bone, reaching costs of up to $3.3 billion (JOHNELL; KANIS, 2004; LIU; LIM; TEOH, 2013).

Many surgical procedures related to these problems result in the partial excision of the bone, and the amputated part is frequently replaced by an autograft or allograft bone tissue and prosthetic implants (KRETLOW; MIKOS, 2007; LIU; LIM; TEOH, 2013; PROSECKÁ et al., 2015). The standard tissue utilized in these treatments is autograft tissue, which is normally extracted from the iliac crest of the patient and presents both osteoconductive and osteoinductive properties as well as non-immunogenicity. However, this procedure has certain drawbacks, such as donor site morbidity, limited supply, and high cost. Another important clinical option is allograft bone, which became relevant due to its abundant source. In spite of that fact, its usage is restricted by possible disease transmission, risk of an immune reaction, toxicity due to its sterilization, and non-optimal interaction between the body and the implanted materials (KRETLOW; MIKOS, 2007; PROSECKÁ et al., 2015).

Each year, the world’s population increases profusely, and the future demand for tissue replacement will be proportional to the overpopulation. Consequently, it is necessary to develop new therapies that overcome the drawbacks of autografting and allografting. Advances in this field could improve the clinical outcomes of implantation and patients´ quality of life (GHOLIPOURMALEKABADI et al., 2015; STEVENS et al., 2008).

Tissue engineering is a new research field, whose goal is to assist in either repairing or replacing damaged or lost tissue/organs. Frequently, in this kind of treatment is used a scaffold, a three-dimensional structure that facilitates maintenance, restoration or enhancement of organ function of the patient (HOPPE; GÜLDAL; BOCCACCINI, 2011).

All tissues and organs are composed of a mixture of cells and non-cellular components that are bound, establishing well-organized networks named extracellular matrices (ECMs); the ECM is the place where cells dwell in all organs and tissues. The non-cellular three-dimensional macromolecular network is composed of collagens, proteoglycans, glycosaminoglycans, elastin, fibronectin, laminins, and different glycoproteins, whose structures and chemical compositions rely on the specific tissue (Figure 1.1). Several functions including cell survival, growth, migration, differentiation, and normal homeostasis are controlled by cellular signals. In addition, this deeply dynamic structure gives physical support to the tissues and remodels itself by means of matrix-degrading enzymes in both normal and pathological states (DONG; YONGGANG, 2016; THEOCHARIS et al., 2016).

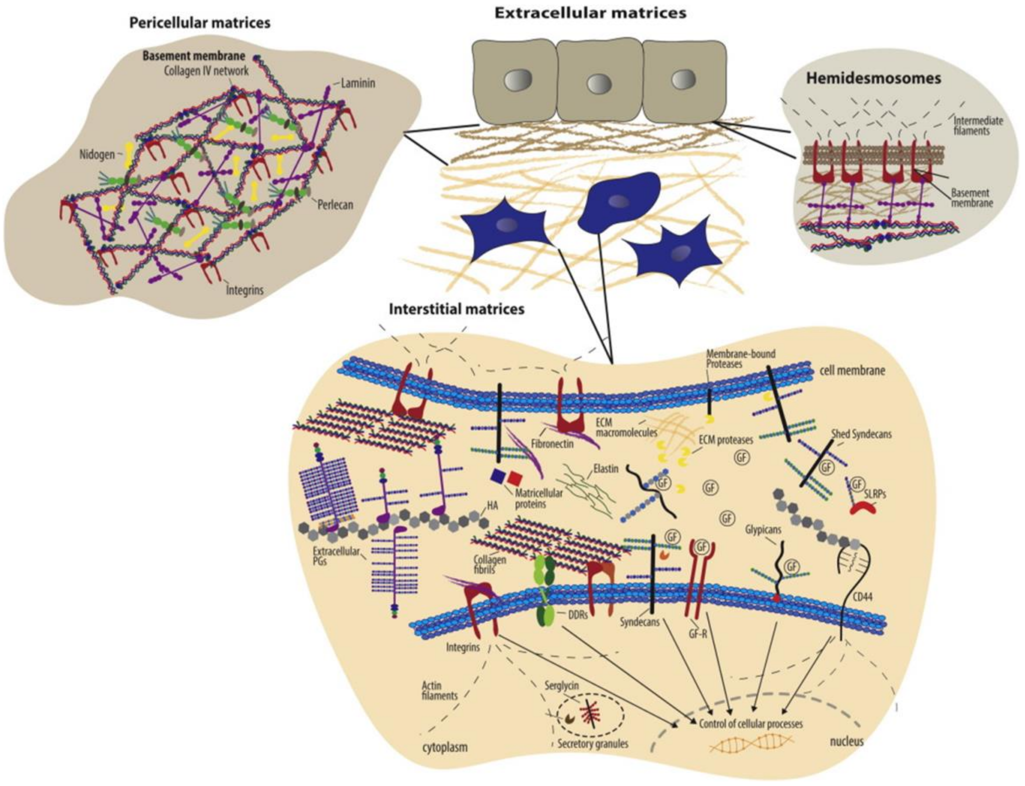

Figure 1.1 - Schematic overview of extracellular matrices, their major components, and cell surface receptors (THEOCHARIS et al., 2016).

Since scaffolds for bone regeneration have to simulate bone morphology, structure, and function, different strategies have been used to produce scaffolds that mimic the micro/nanostructure and chemical composition of the ECM of the injured tissue or organ to repair (DONG; YONGGANG, 2016; MAJI et al., 2016; THEOCHARIS et al., 2016). The three-dimensional porous structure of a scaffold has to offer a suitable environment to stimulate cell function and viability while the cell-specific functions are maintained. Factors such as angiogenesis are vital, since neovascularization encourages regenerating and growing of the tissue; on the contrary, if the cells are located more than a few hundred micrometers of the blood vessels, they can die for deprivation of oxygen supply inhibiting tissue growth. Overall, almost all synthetic and natural materials show restricted angiogenesis, so there is much interest in creating materials with neovascularization (GORUSTOVICH; ROETHER; BOCCACCINI, 2010; MAJI et al., 2016). To mimic the ECM of bone, scaffolds should exhibit other important properties such as biocompatibility with the host tissue, osteoconduction, osteoinduction, appropriate porosity, controlled biodegradability, and optimal mechanical strength. Biodegradability is one of the most attractive characteristics of the scaffold, since its degradation in the body and posterior excretion avoid a second surgery to remove it from the body. Another key point is the architecture of the scaffold that defines the geometry of the neotissue (COSTA-PINTO; REIS; NEVES, 2011; KIM et al., 2014; MAJI et al., 2016).

An ideal scaffold must stimulate differentiation of immature progenitor cells down an osteoblastic lineage (osteoinduction), foster the ingrowth of surrounding bone (osteoconduction), and permit integration into the surrounding tissue (osseointegration), avoiding micromotion and encouraging homogeneous tissue neoformation (KRETLOW; MIKOS, 2007; MATASSI et al., 2011).

Bone tissue engineering (BTE) has used different biomaterials, including biopolymers, metals, bioceramics, and composites to satisfy all design criteria. Each one of them possesses individual characteristics that can be exploited to enhance cellular adhesion and proliferation, which stimulate the healing process. Different methods have been adopted to control the biodegradability, mechanical properties, and biocompatibility of scaffolds to reach the optimal design criteria. Among these techniques, it can be mentioned foam replication, sol-gel foaming, electro-spinning, or additive manufacturing methods (HOPPE; GÜLDAL; BOCCACCINI, 2011).

Scaffolds for bone regeneration must mimic bone morphology, structure, and function in order to allow integration to the surrounding tissue. The structure of human bone is formed by hydroxyapatite (HA) ($Ca_{10}(PO_4)_6(OH)_2$) crystals, which are deposited in the organic matrix composed of 95% of type I collagen, and it can be found in microstructures such as cortical bone, cancellous bone, periosteum, endosteum, and articular cartilage. Cortical bone encompasses 80% of bone mass and has 3-12% porosity, created by the set of voids of this solid structure (Figure 1.2a and 1.3). On the other hand, cancellous bone exhibits an open, honeycomb structure with 50-90% porosity and represents about 20% of bone mass (Figure 1.2b and 1.3) (KARAGEORGIOU; KAPLAN, 2005; WU et al., 2014).

Regarding their mechanical properties, the Young's modulus of cortical bone is sufficiently high to bear the weight of the bone, whereas the Young's modulus for cancellous bone is much lower than for cortical bone, but its special alignment allows softening sudden stress (WU et al., 2014). Bone is constituted by a variety of cells such as osteoblasts, osteoclasts, osteocytes, and bone lining cells. In addition, it is a dynamic structure that constantly mineralizes a new tissue and remodels the bone matrix. In the same way, bone counts on hormones and cytokines, which help to regulate bone metabolism, function, and regeneration.

Among the materials that have chemical similarity to the inorganic phase of bone can be mentioned HA, Bioglass, A-W glass-ceramic, and β-tricalcium phosphate, which exhibit faster adhesion and proliferation of osteoblastic cells than other materials such as Ti (STEVENS et al., 2008). When materials such as bioactive glasses are used for bone repair, it has been observed a rapid bone regeneration emulating the architecture and mechanical properties of injured bone (HENCH, 2002). One explanation to this phenomenon is that these bioactive materials have both osteoconductive and osteoinductive properties. In contrast, materials such as calcium phosphate exhibit osteoconduction, but their osteoinductive properties can be deficient (CROVACE et al., 2016; JONES; GENTLEMAN; POLAK, 2007). This material quickly dissolves, producing an unstable interface that generates a loss of mechanical strength; conversely, the glasses form a hydroxycarbonate apatite layer (HCA) between the surrounding tissue and the scaffold creating a stable interface (HENCH, 2002; KNOWLES, 2003; TILOCCA, 2009). Other important material is Biosilicate, this highly bioactive biomaterial is composed of a group of fully crystallized glass-ceramics of the Na_2O-CaO-SiO_2-P_2O_5 system, which in contact with “simulated body fluid” (SBF) forms a HCA layer in approximately 24 hours (RENNO et al., 2013). For all of these reasons, these materials have been intensively researched in bone tissue engineering applications, as well as composites based on apatite crystals and natural biopolymers. In spite of these advances, further researches are necessary to improve the material performance in BTE (GHOLIPOURMALEKABADI et al., 2015; MAJI et al., 2016; STEVENS et al., 2008). Even though bioglasses have high bioactivity, they exhibit low mechanical properties, making difficult their application in BTE. Thus, several studies have been carried out to find methods that increase their mechanical strength (RENNO et al., 2013).

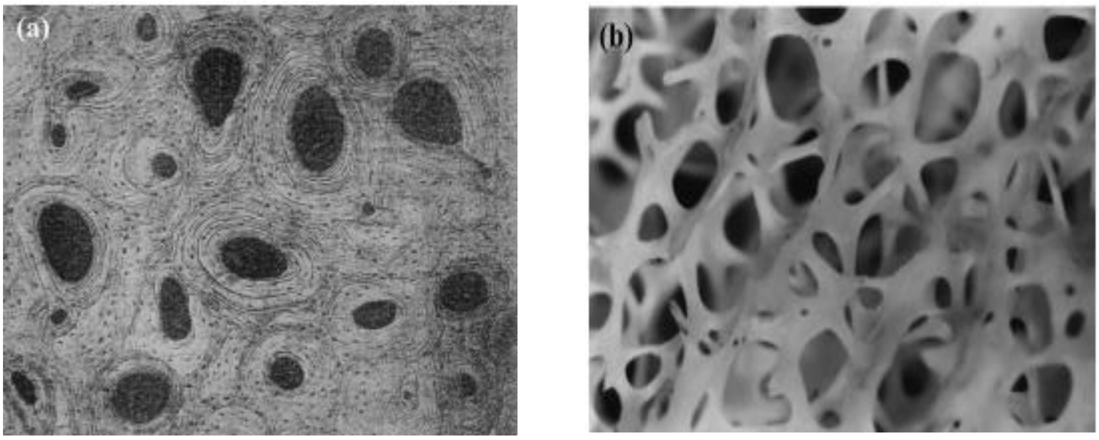

Figure 1.2 - Bone morphologies: (a) optical micrograph of a transverse cross-section showing the microstructure of compact lamellar bone-human femora; (b) SEM image of cancellous bone (WU et al., 2014).

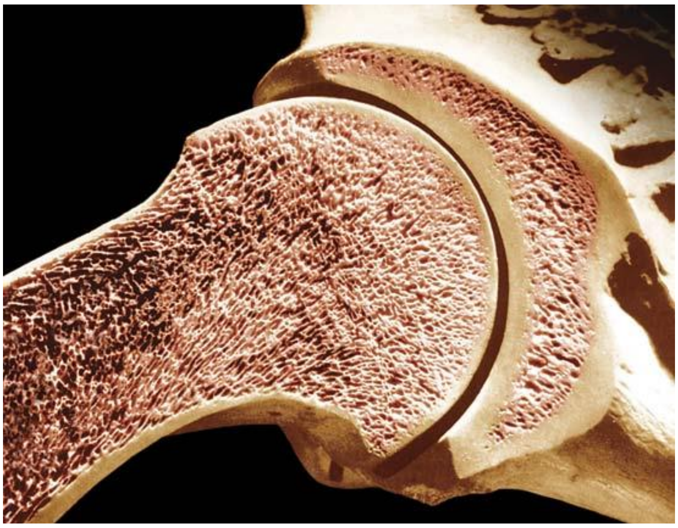

Figure 1.3 - Structure of bone, showing both cortical and trabecular bones. Source: Britannica Academic.

1.1 Objectives

The main objective of this thesis was to obtain macroporous (porosity > 80%, cell size > 300 μm) and mechanically competent (compressive strength > 3 MPa) F18 glass-coated Biosilicate scaffolds.

In vitro evaluation of osteogenic differentiation of human Adipose-derived Mesenchymal Stem Cells was done using F18 glass-coated Biosilicate scaffolds and their ionic dissolution products by Q-PCR.

2 LITERATURE REVIEW

2.1 Biomaterials

Synthetic biomaterials for bone grafting can be classified as first, second, and third-generation biomaterials and their differences rely on the strength of the response that the implant shows when this is exposed to body fluids (TILOCCA, 2009). First-generation biomaterials were created in 1960, and since then, they have been used in several million of implantations. In general, they are metals and alloys (Ti, stainless steel); and dense or porous ceramics (alumina, zirconia). One of their characteristics is that they are biologically inert due to their lacking or weak interaction with the surrounding tissues, generating a minimal toxic response in the patient.

Second-generation biomaterials are classified as bioactive or resorbable materials, such as new compositions of ceramics, glasses, and glass-ceramics (SOUZA et al., 2017; TILOCCA, 2009).

“A bioactive material is one that elicits a specific biological response at the interface of the material which results in the formation of a bond between the tissues” (WANPENG; HENCH, 1996). For instance, when bioactive glasses interact with the tissue and body fluids, they quickly form a HCA layer in the interface between the material and the tissue, increasing the interfacial adhesion of the implant and limiting the material reactivity to the surface, which avoids that the bulk material degrades rapidly. This mechanism permits creating a long-lasting stable interface, which increases cellular interaction and regulate growth of mature tissues (TILOCCA, 2009).

Bioactive materials, such as bioactive glasses, ceramics, glass-ceramics, and composites, began to have different orthopedic and dental applications in 1980 (HENCH, 2002; TILOCCA, 2009). Resorbable materials, such as crystalline or amorphous calcium phosphates, are quickly dissolved in contact with the body fluids, and the void spaces formed in the structure will be gradually replenished with living tissue (KNOWLES, 2003). When the material dissolves, the implant begins to lose mechanical strength, generating an unstable interface, that causes patient immobilization for a long time (KNOWLES, 2003; TILOCCA, 2009). The ideal graft should have a degradation rate synchronized with the formation of the neoformed bone tissue (SABIR; XU; LI, 2009).

Even though the first and second-generation biomaterials have constituted important solutions for diverse clinical problems, these implants can fail for some applications, normally in 10 to 25 years, being necessary a surgical intervention to remove them (HENCH, 2002). So many economic and scientific efforts have been carried out to improve the performance of these biomaterials without ideal outcomes.

Biological tissues are able to react to dynamic loads or biochemical stimuli; this feature is absent in first and second-generation biomaterials restricting their lifetime (HENCH, 2002). Since it is necessary to produce a more biologically based method, the interest in developing third-generation biomaterials has arisen, which foster specific cellular responses at the molecular level (HENCH, 2002; SOUZA et al., 2017). These kinds of biomaterials are characterized for possessing both bioactivity and bioresorbability as well as better clinical results (SOUZA et al., 2017). Third-generation bioactive glasses permit activating genes that encourage regeneration of living tissues conserving the architecture and mechanical properties of injured bone. Their osteoconductive and osteoinductive properties are related to the release of ionic dissolution products during the degradation process, which generate intracellular and extracellular responses in the interface (HENCH, 2002). This process is linked to the differentiation and proliferation of osteoblasts. When primary human osteoblasts are in contact with ionic dissolution products, seven families of genes are activated and upregulated in only 48 hours; thus, osteoblasts go through cell division, and extracellular matrix is synthesized, resulting in mineralization that leads to the formation of new bone tissue (HENCH, 2002; XYNOS et al., 2001).

Bioglasses can be obtained from different glass systems, being the most common, silicates, borates, and phosphates (RAHAMAN; DAY; BAL, 2011). The amorphous structure of silicate glasses is formed by a network of covalent SiO_4 tetrahedral building blocks, which are maintained together by bridging oxygen (BO) atoms (TILOCCA, 2009). This system presents a short-range order that is composed of tetrahedra and is similar to the crystalline systems. In addition, there is a long-range disorder, whose disorder degree is determined by the high flexibility that exists between the angle formed by bridged tetrahedra and their specific orientation. This 3D amorphous structure is a continuous network, where each tetrahedron is linked to other four tetrahedra by BOs. When alkali or alkaline-earth metal cations, known as “modifier” cations, interact with silicate, these break the Si-O-Si bridge bonds, and, hence oxygen acquires a negative charge and forms ionic bonds with the modifier cations. This permits maintaining the overall charge neutrality of the system and reducing the sintering temperature. Despite the fact that these ionic bonds are weaker than Si-O-Si covalent bonds, these types of bonds are very important to stabilize ‘invert’ glasses such as bioactive glasses (Figure 2.1) that are constituted for low silica amounts and contain fewer oxygen atoms as BOs. This ionic interaction is vital for the formation of a stable glass containing high amount of chain-like fragments (Figures 2.1 and 2.2) (TILOCCA, 2009).

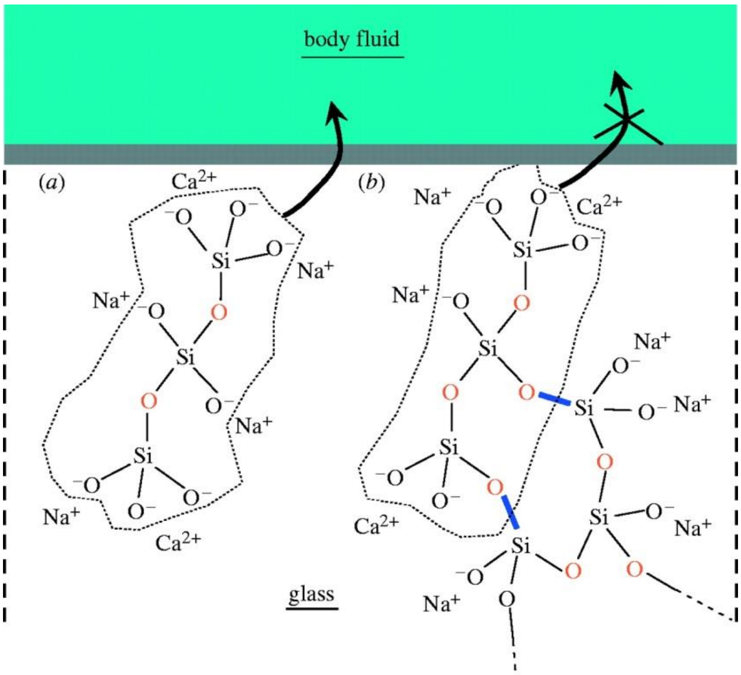

Figure 2.1 - General scheme of the chemical structure of bioactive glasses; BOs are drawn in red. The fragment in (a) is a three-membered silicate chain, there are no covalent bonds to the remains of the structure, and the dissolution will be faster than that of the fragment in (b), which is part of a five-membered ring and

covalently cross-linked by the additional Si-O bonds drew in blue (TILOCCA, 2009).

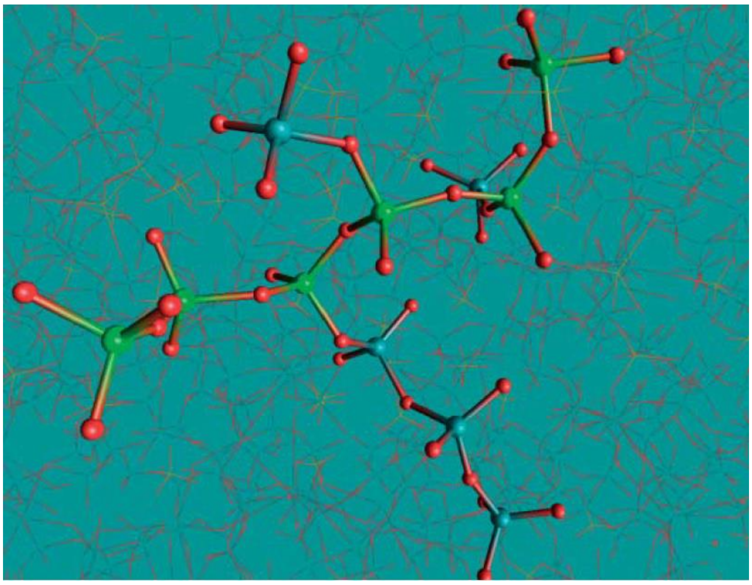

Figure 2.2 - The silicate 3D network of 45S5 Bioglass. Na^+ and Ca^{2+} ions are not drawn for clarity. Ball-and-stick representation is used to point out one silicate chain fragment, with Si atoms colored in light blue and green (TILOCCA, 2009).

2.2 Key factors concerning scaffolds for use in tissue engineering: design criteria

The main goal of tissue engineering is to repair, replace, preserve, or enhance the function of a specific tissue or organ. The ideal scaffold for BTE should function as a template for tissue growth in three dimensions, providing an interconnected macroporous network with an appropriate pore size distribution that promotes vascularization, nutrient delivery, and discharge of metabolic waste. Moreover, its interaction with the cells should encourage cell adhesion, proliferation, migration, differentiated cell function, and no scar tissue. Ideally, the scaffold has to be degradable and resorb at the same rate as tissue regeneration. Also, it has to be strong enough to avoid the breakdown of the porous structure and the loss of the predesigned tissue structure during tissue neoformation. Finally, the scaffold should be non-toxic to cells and have a high surface area (JAYAKUMAR et al., 2010; PARK et al., 2014; VATS et al., 2003).

In section 2.2.1 to 2.2.4, a brief description of these basic requirements of a scaffold to be effective in bone regeneration:

2.2.1 Bioactivity

Scaffolds can establish a dynamic interaction with endogenous or exogenous cellular components, which facilitates molecular and mechanical signaling system, encouraging cell adhesion, proliferation, and migration *in vitro* culture and *in vivo* implantation (CHAN; LEONG, 2008; ZOHORA; YOUSUF; ANWARUL, 2014). Ideally, the scaffold should not generate toxic agents during its degradation or cause any immune response that can interfere with the healing process or induce rejection by the body (ZOHORA; YOUSUF; ANWARUL, 2014). Certain techniques allow biocompatibility to be improved through surface modifications, redefining the hydrophilicity of the material or functionalizing the surface with charged groups, peptides, or proteins (MITRA et al., 2013). It has been evidenced that nanoscale alterations in topography influence over different cell functions, which are related to coordinate transcriptional activity and gene expression (MITRA et al., 2013). Another important factor for osteogenesis is the surface roughness of biomaterials since this can increase attachment, proliferation, and differentiation of cells (CUI et al., 2017; KARAGEORGIOU; KAPLAN, 2005). The scaffold can also increase the regeneration by exogenous growth-stimulating signals such as growth factors (CHAN; LEONG, 2008). To analyze the biocompatibility of the scaffold, some assays can be used to evaluate factors such as biocompatibility, which measures the cell cytotoxicity that cell cultures can undergo *in vitro*; immunogenicity, which studies the immune response against these materials; and biodegradability to estimate cell behavior in the presence of degradation products (HUSSEIN et al., 2016).

Other important factors are osteoconduction and osteoinduction. Osteoconduction is the process that allows bone growth along the graft surface, this phenomenon is regularly observed in the case of bone implant and requires contact between the host bone and the graft; osteoinduction implies the recruitment of immature cells that encourages the generation of new bone on the implant surface; but, in contrast to osteoconduction, the graft surface does not need to be in contact with the host bone because bone cells or their progenitor emit signals that stimulate bone formation anywhere in the biomaterial (CROVACE et al., 2016; JONES; GENTLEMAN; POLAK, 2007). Bioactive ceramics based on calcium phosphate possess osteoconduction, although these materials have less or absent osteoinduction. On the contrary, bioactive glasses exhibit both properties; this is important because osteoinduction provides adequate conditions for bone regeneration (CROVACE et al., 2016; JONES; GENTLEMAN; POLAK, 2007).

Bioactive glasses can be classified such as melt-derived and sol-gel derived. Melt-derived glasses are principally quaternary such as Bioglass® (24.4-Na_2O-26.9%CaO-46.1SiO_2-2.5P_2O_5, mol%). Bioglass® can be cast into several shapes or powder sizes and is found commercially as Novabone (US biomaterials) (VATS et al., 2003). These materials have different applications in tissue engineering because they are able to support vascularization *in vivo* and *in vitro* (HOPPE; GÜLDAL; BOCCACCINI, 2011); stimulate osteoblast adhesion, growth, and differentiation; induce differentiation of mesenchymal cells to osteoblasts; are able to bond with soft and hard tissue; and generate a HCA layer when they are in contact with biological fluids, this induces a strong bond between bioactive glasses and human bone (CROVACE et al., 2016; HENCH, 2013; HOPPE; GÜLDAL; BOCCACCINI, 2011; JONES; GENTLEMAN; POLAK, 2007). Equally, their ionic dissolution products such as Si^{4+}, Ca^{2+}, and PO_4^{3-} promote the expression of different genes of osteoblastic cells and other biological responses (Figure 2.3) (HOPPE; GÜLDAL; BOCCACCINI, 2011).

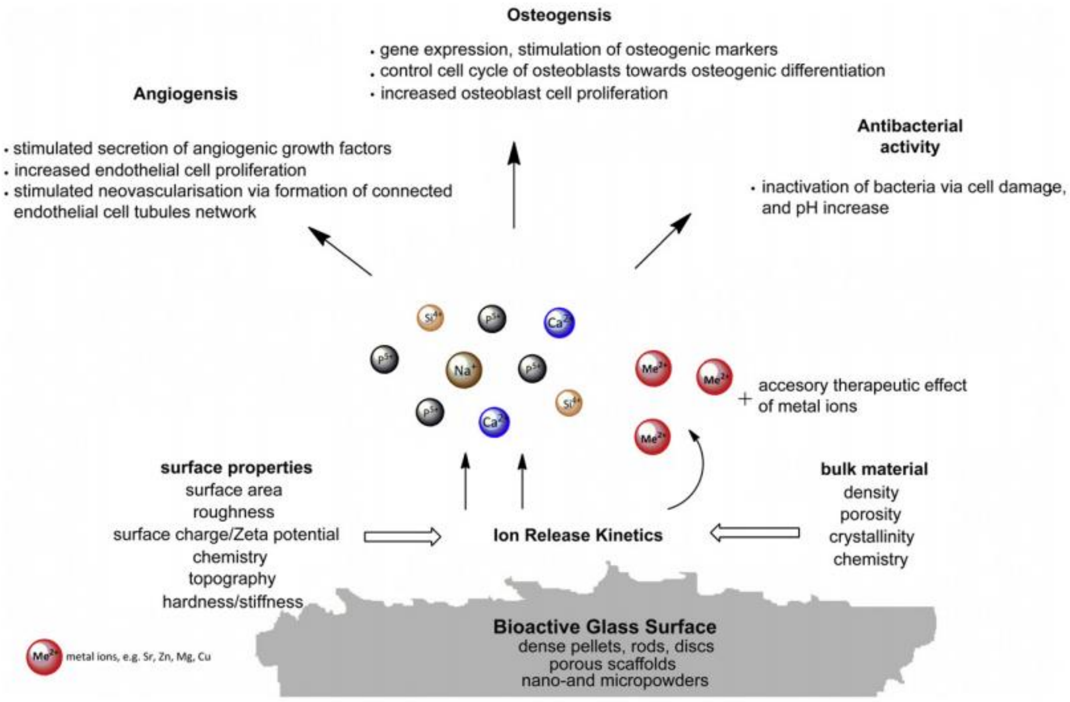

Figure 2.3 - Sketch of biological responses to ionic dissolution products of bioactive glasses (HOPPE; GÜLDAL; BOCCACCINI, 2011).

The osteoinduction mechanism is not totally elucidated. Nevertheless, some studies have shown that during bioglass degradation, phosphate groups and ions such as silicon, calcium, and sodium are released, stimulating the formation of bone tissue (JONES; GENTLEMAN; POLAK, 2007; RENNO et al., 2013). Hench *et al.* proposed a set of reactions to explain the formation of the HCA layer that leads to the generation of a strong bond between bioactive glass and living tissue (HENCH, 2013; JONES; GENTLEMAN; POLAK, 2007). This process can be summarized in 5 stages:

Stage 1: When the glass is in contact with body fluids, Na^+ and Ca^{2+} ions are released into the fluid. And, in this rapid ionic exchange, alkali and alkali earth ions are substituted in the glass structure for H^+ ions from the fluid. This reaction generates that the local pH augments since H^+ ions in the solution are being replaced by cations. This basic medium generates the hydrolysis of the silica groups (JONES; GENTLEMAN; POLAK, 2007).

$$Si - O - Na + H^{+} \rightarrow Si - OH + Na_{aq}^{+}$$

Stage 2: The OH^{-} ions produced during stage 1 attack the silica glass network, which breaks Si-O-Si bonds, causing the continuous generation of Si-OH (silanols) at the glass-solution interface. Thus, soluble silica leaves the glass structure in the form of $Si(OH)_4$ (CROVACE et al., 2016; JONES; GENTLEMAN; POLAK, 2007).

$$Si - O - Si + H_2O \rightarrow Si - OH + OH - Si$$

Stages 3 to 5: If the pH of the solution is less than 9.5, the condensation of $Si(OH)_4$ occurs forming a polymerized silica-rich layer on the glass surface, which is depleted in Na^{+} and Ca^{2+} ions (stage 3). Then, Ca^{2+} and PO_4^{3-} ions in the glass move to the surface through the open silica-rich layer and together with Ca^{2+} and PO_4^{3-} ions present in body fluids generate an amorphous CaO-P_2O_5 rich film over the silica-rich layer (stage 4). Subsequently, CaO-P_2O_5 film incorporates OH^{-} and CO_3^{2-} anions from solution, giving rise to the crystallization to form a mixed HCA layer (stage 5). This process is outlined in Figure 2.4 (CROVACE et al., 2016; JONES; GENTLEMAN; POLAK, 2007; RENNO et al., 2013).

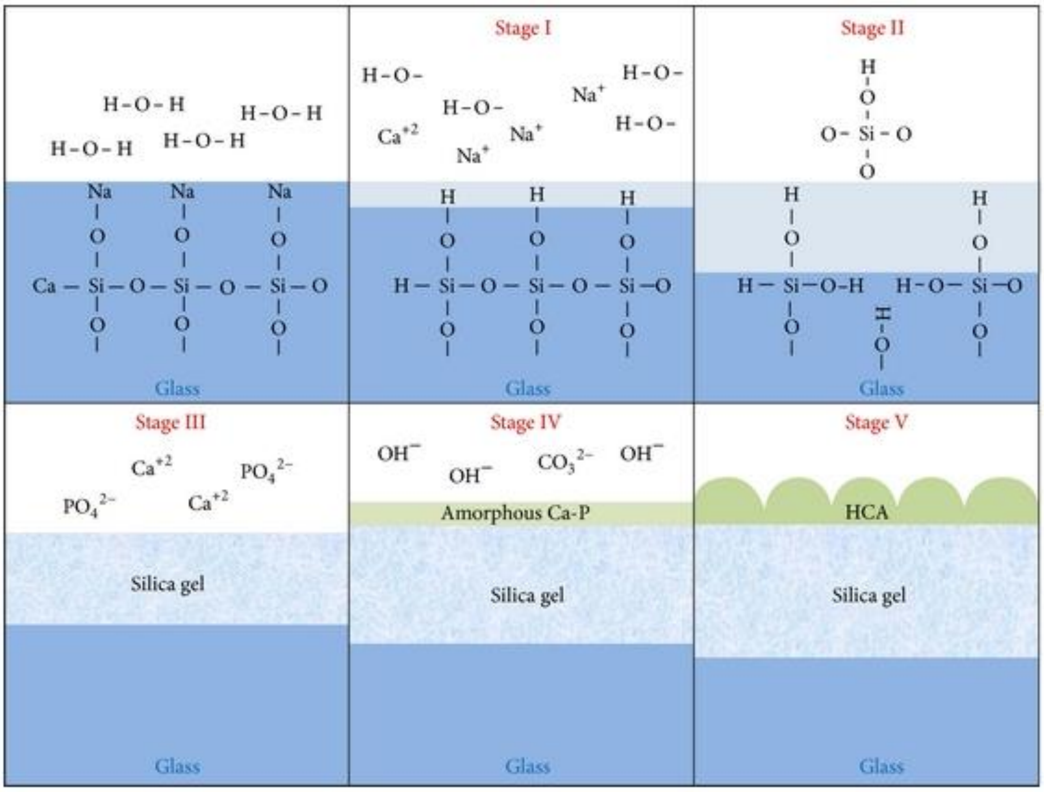

Figure 2.4 - Illustration of the mechanism of HCA formation on the surface of a bioactive glass in contact with body fluids (RENNO et al., 2013).

To form a rapid bonding to bone, the kinetics of the stages 4 and 5 should be synchronized with *in vivo* natural mineralization. It has been evidenced that certain extracellular proteins, such as fibronectin, help in the capture of macrophages, mesenchymal stem cells, and osteoprogenitor cells. The latter participates in the synthesis and deposition of the organic matrix, which is progressively mineralized (Figure 2.5) (RENNO et al., 2013).

Differentiation and proliferation of osteoblasts are involved in a rapid healing process. During osteoblast cell division, a synchronized sequence of genes is activated stimulating the production of the extracellular matrix necessary for tissue neoformation. Some studies have shown that when primary human osteoblasts are in contact with the ionic dissolution products of bioactive glasses, seven families of genes are upregulated in only 48 hours (HENCH, 2002). The reaction kinetics of the process generated by the contact between the glass and the surrounding tissue relies on the rate and class of dissolution ions released (CROVACE et al., 2016). This set of genes expresses different proteins that are deeply involved in the differentiation and proliferation of osteoblasts, such as signal transduction molecules; growth factors and cytokines related to the inflammatory response; apoptosis regulators; proteins that participate in DNA recombination, synthesis, and repair; and extracellular-matrix components (HENCH, 2002).

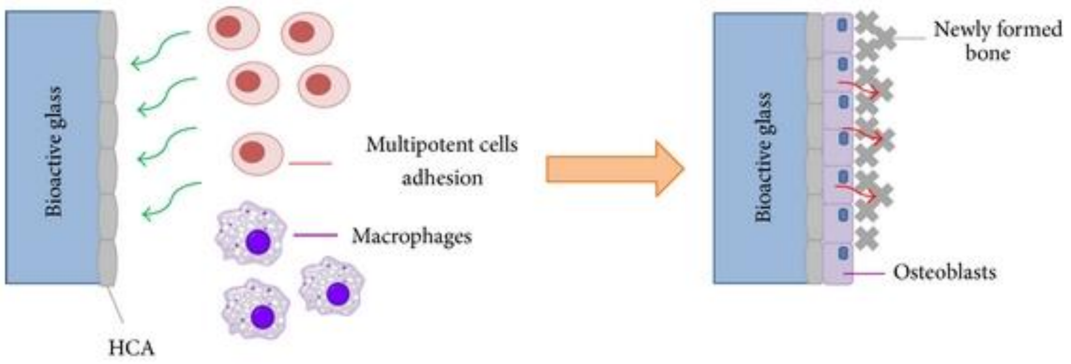

Figure 2.5 - Simplified scheme showing cell adhesion to the HCA layer formed in the glass surface (RENNO et al., 2013).

The best known bioactive glass is the 45S5, which was firstly synthesized by Larry Hench in the late 1960s and was the first material to show the ability to form an interfacial bond with host tissue in rats (JONES; GENTLEMAN; POLAK, 2007). Its particular composition provides it with special features such as the highest bioactivity index (IB = 12.5), biocompatibility, and biodegradability (CROVACE et al., 2016). Bioglass 45S5 forms a HCA layer on its surface when it interacts with body fluid, increasing osteoblast activity. This glass is classified such as class A bioactive material since it is osteogenetic and osteoconductive (ZOHORA; YOUSUF; ANWARUL, 2014). When 45S5 is resorbed, its ions are released into the media; these ionic dissolution products can upregulate gene expression, which governs osteogenesis, production of growth factors, and angiogenesis. Gorustovich *et al.* found that angiogenesis and compatibility of silicone tubes increased after they were coated with 45S5 (ROSS et al., 2003). Understanding the effect of these by-products and their specific concentrations in these processes will help to construct optimal bioactive glass compositions (GORUSTOVICH; ROETHER; BOCCACCINI, 2010; MITRA et al., 2013).

2.2.2 High porosity and pore size distribution

Porosity and pore size of the scaffolds accomplish a remarkable role in bone formation *in vitro* and *in vivo*. It has been found that osteogenesis *in vivo* is affected by pore size and relies on processes such as recruitment and penetration of cells from surrounding tissue and vascularization. Highly interconnected and open pores are essential for the scaffold performance, since this reticular structure facilitates nutrient supply, oxygen delivery to cells, and removal of metabolic waste, so migration and proliferation of osteoblasts and mesenchymal cells as well as blood vessel ingrowth are stimulated. (CUI et al., 2017; GIL et al., 2011; KARAGEORGIOU; KAPLAN, 2005).

Larger pores (above 300 µm) promote vascularization and high oxygenation, whereas smaller pores produce pore occlusion of the cells, which hampers cellular penetration, extracellular matrix production, and neovascularization of the inner areas of the scaffold (DHANDAYUTHAPANI et al., 2011; HOPPE et al., 2014; JODATI; BENGI; EVIS, 2020; MESQUITA-GUIMARÃES et al., 2019). It is known that microporosity (pores smaller than 10 µm) benefits capillary ingrowth and cell-matrix interactions (MATASSI et al., 2011). Hence, pore geometry and size must control to mimic the anatomical features of the specific bone (CUI et al., 2017; GIL et al., 2011; KARAGEORGIOU; KAPLAN, 2005).

In bone tissue engineering, adequate pore sizes for bone tissue growth are in the range from 150 µm to 900 µm. Pores larger than 900 µm diminish the surface to volume ratio, generating slow tissue neoformation, and pores smaller than 150 µm inhibit cell migration and vascularization. The ideal porosity and pore size are influenced by diverse factors, such as bone characteristics *in vivo,* specific biomaterials, cells, and cytokines use *in vitro* and *in vivo*.

Although high porosity and pore size are essential for appropriate bone ingrowth, these can deeply affect the mechanical properties of materials due to the structural weakness of the scaffold. Consequently, there is an upper limit for the pore size and porosity to prevent the mechanical properties from being severely diminished. For example, bioglasses are materials that can mimic the ECM and their ion exchange *in vivo* helps HCA ingrowth. Therefore, they are promising materials for bone regeneration, but nonetheless, highly porous structures can present low mechanical properties, being an obstacle to their broad clinical application. More robust mechanically structures can be synthesized using surface coatings, 'i.e.', the scaffold surface is covered with one synthetic or natural material, such as polymer (CHEN et al., 2007; KARAGEORGIOU; KAPLAN, 2005; MATASSI et al., 2011).

Bioglasses have been used in different studies related to bone regeneration using different compositions and porosities. Yun *et al*. used three different techniques to synthesize hierarchically giant-porous, macro-porous and nano-porous scaffolds of bioactive glass-poly (ε-caprolactone), which exhibited 3D well-interconnected pore networks (YUN; KIM; PARK, 2011). These devices exerted a good influence on both *in vitro* bone-forming bioactivities and *in vitro* cell activity (YUN; KIM; PARK, 2011). Liu *et al*. produced oriented scaffolds using 13-93 bioactive glass ($6.0Na_2O$-$7.9K_2O$-$7.7MgO$-$22.1CaO$-$1.7P_2O_5$-$54.6SiO_2$ mol.%), whose pore diameters were controllable. These 13-93 bioactive glass scaffolds showed an excellent microstructure and mechanical response, so they could be an adequate biomaterial for applying in the repair of large defects in load-bearing bones (LIU; RAHAMAN; FU, 2013). Bi *et al*. manufactured borate bioactive glass (13-93B3) scaffolds with trabecular, fibrous, and oriented microstructure and their potential for bone regeneration were evaluated *in vivo*. The best outcomes for new bone formation (33%), osteoinductive ability, and blood vessel infiltration were obtained from the scaffolds with a trabecular microstructure within 12 weeks post-implantation. These results presented a direct relationship with the increase in the total porosity and pore interconnectivity of the structures (BI et al., 2013). Yuan *et al*. prepared porous glass-ceramic using Bioglass® 45S5, and after they were implanted in thigh muscles of dogs, it was found that the scaffolds induced bone formation in the soft tissues (YUAN et al., 2001).

The properties of these and other bioglasses are summarized in Table 2.1.

Table 2.1 - Porosities and pore sizes of bioglass scaffolds for bone regeneration.

Bioglass [Reference]	**Pore size (µm)**	**Porosity (%)**	**Fabrication Technique**	**Application**
13-93 (LIU; RAHAMAN; FU, 2013)	6-120	20-60	Unidirectional freezing	Bone repair
13-93B3 (BI et al., 2013)	50-500	50-77	Melting-casting	Bone repair *in vivo*
45S5 (XYNOS et al., 2000)	10-500	-	Foaming	Primary human osteoblasts *in vitro*
45S5 (YUAN et al., 2001)	100-600	-	Sintering	Ectopic bone formation in dogs
Mesopore-bioglass (WU et al., 2010)	200-400	94	Replicate Foam	Bone marrow stromal cells *in vitro*
CO/BG scaffold (LONG et al., 2015)	40-200	81	Sol-gel	Human bone marrow stromal cells *in vitro*
MBG/poly(caprolactone) (YUN; KIM; PARK, 2011)	190 2-9 5 nm	75-84	Salt leaching Rapid prototyping Triblock copolymer templating	Human bone marrow stromal cells *in vitro*

2.2.3 Biodegradability

Biodegradable scaffolds can be absorbed by the body, and after implantation surgery is not necessary their surgical removal; as a result, they have been intensively investigated (PATEL; FISHER, 2008). Biodegradability must be accompanied with the appropriate degradation rate, so while new bone is formed, the temporary scaffold will degrade; in other words, this concomitant process guarantees that by the time the injury site is thoroughly regenerated, the scaffold will have been thoroughly degraded. This process prevents loss of the scaffold function due to its premature degradation. Degradation rate is established depending on the specific application or tissue type and is associated with the differences in load-bearing functions and rates of remodeling required (GIL et al., 2011; SABIR; XU; LI, 2009).

When the material has a high degradation rate, scaffold porosity should be less than 90% because its mechanical and structural integrity will be affected before the repair process. On the contrary, when the material has a low degradation rate and strong mechanical properties, a high porosity is adequate inasmuch as a larger pore surface area interacting with the host tissue increases degradation, which can be carried out by macrophages via oxidation or hydrolysis, or both (KARAGEORGIOU; KAPLAN, 2005).

The degradation process for apatite-derived bioceramics/bioglasses implies three different factors, such as physicochemical dissolution, this factor relies on the physical and chemical properties of the biomaterial and the pH value of media. During this process can occur the formation of new phases including amorphous calcium phosphate, dicalcium phosphate dihydrate, octacalcium phosphate, and anionic-substituted HA, which can accumulate over the surface; physical disintegration, the grain boundaries can suffer a chemical attack breaking the biomaterial into small particles; and biological factors that can affect the local pH (HENCH; BEST, 2013; WU et al., 2014). Therefore, degradation rate of these biomaterials is determined by chemical compositions, crystallinity, and physical properties such as porosity, pore size distribution, and grain size (WU et al., 2014).

In general, the consolidation of porous bioglass-based scaffolds requires thermal treatments that induce devitrification. For this reason, bioglasses are mainly used in the particulate form to fill bone defects (COMESAÑA et al., 2015; MELLI et al., 2017). It is supposed that the crystalline phases formed during these thermal treatments are not soluble and interfere with the resorption process. Despite these facts, both the crystalline volume fractions of these materials and the effect of crystallization on the resorption ability as well as the resorption mechanism of the scaffolds are rarely reported (MELLI et al., 2017). Boccaccini *et al*. analyzed the biodegradation of 45S5 Bioglass®-based glass-ceramic scaffolds in SBF by scanning electron microscope (SEM), transmission electron microscopy (TEM), X-ray diffraction (XRD), and energy-dispersive X-ray spectroscopy (EDX). They found that the material underwent dissolution mainly at glass/crystal interfaces. This dissolution was preferentially carried out in the crystal structural defects, causing fine grains due to the break-down of the crystalline particles; moreover, amorphization of the crystalline structure was observed due to the generation of point defects during ion exchange (BOCCACCINI et al., 2007). Rohanová *et al*. studied the dissolution of glass-ceramic scaffold obtained by Bioglass®, which contains 77 wt.% of crystalline phases $Na_2O.2CaO.3SiO_2$ and $CaO.SiO_2$, and 23 wt.% of residual glass phase, using SBF buffered with tris-(hydroxymethyl) aminomethane (TRIS) (ROHANOVÁ et al., 2011). They found that in SBF without buffer, the only dissolving phase was the residual glassy phase, and one amorphous calcium phosphate phase was formed on the material surface (ROHANOVÁ et al., 2011). On the other hand, SBF buffered with TRIS was able to dissolve both crystalline and residual glass phases, and a crystalline form of hydroxyapatite was formed on the scaffold surface. Moreover, the dissolving rate in the latter solution was twice as fast as in SBF without TRIS (ROHANOVÁ et al., 2011).

Melli *et al*. used water to study resorbability of Bioglass®-based glass-ceramic scaffolds produced via a powder metallurgy-inspired technology (BOCCARDI et al., 2016; MELLI et al., 2017). Both crystalline and amorphous phases were dissolved in water but with different kinetics. This surface phenomenon diminished the section of the struts, increasing the porosity without affecting the stability of the structure (MELLI et al., 2017). It is known that the solubility of the crystalline and amorphous silicate increases in neutral and basic media (ALEXANDER; HESTON; ILER, 1954; KNAUSS; WOLERY, 1988). In this study Melli *et al*. observed that at basic pH both phases were dissolved to the same extent (MELLI et al., 2017). When the glass-ceramic was in contact with water at room temperature and under stirring, the crystalline phase underwent amorphization and the movement allowed the overall surface of the structure to dissolve homogeneously (MELLI et al., 2017). Conversely, in a static medium, the outer part of the material dissolved quicker and dissolution level relied on the medium conditions. Moderate dissolution is expected in *in vivo* studies because calcium phosphate nucleation on the surface of bioglass scaffolds mediates mechanical anchorage of tissue neoformation (MELLI et al., 2017).

During craniofacial reconstructive surgeries, it is necessary to use a bioactive bone implant that can guarantee gradual resorbability and permit adjustment of the kinetics of new bone formation during repairing process (COMESAÑA et al., 2015). For this reason, Comesaña *et al*. created 3D bioceramic implants, whose inner core is comprised of calcium phosphate that moderately degrades at physiological pH; a highly reactive bioactive glass was used to enclose this layer (COMESAÑA et al., 2015). A bioactive sodium-calcium-phosphate interface connects both the inner (calcium phosphate) and the outer (bioglass) layers; and the bioactivity and degradation rates of BG particles were kept after deposition of bioglass. These gradual-resorbability implants can be used in the restoration of low-load-bearing bones (COMESAÑA et al., 2015).

Synthesis of bioglasses-based composites has become an excellent strategy to develop novel third-generation biomaterials with potential applications in diverse fields of medicine.

2.2.4 Ideal mechanical properties

Scaffolds have been used in tissue regeneration to foster formation and maturation of new tissues or organs, where a balance between temporary mechanical support and mass transport (degradation and cell growth) is vital (YUSOP et al., 2012). Hence, scaffolds should have sufficient mechanical integrity to support both the implantation procedure and the mechanical forces, which are generally experienced during the remodeling process, as well as patient’s normal activities without the scaffold collapsing. Ideally, scaffolds must possess adequate initial strength and stiffness, which should be conserved until neotissue formation is completed (COLLINS; BIRKINSHAW, 2013; YUSOP et al., 2012). Given these points, ideally, the mechanical properties of scaffolds should be similar to those of the surrounding tissue, avoiding stress shielding around the scaffold, and consequently, bone loss or implant loosening. Accordingly, this mechanical adaptation process should be fulfilled especially for open-porous scaffolds, whose bone ingrowth process is carried out inside of the scaffold (WIEDING; JONITZ; BADER, 2012). Furthermore, the mechanical properties are related to cell seeding, since certain mesenchymal stem cells (MSC) would only differentiate if the stiffness was similar to the respective tissue (CHAN; LEONG, 2008).

Metallic biomaterials have been widely used for hard tissue engineering. However, dense metallic materials have higher Young's modulus values than those of natural bone, which can cause resorption of surrounding bone tissues due to the stress shielding effect after implantation. Taking this into account, it is essential to develop porous structures whose stiffness is similar to that of natural bone (WU et al., 2014). Porous metallic scaffolds are frequently used for load-bearing application due to their excellent mechanical properties, such as superior fatigue resistance, high compressive strength, and good machinability. Nonetheless, these scaffolds have certain shortcomings, such as the fact that their surfaces are not bioactive, most are not biodegradable, and the possibility of release of toxic agents (ZOHORA; YOUSUF; ANWARUL, 2014).

Calcium phosphates, calcium sulfates, and bioactive glass have been used to synthesize devices for BTE. Calcium phosphate and bioactive glass are able to induce the formation, precipitation, and deposition of calcium phosphate from the medium, enhancing bone-matrix interface strength (MATASSI et al., 2011). Despite their high bioactivity, the use of bioglasses in medical applications has represented a great challenge due to their poor mechanical properties. When glasses undergo crystallization their strength increase, but nonetheless, this causes a reduction in bioactivity (MITRA et al., 2013).

The compressive strength of natural cancellous bone is in the range of 2 to 12 MPa, and their Young's modulus is around 22 MPa. Accordingly, many approaches have been developed to manufacture biomaterials that reach a compressive strength around these values, which is a requisite for their application in bone tissue engineering (NASERI et al., 2015).

Some glass-ceramic scaffolds, whose porosity is lower than 89%, showed a linear relationship between compressive strength and porosity (Figure 2.6); as has been noted, when the porosity of scaffold increases 10%, the compressive strength can decrease from 15 to 2 MPa (GERHARDT; BOCCACCINI, 2010).

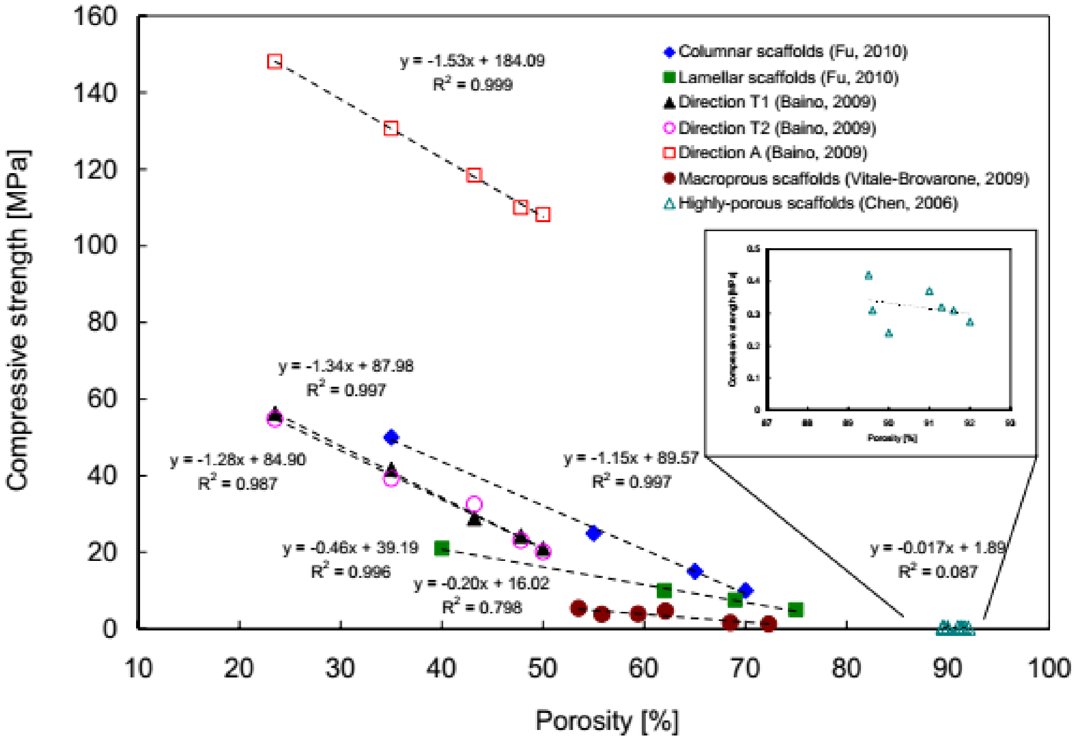

Figure 2.6 - Relationship between porosity and compressive strength of bioactive glass-ceramic scaffolds (GERHARDT; BOCCACCINI, 2010).

Yang *et al*. coated 45S5 bioglass scaffolds with different layers of alginate-chitosan. As the cycles of alginate-chitosan assembly increased, both compressive modulus and strength did too (Figure 2.7). This happens because the coatings consolidated the brittle strut walls delaying BG scaffold fracture; in addition, the struts did not fracture until the electrostatic interactions between the anionic alginate and calcium ions were broken (YANG et al., 2012). Another interesting result was that the scaffolds soaked in SBF for 48 hours showed compressive modulus similar to that of dry scaffolds; this evidences a remarkable strain tolerance together with a non-significant strength reduction (YANG et al., 2012).

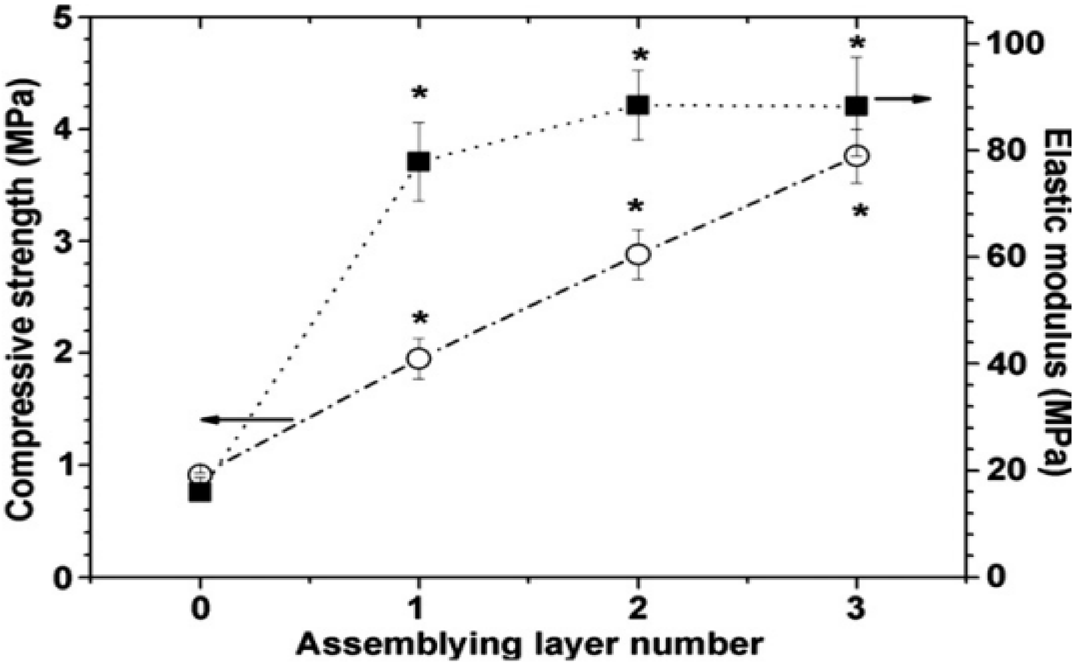

Figure 2.7 - Compressive strength and modulus of the counterionic biopolymers-reinforced 45S5 bioglass scaffolds with increasing assembly cycles (*$p<0.05$) (YANG et al., 2012).

2.3 **Biosilicate and F18 glass: potential candidates**

Although bioglasses present osteoconduction and osteoinduction, their medical applications are difficult due to their poor mechanical properties. So as to solve this inconsistency, Peitl *et al.* induced different degrees of crystallization over the Na_2O-CaO-SiO_2-P_2O_5 system at different concentrations (CROVACE et al., 2016). They demonstrated that crystallization of these materials did not inhibit HCA layer formation, even in fully crystalized ceramics, producing only a small decrease in the kinetics of HCA layer formation. Moreover, this glass was able to induce the formation of HCA layer faster than commercial products, such as A/W glass-ceramics, synthetic hydroxyapatite, Ceravital, and Bioverit. This high rate of HCA formation on the glass-ceramics can be explained by two mechanisms that act concomitantly, a soluble non-phosphate crystal phase (1N2C3S) and phosphorus ions in solid solution that can be easily liberated to the medium, fostering an elevated reaction rate during this process (PEITL; DUTRA ZANOTTO; HENCH, 2001; PEITL; LATORRE; HENCH, 1996).

The specific composition $23.75Na_2O$-$23.75CaO$-$48.5SiO_2$-$4P_2O_5$ (wt.%) is known as Biosilicate®. When this system is subjected to controlled double stage heat treatments, this material can exhibit one phase of sodium-calcium silicate ($Na_2CaSi_2O_6$) or two phases one of $Na_2CaSi_2O_6$ and the other of sodium-calcium phosphate ($NaCaPO_4$). This biomaterial has interesting properties such as osteoconductivity, osteoinductivity, and bactericide; furthermore, it is non-cytotoxic and non-genotoxic. It has shown to be a versatile, multipurpose biomaterial and its shape is easily tunable. This material has been successfully tested in several *in vitro*, *in vivo*, and clinical studies, being a promising candidate for different tissue engineering applications (CROVACE et al., 2016). Renno *et al.* researched the effect of filling the tibial bone defect in rats with Biosilicate and 45S5 Bioglass®. They used two particle size distributions, one from 180 µm to 212 µm and the other from 300 µm to 355 µm, and they observed that for both distributions, the specimens with Biosilicate presented a higher amount of newly formed bone in the callus than those ones of the control group, as well as higher mechanical stability (GRANITO et al., 2009, 2011; RENNO et al., 2013).

Bossini *et al.* used low-level laser therapy (LLLT) and Biosilicate to evaluate the healing process of bone fracture in osteoporotic rats. The particle size distribution used was in the range from 180 µm to 212 µm. This study showed that for the rats treated with laser therapy (120 J/cm^2) and Biosilicate, a higher amount of newly formed bone was formed than for those of the control group. This, together with COX2 and CBFA1 immunoexpression, angiogenesis, and collagen deposition in the defect, stimulated bone repair (BOSSINI et al., 2011).

There are different infections that are related to surgical implants, which generate clinical, economic, and psychological issues, such as intensive surgical treatments and antibiotic therapies, loss of the implant, emotional problems, financial loss, and even death (DAROUICHE, 2004). About 14% of patients with dental implants can suffer peri-implantitis, which is associated with some pathogenic microorganisms, such as *Fusobacterium ssp*, *A. actinomycetemcomitans*, and *P. gingivalis*. To fight against these species, some strategies are being used such as anti-bioadhesion coatings; surfaces coated with antimicrobial agents such as vancomycin, Ag, and Zn; or antimicrobial releasing coatings such as calcium phosphate, polylactic acid, and chitosan (NOROWSKI; BUMGARDNER, 2009). Oral microorganisms, such as *S. aureus, P. aeruginosa,* and *E. coli* are associated with the microbiota of dental biofilm in periodontitis, which are very difficult to eradicate from biomaterial implant surface because they form an exopolysaccharide layer that is very resistant to immune response in patients and antibiotic therapy (HURT et al., 2015; SOUTO et al., 2006). Hence, one strategy to establish steady anchorages of the scaffold in the surrounding bone is to develop new materials that concomitantly promote prevention of bacterial infections and osteogenesis (NOROWSKI; BUMGARDNER, 2009). Martins *et al*. researched the antimicrobial properties of Biosilicate using techniques such as agar diffusion, direct contact, and minimal inhibitory concentration (MIC). Among them, the outcomes obtained with the direct contact technique are remarkable, where the biomaterial presented antimicrobial activity against 19 of 20 species and the only organism that exhibited resistance was *Staphylococcus aureus*. These results are relevant inasmuch as no antimicrobial element was used. Although the exact antimicrobial mechanism of this biomaterial is not completely elucidated, it is known that Biosilicate in powder acquires a highly reactive surface and, in contact with an aqueous suspension, releases cations that increase the pH of the medium, inhibiting bacteria growth (MARTINS et al., 2011).

F18 glass is a new bioactive glass developed in Vitreous Materials Laboratory of the Federal University of São Carlos (LaMaV-UFSCar). This SiO_2-Na_2O-K_2O-CaO-MgO-P_2O_5 system overcomes certain difficulties that are currently presented for other bioactive glasses such as uncontrolled crystallization during extended or repeated heat treatments, which deeply reduces their bioactivity and diminishes their mechanical properties (SOUZA et al., 2017). Therefore, this highly stable and bioactive glass permits manufacturing several kinds of medical devices such as flexible continuous fibers, porous sintered bodies, and 3D complex shapes. Consequently, this biomaterial is potentially an excellent alternative for soft and hard tissue regeneration in many applications (SOUZA et al., 2017). *In vitro* tests have shown that F18 glass fibers are highly bioactive and soluble and require only 4 hours for HCA layer formation (SOUZA, 2015). *In vitro* biocompatibility of F18 glass was also evidenced by the notable proliferation of fibroblasts and osteoblasts after cells were cultured in F18 solutions with different concentrations and exposure times; in addition, these fibers did not produce DNA strand breaks in both cell lines (GABBAI-ARMELIN et al., 2017; SOUZA et al., 2017). In the same way, F18 scaffolds were implanted subcutaneously in rats to analyze *in vivo* biocompatibility; thus, two months after implantation, whole scaffold degradation was observed with formation of an organized granulation tissue (GABBAI-ARMELIN et al., 2017; SOUZA et al., 2017). In another study, it was reported that after 60 days of implantation of F18 scaffolds in rat tibial defects, the injured part was replaced by mature formed bone without an inflammatory response. Besides, 15 days after the surgical procedure, the mechanical properties of the tibial callus had increased. These results are related to bone inductive property of F18 and the arrangement of the F18 scaffold's microstructure that stimulates the formation of a quality bone (SOUZA et al., 2017).

2.4 Conventional techniques for Bioceramics scaffold fabrication

Different techniques have been developed to fabricate porous scaffolds for BTE, which mimic the extracellular matrix of natural bone, using synthetic and natural materials. These techniques including gel casting of foams, incorporation of volatile organic particles in the ceramic powders, foam replication, gel-polymer process, sol-gel, solvent-casting/salt-leaching, etc. (BAINO; NOVAJRA; VITALE-BROVARONE, 2015; MAO, 2017; WANG; RUAN; CHEN, 2009).

2.4.1 Foaming methods

Ceramic foams with highly porous structures are produced by dispersion of gas, which forms bubbles inside the ceramic suspension. The range of pores reached by this technique is from 20 μm to 2 mm. There are different strategies to carry out foaming such as the incorporation of gas inside the slurry. In some cases, it is necessary to stabilize the bubbles inside the slurry using surfactants or hydrophobic particles that can diminish the surface energy between liquid and gas (MAO, 2017). There are diverse ways to introduce external gas such as mixing a large quantity of gas with the liquid, which is dispersed by mechanical stirring, followed by solidification. Another alternative, it is used an aqueous solution of H_2O_2, which is mixed with ceramic powder (BAINO; NOVAJRA; VITALE-BROVARONE, 2015). After the mixture is cast, the temperature is increased to 60°C, which is the decomposition temperature of hydrogen peroxide. During the decomposition is formed O_2 that forms bubbles necessary for the foaming. Then, the samples are sintered, giving rise to crystalline ceramics, bioactive glass, calcium phosphate scaffolds, etc. (BAINO; NOVAJRA; VITALE-BROVARONE, 2015; NAVARRO et al., 2004).

The production of bubbles inside the slurry can be done using a hydrophilic organic monomer, which is mixed with an aqueous ceramic suspension and a surfactant, this technique is known as gel-cast foaming and produces porosities from 40% to 90%, the amount of closed or open pores relies on pore fraction. Subsequently, an initiator and a catalyst are added to initiate the polymerization, giving rise to the green body, which will be later dried and sintered (Figure 2.8) (BAINO; NOVAJRA; VITALE-BROVARONE, 2015; MAO, 2017; ORTEGA; SEPULVEDA; PANDOLFELLI, 2002).

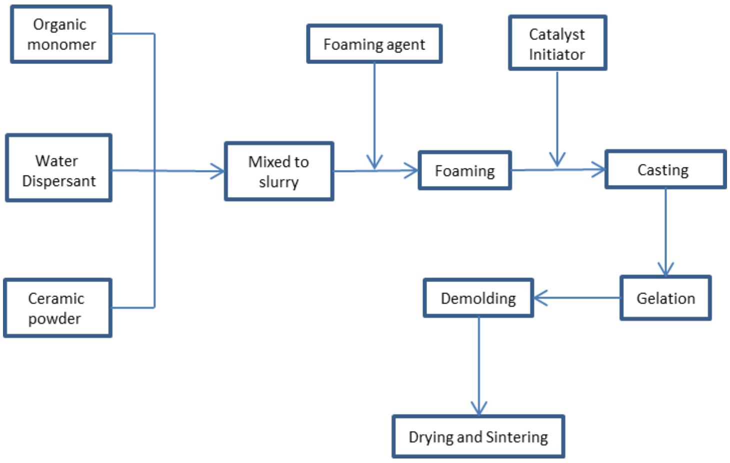

Figure 2.8 - Flow chart for the production of ceramic foams by gel-casting of foams (MAO, 2017).

2.4.2 Foam replica technique

This is the easiest and most widely used method to obtain scaffolds for BTE. This technique has been used to synthesize bioactive glass scaffolds since 2006 (CHEN; THOMPSON; BOCCACCINI, 2006). Before this date, they were produced using other techniques, such as dry-powder processing with porogen additions, sol-gel method, and gel-casting method (CHEN; THOMPSON; BOCCACCINI, 2006). This technique has exhibited a great capability to mimic the trabecular bone structure, enhancing cell adhesion, proliferation, and differentiation. Using this method, scaffolds with porosity higher than 90% and highly interconnected porous structures have been obtained, which stimulate cell ingrowth and angiogenesis during repairing process (CHEN et al., 2007; CHEN; THOMPSON; BOCCACCINI, 2006).

To fabricate porous scaffolds by this technique, it is necessary to prepare a suspension or slurry, adding glass-ceramic, ceramic, or bioglass powder to PVA aqueous solution under stirring (Figure 2.9). Then, it is used a sacrificial template such as a polyurethane foam to replicate the highly porous network of the scaffold. The sacrificial template is dipped in the slurry to permit the ceramic or glass particles to attach to the surface of the polymer; this step can be repeated. To avoid an inhomogeneous coating on the foam struts, the excess of slurry is taken out by squeezing the template. Then, the sample is dried at room temperature, followed by sintering that allows reaching the adequate density, sometimes the polymer can be slowly burned out before sintering. In this way, this technique mimics the macrostructure of the sacrificial template, forming an appropriate microstructure (CHEN et al., 2007; CHEN; THOMPSON; BOCCACCINI, 2006; DESIMONE et al., 2013).

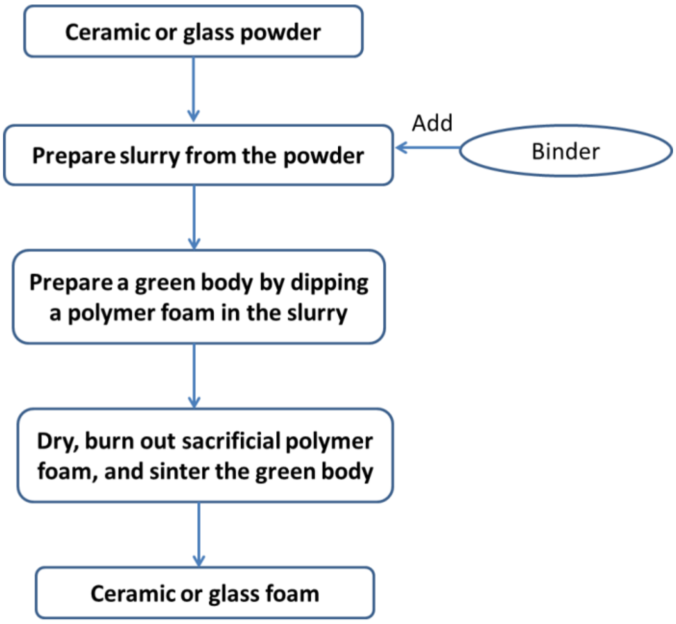

Figure 2.9 - Flowchart of the polymer-sponge method for fabrication of glass or ceramic foams (CHEN; THOMPSON; BOCCACCINI, 2006).

Foam replica method has been used to synthesize bioactive glass-ceramic materials using 45S5 Bioglass and Biosilicate; with this technique can be obtained the ideal conditions for BTE, such as a porosity of 95% and pore sizes between 200 µm to 500 µm (CHEN et al., 2007; DESIMONE et al., 2013).

2.4.3 Sol-gel foaming

Another option for foaming is sol-gel foaming, which is based on the sol-gel method and mechanical frothing (BAINO; NOVAJRA; VITALE-BROVARONE, 2015). Sol-gel formed a colloidal suspension that is currently produced by condensation of metal alkoxide precursors (tetraethylorthosilicate and triethylphosphate) using salts ($CaNO_3$) and a hydrolysis catalyst (DANKS; HALL; SCHNEPP, 2016). Then, the suspension containing a gelling agent, a surfactant, and distilled water is vigorously stirred. After casting, the gelation is complete and solvent is taken out by gently drying. Finally, the porous structure is obtained after sintering (BAINO; NOVAJRA; VITALE-BROVARONE, 2015). With this technique, 3D scaffolds of glass or glass-ceramic with interconnected macropores and sizes between 10 µm to 500 µm can be produced. Additionally, these materials present a nanoporous texture in the range from 2 nm to 50 nm, diminishing mechanical properties of scaffolds (BAINO; VITALE-BROVARONE, 2011).

2.4.4 Solvent-casting/salt-leaching technique

This method permits obtaining foam-like structures with an easy preparation process. The solvent-casting/salt-leaching technique implies the following steps. First, the polymer, e.g. PCL or PLA, is dissolved using organic solvents and stirred to obtain a homogeneous slurry system; sometimes, it may be necessary to use heat. Second, sieved salt is added to the slurry under stirring. Third, the ceramic powder is added to polymer/solvent/salt using mechanical stirring, and this homogeneous gel-like mixture is casting in a Teflon mold (DARUS et al., 2018). Fourth, the drying process is done to evaporate the organic solvent by controlled evaporation or ultrasonic vibration, which also helps in the complete solidification. Then, the salt is washed out by immersing the samples in deionized or distilled water for some days; this can also help to remove the trace of solvents. Finally, the salt-removed samples can be dried (MEHRABANIAN; NASR-ESFAHANI, 2011; PARK et al., 2012; TAHERKHANI; MOZTARZADEH, 2016).

Despite being such a practical and economical technique, which permits designing foam-like structures with a high porosity, many times residual NaCl or organic solvents keep in the final scaffold; in addition, it is difficult to obtain a well-defined geometry and when pressure is used, it is laborious to produce some complex structures (CHO et al., 2014; CUI et al., 2017). Moreover, pore interconnectivity depends on whether the particles are in contact. It means that pore connectivity is low. As a result, it has been introduced some process modifications to improve this conventional method, such as sintered NaCl template method (CHO et al., 2014; CUI et al., 2017).

2.5 Applications of ceramics in tissue engineering

2.5.1 Ceramic-based injectable scaffolds

For many years, ceramics such as hydroxyapatite, tricalcium phosphate, biphasic calcium phosphate, and bioactive glasses mixed with diverse biopolymers have been used to replace autogenous bone, which are used for repair, substitution, or augmentation. These composites based on calcium phosphate are resorbable and are able to produce bone trabeculae, being their resorption rate synchronized with the formation of new bone. In bone tissue engineering, a pore size smaller than 5 μm facilitates bioresorption of the scaffold and pore sizes between 400 μm and 600 μm foster cellular migration and osteogenic differentiation, but nevertheless, this size range is large for an injectable scaffold. Accordingly, particles with diameters from 10 to 100 μm are used to guarantee injectability and better growth of fibrovascular tissue. In addition, mixtures of the low and high soluble ceramics such as hydroxyapatite and β-tricalcium phosphate are used to reach appropriate solubility of biomaterials, which permits the correct remodeling of the injured site (MIGLIARESI; MOTTA; DIBENEDETTO, 2018).

Different injectable and resorbable materials, such as $^{\beta}$Beta-bsm® and Norian SRS, are commercialized. $^{\beta}$Beta-bsm® (Figure 2.10) is a biocompatible bone graft substitute scaffold, which is distributed by Zimmer Biomet and can be applied using a minimally invasive procedure. Composition of this nanocrystalline calcium phosphate is similar to the inorganic part of human bone and reaches an average compressive strength of 30 MPa (BIOMET, 2019).

Norian SRS bone void filler (Figure 2.11) is an injectable material, which can be used in orthopaedic and trauma applications such as bony voids or gaps of the skeletal system, for example in extremities, pelvis, crania and face (BIOMET, 2019; MIGLIARESI; MOTTA; DIBENEDETTO, 2018).

Figure 2.10 - Image of $^{\beta}$Beta-bsm$^{\circledR}$, injectable osteoconductive material that stimulates new bone growth (BIOMET, 2019).

Figure 2.11 - Norian SRS, calcium phosphate bone void filler (NORIAN, 2019).

This biomaterial is resorbed during normal cellular remodeling and replaced with new bone tissue while strength is maintained. This calcium phosphate cement is mixed with a carbonate and sodium phosphate solution to obtain the injectable filler, which reaches a compressive strength of 55 MPa in 12 hours (MIGLIARESI; MOTTA; DIBENEDETTO, 2018).

2.6 Strategy to increase the compression strength

To improve the compression strength of the Biosilicate scaffold will be used F18 bioactive glass coatings. F18 was chosen because it exhibits remarkable bioactivity, possesses a wide workability spectrum, and improves bio-interaction (SOUZA et al., 2017). In addition, it is the first time that F18 glass is used to increase the compressive strength of Biosilicate scaffolds. Different F18 devices have evidenced enough mechanical strength for handling and have increased the mechanical properties in rat tibial callus (SOUZA et al., 2017). The aim to use this biomaterial is that F18 bioactive glass flows without crystallizing at temperatures above 600 ºC, bridging micro-gaps in the Bioglass®-struts without clogging the pores. When F18 infiltrated the cracks and voids of the struts, the compressive strength and stiffness of the scaffold were enhanced, improving the mechanical stability of the overall structures.

Tiainen *et al*. employed an approach to significantly increase compressive strength of the TiO_2 scaffolds by removing internal porosity using a vacuum infiltration process (TIAINEN; WIEDMER; HAUGEN, 2013). In this study, Tiainen *et al.* synthesized highly porous TiO_2 bone scaffolds using polymer sponge replication. The sintered TiO_2 scaffold was recoated with a TiO_2 slurry, the slurry excess was removed by centrifugation; subsequently, the scaffold was dried and sintered. Then, to eliminate the internal porosity of the struts, a vacuum infiltrated TiO_2 coating was carried out using a pressure of 0.2 mbar for 5 minutes and a low-viscosity TiO_2 slurry. After this process, a uniform TiO_2 layer was deposited on the struts, and lateral cracks on the strut surfaces considerably reduced; additionally, the compressive strength of the scaffold increased from 1.8 MPa to 3.4 MPa, and the scaffold conserved highly interconnected and open pores as well as an adequate pore size (TIAINEN; WIEDMER; HAUGEN, 2013).

It has been suggested that for load-bearing applications, scaffolds should exhibit compression strength similar to that of the cortical bone, i.e., in the range 100-150 MPa (FU et al., 2013). However, a compressive strength similar to that of trabecular bone (2-12 MPa) would be enough for applications in dentistry where there is no significant mechanical loading, such as sinus lifting and vertical augmentation surgeries (Figure 2.12).

There are several commercially available products for such applications. An example is ReproBone^{TM} sold by the British company Ceramysis. ReproBone^{TM} is a composite scaffold (60%HA-40%βTCP) available in many shapes, including blocks (1x1x2 cm). These porous blocks (or scaffolds) exhibit a total porosity of approximately 80%, an average pore size in the range from 200 μm to 800 μm and a compressive strength of 1.5 MPa (CERAMISYS, 2019).

Another example is the chronOS® sold by the company DePuy Synthes. This product is based on βTCP and is also available in preforms, with a total porosity of 70%, macropores in the range from 100 μm to 500 μm and a compressive strength around 5 MPa (DEPUYSYNTHES, 2019).

Endobon® sold by the company Zimmer Biomet, is a bovine HA ceramic. This product is also available in the form of small blocks and has a total porosity in the range from 45% to 85%, pore sizes in the range from 100 μm to 1.500 μm and compressive strengths from 1 MPa up to 20 MPa, depending on the porosity level (KURIEN; PEARSON; SCAMMELL, 2013; ZIMMERBIOMET, 2019).

There are other available products based on calcium phosphate ceramics with increased compressive strength (in Brazil and abroad), but with inferior porosity, in the range from 50% to 60%. This porosity level is considered insufficient for bone ingrowth by most researchers in the scientific community (DESIMONE et al., 2013).

Therefore, in this work, the goal was to obtain scaffolds with a total porosity > 80%, pore sizes > 300 μm, and an adequate compressive strength for some specific applications in dentistry, such as those mentioned above.

(a)

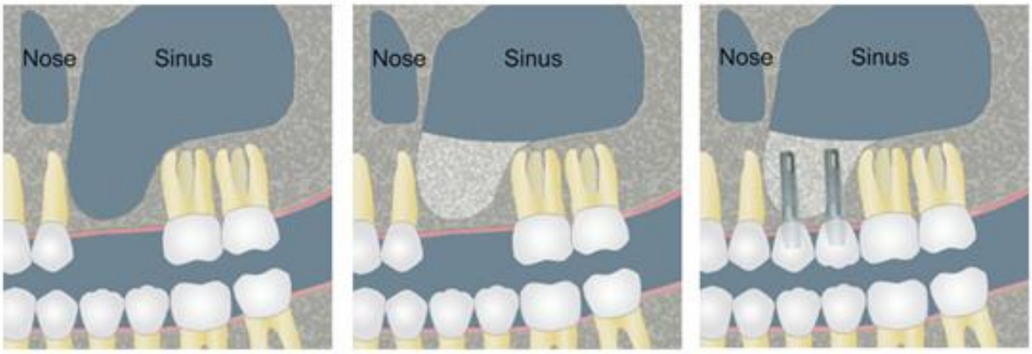

(b)

Figure 2.12 - Schematic representation of the use of scaffolds (a) in a sinus lift surgery and (b) in a vertical augmentation surgery.

2.7 Mesenchymal stem cells

Mesenchymal stem cells (MSCs) are clonogenic cells that can be highly expanded and form fibroblast-like colonies with multipotential to differentiate in different lineage such as osteoblasts, chondrocytes, adipocytes, and myoblasts (CALABRESE et al., 2016; MIRON; ZHANG, 2012). Usually, human MSCs are isolated using a small aspirate of bone marrow; nevertheless, MSCs can be found in other tissues such as adipose tissue, umbilical cord blood, amniotic fluid, skin, hair follicle, dental pulp, etc. (CALABRESE et al., 2016; KULTERER et al., 2007). Adipose-derived stem cells (ASCs) are an interesting source of cells for BTE since they are easily harvested in high quantity, and they have the potential for osteogenic differentiation (ZUK et al., 2001). Another advantage of MSCs is that they can be extracted from own patients, avoiding problems such as immune rejection and possible disease transmission (KULTERER et al., 2007). These cells have been using in different clinical treatments such as heart infarct ischemia, stroke ischemia, meniscus regeneration, tendinitis, spinal cord interruption, and healing of damaged cartilage and bone (MIRON; ZHANG, 2012). Although these cells present highly therapeutic properties, the complex mechanisms that control MSCs expansion and differentiation in their different lineages have not been well elucidated yet, being an active area of medical research (KULTERER et al., 2007).

2.8 Induced pluripotent stem cells

Embryonic stem (ES) cells are so much important in research since these cells are pluripotent and possess high differentiation and proliferation potential, being a valuable instrument to elucidate the mechanisms of human development and differentiation processes. Moreover, these types of cells represent an option to create new treatments for diverse illnesses (LO; PARHAM, 2009). Nevertheless, fertilized embryos are used for the derivation of these cells, which generates ethical and political issues. An interesting option to replace these cells is induced pluripotent stem (iPS) cells, which were created by reprogramming of mouse fibroblasts in 2006 (LO; PARHAM, 2009; ROBINSON et al., 2015; WILLERTH, 2011). These cells have the ability to differentiate in different lineages *in vivo* and *in vitro*, and iPS cells differentiate into mature osteoblasts conserve their phenotype in 3D scaffolds (BILOUSOVA; JUN; KING, 2011). Moreover, they are able to induce the expression of diverse factors related to pluripotent cells and their gene expression and activity are similar to those of ES cells; nonetheless, their differentiation potential varies relying on the lineage and the experimental conditions used. Another interesting fact, it is the possibility to use patient’s own iPS cells for regenerative treatment (BILOUSOVA; JUN; KING, 2011).

2.9 **Osteogenic induction and mineralization**

Osteogenesis is a complex process, which requires that mesenchymal precursors proliferate and condense in a highly interactive group, guiding towards the deposition of an organic matrix that subsequently mineralizes and stimulates the construction of final bone (LATTANZI; BERNARDINI, 2011). Among osteoblast lineage cells can be found osteoprogenitors, osteoblasts and osteocytes (Figure 2.13), these cells are obtained through differentiation process of MSCs, which involves different complex stages that are under investigation (KARGOZAR et al., 2019). In the different types of osteogenesis, osteoprogenitor cells partially differentiate into preosteoblasts before osteoblast formation (Figure 2.13) (MIRON; ZHANG, 2012; RUTKOVSKIY; STENSLØKKEN; VAAGE, 2016). Preosteoblasts are recognized by inducing ALP expression and their commitment into osteoblasts is induced by different genes such as RUNX2, DLX5, and SP7 (KARGOZAR et al., 2019). When RUNX2 is activated, the cells form preosteoblasts, and subsequently go through different stages characterized by expression of specific osteogenic markers. Preosteoblasts begin proliferating, together with the expression of fibronectin, collagen, TGFβ receptor 1, and osteopontin. Then, the cell cycle stops, and differentiation begins (LONG, 2012).

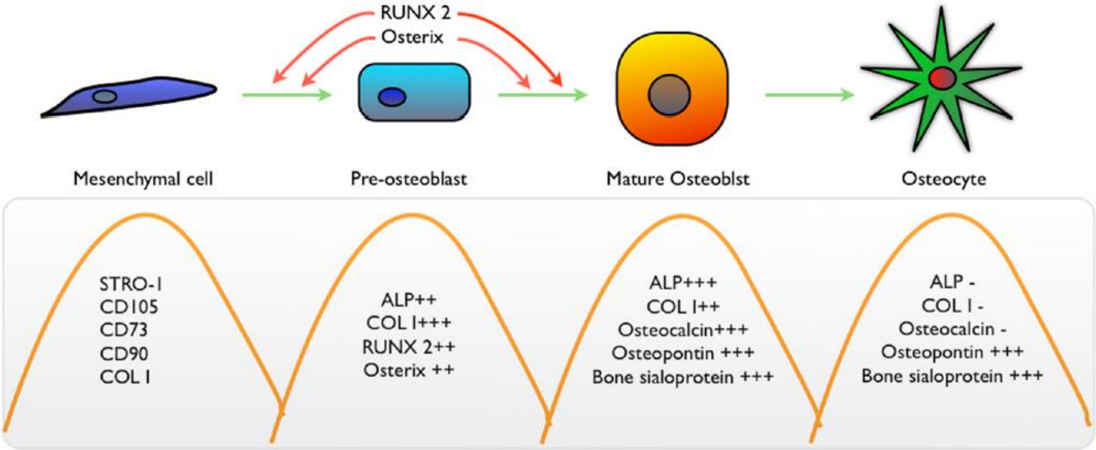

Figure 2.13 - Schematic representation of cells involve in osteogenesis: MSCs, pre-osteoblasts, osteoblasts, osteocytes and theirs markers (MIRON; ZHANG, 2012).

The formation of bone tissue begins when osteoblasts secrete the bone matrix, which is composed of 90% of type I collagen (KNOTT; BAILEY, 1998). It has been found that after whole differentiation into osteoblasts, bone sialoprotein and osteocalcin are highly expressed. Bone sialoprotein represents about 5 to 10% of non-collagenous proteins in the ECM, which binds to type I collagen and induces hydroxyapatite crystal formation (MIRON; ZHANG, 2012). In the same way, osteocalcin is the major osteoblast-specific non-collagenous protein, representing around 10% (LINDEN; CRAIG, 2007). This protein synthesizes by osteoblasts is part of organic matrix and possesses γ-carboxyglutamic acid residues and its acid groups favor strong bind to calcium, mediating the bond between calcium and hydroxyapatite (LINDEN; CRAIG, 2007; MIRON; ZHANG, 2012). Fully mature osteoblasts are responsible for the secretion of collagen and noncollagen constituents of bone matrix, which is isolated from the extracellular fluid for an organized tight epithelial layer of osteoblasts, permitting the control of the matrix environment during mineralization (BLAIR et al., 2017; KARGOZAR et al., 2019). While matrix is growing, some osteoblasts become part of the ECM and subsequently become osteocytes (Figure 2.13), these stellate cells are placed in narrow interconnected passages in the ECM (RUTKOVSKIY; STENSLØKKEN; VAAGE, 2016). Osteoblasts lost in the epithelial layer are replaced for new recruited cells to preserve the layer during active bone formation (BLAIR et al., 2017). Osteocytes have the ability to communicate both among them and with the osteoblasts of the surface layer, this cellular communication is carried out through canaliculi that permeate the matrix (BLAIR et al., 2017).

Before mineralization, the extracellular matrix needs to gain enough structural stability, which is mostly provided by the polymerization that generates the array fibril, and the degree of cross-linkings that defines the stability of the collagen triple helix, preserving the mechanical properties and regulating biological functions (CHRISTIANSEN; HUANG; SILVER, 2000; SHEN et al., 2018). Other important factors in the matrix maturation are both the formation of protein-glycoaminoglycan complexes and the bound between calcium and collagen fibrils (DONALD; HEANEY, 2019; KAARTINEN et al., 2002). Moreover, there is a little quantity of some proteins such as osteopontin and osteocalcin inside the ECM, which have important functions in the coordination of organic matrix and bone mineralization (BLAIR et al., 2017; MIRON; ZHANG, 2012). During bone maturation, collagen acquires specific orientations in the place where the dense hydroxyapatite-based mineral will be deposited; this process is mediated by different mechanisms, such as active and passive transport as well as pH control (BLAIR et al., 2017).

After matrix maturation, which can last of 10-14 days, the mineralization begins. Blair *et al*. found that crystal nucleation is guided by a specific proton export network that promotes two-phase removal of acid through the osteoblasts epithelium and subsequent mineral condensation (BLAIR et al., 2017; LARROUTURE et al., 2015). Additionally, mineralization is characterized by the inhibition or degradation of the inhibitors that prevent mineralization; these molecules are important because they permit the regulation of this process. Briefly, proteoglycans regulate and initiate the formation of crystal nuclei, followed by the precipitation of calcium and phosphate giving origin to the hydroxyapatite $[Ca_{10}(PO_4)_6(OH)_2]$, which grows between and within collagen fibrils. This process takes around ten days, and the specific location and orientation of each crystal is regulated by the structure of collagen and non-collagenous proteins (DONALD; HEANEY, 2019; KOMAROVA et al., 2015).

2.10 **Types of ossifications**

Bone and cartilage are the tissues that form the skeleton, and osteoblasts and chondrocytes are the cells that synthesize them, respectively (HOUSCHYAR et al., 2019). There are two different types of bone formation, and in both of them, the mesenchymal tissue transforms into bone tissue. Bones are principally formed by endochondral ossification (Figure 2.14), where condensed groups of mesenchymal cells grow and differentiate in chondrocytes. Chondrocyte proliferation and secretion of the cartilage-specific extracellular matrix give rise to the cartilage template that defines the final shape of bone (LATTANZI; BERNARDINI, 2011). When chondrocytes stop dividing, their volume is augmented, generating hypertrophic chondrocytes. This cellular modification permits collagen X and fibronectin to be added to the extracellular matrix, creating appropriate conditions for mineralization. Then, the cartilage model begins being infiltrated by blood vessels and osteoclasts penetrate in the cartilage template and digest the extracellular matrix (LATTANZI; BERNARDINI, 2011; XUE et al., 2009). Some of the hypertrophic chondrocytes undergo apoptosis and others continue proliferating, guaranteeing bone lengthening in the postnatal process. Over degraded cartilage, osteoblasts synthesize extracellular matrix and, finally, all cartilage is replaced by bone tissue (Figure 2.14).

Unlike the endochondral ossification through which long bones develop, flat bones are synthesized through a direct process known as intramembranous ossification. In this process, mesenchymal cells differentiate into osteoblasts without intermediate steps as occurs in osteochondral ossification in which a template is used, which facilitates angiogenesis and models bone tissue. In intramembranous ossification, osteoblastic differentiation of MSCs into preosteoblasts is followed by differentiation into osteoblasts, which produce the matrix extracellular that mineralizes, giving origin to bones tissue (XUE et al., 2009).

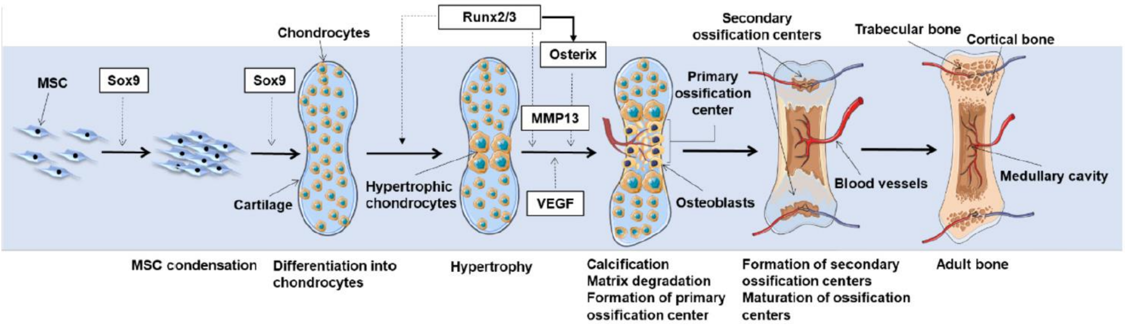

Figure 2.14 - Draw of endochondral ossification. Here is represented the condensation of MSCs that guides to the differentiation into chondrocytes forming an intermediate cartilage. Then, the chondrocytes become hypertrophic, which induce vascular invasion in the cartilage, and cells that were brought by blood vessels into the cartilage template begin to differentiate and form bone tissue at a primary ossification center. Subsequently, bond formation extends following the length of shaft forming secondary ossification center. The final bone is composed of trabecular and cortical bones, and the medullary cavity. In this process, different factors mediate differentiation, being SOX9 the most important (LOPES et al., 2018).

2.11 Mechanisms of bone repair and regeneration

Bone is a special tissue that has the ability to self-remodel during entire life. When this tissue suffers a lesion, it heals itself developing new bone tissue, which will have the same structural and biomechanical integrity as uninjured tissue (HOUSCHYAR et al., 2019). This cicatrization process is similar to embryonic bone formation during fetal development, being a complex and well-organized regenerative process that involves the regulation and expression of many biomolecules, which induce and control the osteogenesis process (FERGUSON et al., 1999). This healing process can be performed by direct or indirect repair. Direct repair occurs when the bony fronts of the injured adjacent tissue are near. In many cases, this is achieved through a surgical treatment that permits steady stabilization of the fracture (HOUSCHYAR et al., 2019; PESCE et al., 2009). The process used during direct repair is similar to intramembranous ossification, which is stimulated by different cells such as osteoprogenitor cells, osteoclasts, and MSCs that arrive to the fracture tissue. Another strategy used to repair this steady injury is using an indirect mechanism, which is carried out through endochondral ossification. After the fracture, an inflammatory process begins resulting in the formation of a soft callus, which in turn will give rise to the cartilage that is used as a template in this type of ossification (HOUSCHYAR et al., 2019; MARSELL; EINHORN, 2011). After the fracture is fixed or immobilized, these types of repair needs some months for complete healing. Nevertheless, up to 10% of bone fracture repair cannot heal adequate, generating formation of a fibrous tissue or non-union (HOUSCHYAR et al., 2019). In some of these cases, traditional bone tissue engineering strategies use direct *in vitro* bone-like matrix formation in scaffolds to help to bring together fracture sides, which are difficult to keep together (THOMPSON et al., 2015). These strategies are based on bone formation by intramembranous ossification. After scaffold implantation, inflammatory wound healing response stimulates the formation of a complex network of blood vessels. Nevertheless, osteoconductive or osteoinductive bone scaffolds commonly do not promote angiogenesis resulting in poor vascularization (BOSE; ROY; BANDYOPADHYAY, 2012). Diffusion limitation and insufficient vascular network provoke oxygen and nutrient deficiency and hinder waste removal from the scaffold, generating limited area for bone regeneration and avascular necrosis (THOMPSON et al., 2015). An alternative for resolving this problem is the implantation of *in vitro* tissue-engineered cartilage, which is used as an intermediate template where hypertrophic chondrocytes can produce angiogenic and osteogenic factors, permitting the formation of blood vessel network and the deposition of mineralized extracellular matrix (THOMPSON et al., 2015). Jukes *et al.* synthesized a cartilage matrix passaging embryonic stem cells over scaffolds, which were implanted in mice, inducing endochondral ossification in 21 days (JUKES et al., 2008). Besides, Tortelli *et al.* found that the type of ossification *in vivo* is influenced by the type of cells seeded *in vitro* over the porous ceramic scaffolds; when MSCs and osteoblasts were passaged over the implants, endochondral and intramembranous ossification were induced, respectively (TORTELLI et al., 2010).

2.12 **BMP pathway**

To achieve osteogenic process, many factors and signaling pathways need to be coordinated to induce regulated proliferation, migration, and differentiation; all of these molecules and cross-talking pathways create a highly interconnected and complex network that is not well understood (HOUSCHYAR et al., 2019; SCOTT, 2000). The best-known signaling pathways that control osteogenesis are the wingless-int (WNT), bone morphogenetic protein (BMP), hedgehog (HH) and fibroblast growth factor (FGF) families (LATTANZI; BERNARDINI, 2011). Among these, the most important osteogenic signaling pathway is the BMP; together with FBF signaling and factors such as RUNX2 and SOX9, which are considering the “master factors” during intramembranous and endochondral ossification, respectively (KARSENTY; KRONENBERG; SETTEMBRE, 2009; VLACIC-ZISCHKE et al., 2011).

Transforming growth factor-beta (TGFB)/bone morphogenetic protein (BMP) signaling pathway is related to many cellular processes and is essential for the regulation of cell proliferation, differentiation, apoptosis, migration, and extracellular matrix remodeling (LIU et al., 2009). Bone morphogenetic proteins are members of the TGFB superfamily and contribute to endochondral bone formation, healing, and regeneration and increase osteoblast differentiation. Although there are more than 20 of these osteogenesis factors, only some of them have exhibited osteoinductive potential (HAQUE et al., 2008; HERZOG et al., 2014). BMP2, BMP4, BMP6, and BMP7 are known for their ability to induce osteoblastic differentiation and bone formation, with BMP2 and BMP4 being the most important ligands during bone and cartilage development, and some problems such as limb fractures can appear when the function of these receptors is interrupted (CASTRO-RAUCCI et al., 2016). Castro-Raucci *et al.* found that nanotopography induces osteoblast differentiation since it promotes the endogenous production of BMP2, this suggests that this receptor has greater osteogenic potential of nanotopography than BMP4, which was not expressed (CASTRO-RAUCCI et al., 2016; LATTANZI; BERNARDINI, 2011). BMP2 is part of the principal group of bone morphogenetic factors that are involved in skeletal repair, postnatal development of skeletal tissue, and modulate the formation of vessel networks (HERZOG et al., 2014). Different studies have found that when BMP2 is introduced into *in vitro* cultures, it increases the mineralization process (ATARI et al., 2012; MAREDDY et al., 2010).

TGF-β/BMP signaling plays an important role in the regulation of bone organogenesis, which is mediated by the interaction of two types of serine-threonine kinase, BMPR1A or BMPR1B and BMPR2 (HAQUE et al., 2008; RAHMAN et al., 2015). Normally, signal transduction is initiated by bringing together BMPR1 and BMPR2 receptors on the cell surface to form a complex that is necessary for the signal propagation (RAHMAN et al., 2015). The receptor complex is activated by inducing phosphorylation of type I receptor by type II receptor. Then, type I receptor induces phosphorylation of SMAD-1/5/8; next, activated SMAD-1/5/8 forms a heterotrimeric transcription complex with SMAD4 (HAQUE et al., 2008). This permits the migration of the complex to the nucleus facilitating the interaction with different factors such as osterix, SOX9, and RUNX2, which play essential roles in some signaling pathways during osteogenesis. Moreover, the complex has the option to binds directly to DNA (HAQUE et al., 2008).

When osteogenesis occurs by the BMP signaling pathway, it can be activated through either the SMAD pathway as was described above or the MAPK pathway that is non-SMAD-dependent signaling and is activated by growth factors such as TGFB, FGF, IGF and VEGF (HAQUE et al., 2008). Other ways to regulate BMP activity is by antagonists such as BMP3, a negative regulator that can bind directly to BMP receptors as a potent antagonist. This factor obtained by mature bone cells interacts with the type II receptor ACVR2B, reducing BMP signaling and limiting osteogenic differentiation (HAQUE et al., 2008; KOKABU et al., 2012).

2.12.1 RUNX2, Osterix, and SOX9

BMP2 signaling is performing downstream of SMAD cascade by means of the recruitment of specific transcription factors, and the best-known one is Runt-related transcription factor 2 (RUNX2). This can induce gene expression of ALP, osteocalcin, osteopontin, bone sialoprotein, and collagens (LATTANZI; BERNARDINI, 2011). RUNX2 is an important factor that regulates osteoblast differentiation during both endochondral and intramembranous ossification, being fundamental during skeletal development and inducing cell commitment and maturation of osteoblasts in postnatal development (LONG, 2012). Moreover, RUNX2 controls bone resorption of osteoclasts, which enables regulation of bone formation and is crucial for the adequate function of mature osteoblasts (LONG, 2012; WU; LU, 2008). Almost all signaling pathways related to osteogenic differentiation are targeted at RUNX2 (CHEN et al., 2016). Being the “master regulator” of osteoblast development, the reduction of its signaling can affect several osteoinductive genes essential for differentiation, and the complete absence of its signaling generates deficit in skeletal components (VLACIC-ZISCHKE et al., 2011). There is a deeply relationship between RUNX2 and BMP-SMAD signaling pathway, it has been found that activated SMAD1/5 and SMAD4 can upregulate RUNX2 expression, then all of them form a complex that collaboratively induces osteoblast differentiation and bone formation through different mechanisms as shown in Figure 2.15 (NISHIMURA et al., 2012a; WU; LU, 2008). Also, RUNX2 expression can be upregulated by BMP2 and TGFβ (WU; LU, 2008).

Osterix also named SP7 is a BMP2 specific transcription factor that is essential for osteoblast differentiation and is specifically expressed in all developing bones. Nakashima *et al.* observed that SP7 null mice were not able to produce osteoblasts, although the expression of RUNX2 was normal (NAKASHIMA et al., 2002). This factor is also very important for osteocyte differentiation (LONG, 2012). As can be seen in Figure 2.15, SMAD signaling is related to induction of SP7 by RUNX2 and BMP2. Similarly, it has been found that RUNX2 and SP7 have the ability to upregulate the same genes such as osteocalcin and bone sialoprotein, which are vital in osteogenesis, but furthermore, they upregulate the expression of different genes, this evidences that they perform both equal and different function during osteogenic process (NISHIMURA et al., 2012a).

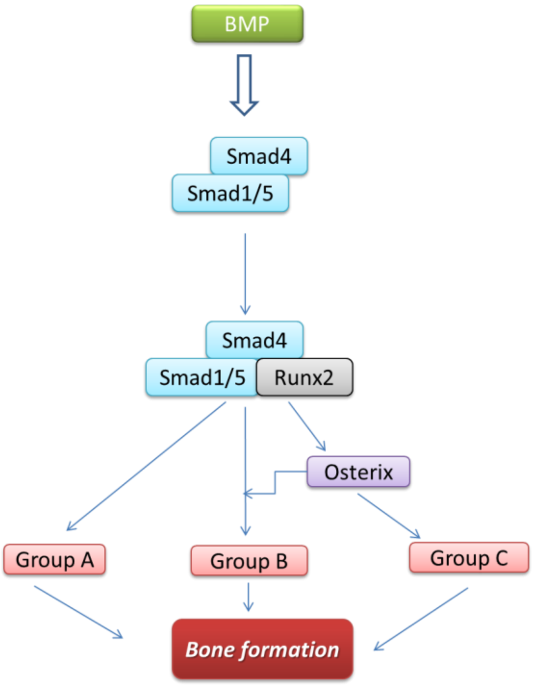

Figure 2.15 - RUNX2 in conjunction with SMAD signaling induces osterix. RUNX2 and osterix (SP7) regulate common (Group B) and different (groups A and C) target genes, being all necessary for bone formation. Adapted from (NISHIMURA et al., 2012a).

SOX9 is a transcription factor that is important for condensation of mesenchymal cells and is vital for skeleton development (LOEBEL et al., 2014; MINAŘÍKOVÁ et al., 2015). This protein is required for differentiation of mesenchymal cells into chondrocytes and for synthesizing the mesenchymal progenitors that differentiate into osteoblasts (KARSENTY; KRONENBERG; SETTEMBRE, 2009). In spite of these features, the role of SOX9 in osteogenesis of human mesenchymal stem cells (hMSCs) *in vivo* and *in vitro* is not well understood. It is known that this factor is not expressed for the mature osteoblasts and its deletion can produce either lack of chondrocytes and osteoblasts or total absence of endochondral bone; however, intramembranous bones can be formed relying on the type of cells tested (AKIYAMA et al., 2002; LONG, 2012; MORI-AKIYAMA et al., 2003). Loebel *et al.* found that during the early stage of osteogenic differentiation *in vitro*, SOX9 acts as an osteogenic regulator, being the osteogenic differentiation potential of hMSCs determined by the ratio between RUNX2 and SOX9 (LOEBEL et al., 2014).

2.12.2 FGF signaling

Fibroblast growth factors (FGFs) and corresponding receptors (FGFRs) are a large family that performances remarkable biological function during bone development in vertebrate (LONG, 2012). FGF signaling is essential for maintaining bone homeostasis and controlling cell proliferation and differentiation during osteogenesis and tissue repair (MAREDDY et al., 2010). These polypeptides have a crucial role in the angiogenesis process, inhibit apoptosis in osteoblasts and increase osteoclast differentiation (CHEN et al., 2016; GINER et al., 2013). This family comprises 22 structurally related members in humans and mice, and most of them are activated by binding to tyrosine kinase transmembrane receptors such as FGFR1-FGFR4 (LATTANZI; BERNARDINI, 2011; LONG, 2012). After binding FGFR on its extracellular ligand-binding domain, receptor monomers are submitted to dimerization inducing phosphorylation of tyrosine residues of signaling proteins and activating several signaling modules, being all important for regulating MSCs differentiation (CHEN et al., 2016; LATTANZI; BERNARDINI, 2011). As a result, FGF2, FGF4, and FGF8 can upregulate other factors such RUNX2; and FGF2 can induce ALP and stimulate mineralization (CHEN et al., 2016). As is known, all these signaling pathways work together to define lineage commitment of MSCs. Additionally, transcription factors can participate in different pathways, such as BMP2, that plays a role not only in osteogenesis but also in adipogenesis of MSCs (CHEN et al., 2016). Moreover, they can have different functions in the same differentiation process, regulating the function of other factors. For example, FGFR1 can foster osteoblast differentiation in the early stage without hindering RUNX2 expression; nevertheless, in the later stage of osteogenesis, this factor can inhibit the mineralization (LONG, 2012).

2.13 Cell-cell communications and adhesion

Multicellular organisms are recognized for having a complex cellular coordination that assures their survival. Cells need to coordinate cellular activities through cell communication, which actives processes such as cell growth, proliferation, and migration. To achieve these goals, cells have developed different types of mechanisms, such as short-range interactions that can be produced by direct physical or cell-cell contact (KUMAR; GILULA, 1996). Cell adhesion is the capacity of a cell to adhere to another cell or to the ECM and plays an important role in cell communication because it induces signals that regulate cell proliferation, migration, and differentiation. For these reasons, it is vital that biomaterials used for bone regeneration foster cell adhesion to induce cell growth, proliferation, and bone formation (KHALILI; AHMAD, 2015).

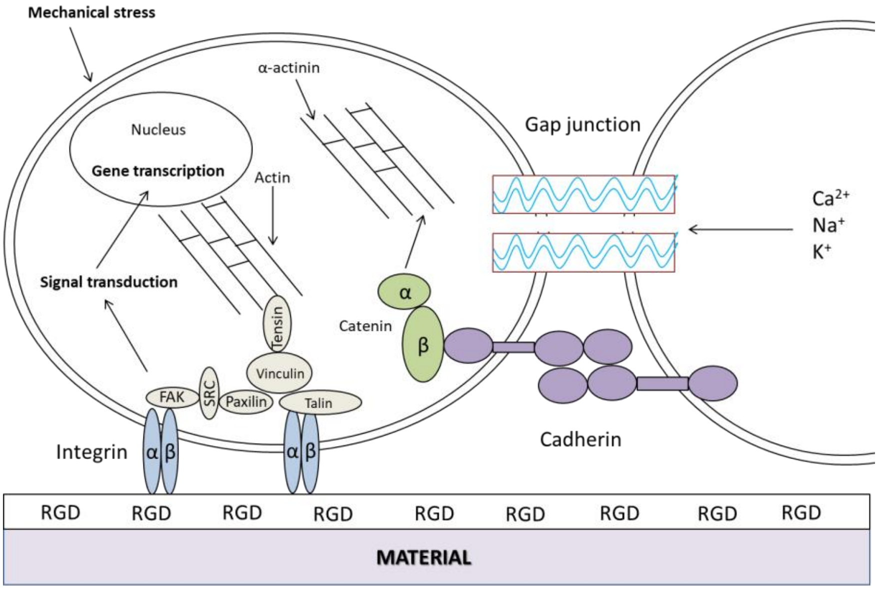

Figure 2.16 - Representation of the cell proteins involved in cell adhesion on biomaterial (ANSELME, 2000).

Signal transduction is the transmission of chemical or physical signals through a cell, generating a cellular response and this mechanism is initiated by cell-surface receptors. Between the mechanisms (Figure 2.16) involved in cell adhesion are: cell-substrate adhesion that consists in the cell adhesion to the ECM or a substrate and is mediated by integrins; cell-cell adhesion that permits interaction between neighbouring cells and is mediated by cadherin and gap junction, which is a kind of cell communication mediated by connexins and consists in the construction of channels that mediate the flux of different molecules between neighbouring cells (ANSELME, 2000; KUMAR; GILULA, 1996).

2.13.1 Cell-substrate adhesion

When cells and biomaterials get in contact, specialized molecules mediate cell attachment, which can be classified such as short-term events or adhesion phase. In short-term events, cells and material are joined by physicochemical bonds such as ionic forces or Van der Walls forces. Adhesion phase involves different biomolecules such as extracellular matrix proteins, cell membrane proteins, and cytoskeleton proteins, which act together to regulate gene expression (ANSELME, 2000; GRZESIK, WOJCIECH J, ROBEY, 1994). Adhesion molecules are known for playing an important role in adhesion since they are able to interact with specific ligands, with integrins and cadherins being the molecules involved in the adhesion process in osteogenesis. The integrins are transmembrane proteins formed by two bound sub-units that connect both sides of the membrane (ANSELME, 2000; PHILIP, 2016). The domain of integrin exposed to the external medium binds to a specific ligand of the material or the ECM and the domain exposed to the cytoplasm activates intracellular proteins such as talin and catenin. In general, when the ligand binds to the extracellular domain, conformational changes are generated and transmitted to the intracellular domain. This produces intracellular modifications that are necessary for cell adhesion, spreading, and migration, which foster cell growth and osteogenic differentiation (ANSELME, 2000; PHILIP, 2016). Figure 2.17 shows the focal adhesion (FA) complex that keeps connect integrins and adhesion molecules to the actin filaments by FA proteins, playing an essential role in mechanotransduction because it transmits adhesive and traction forces to the cytoskeleton (KHALILI; AHMAD, 2015).

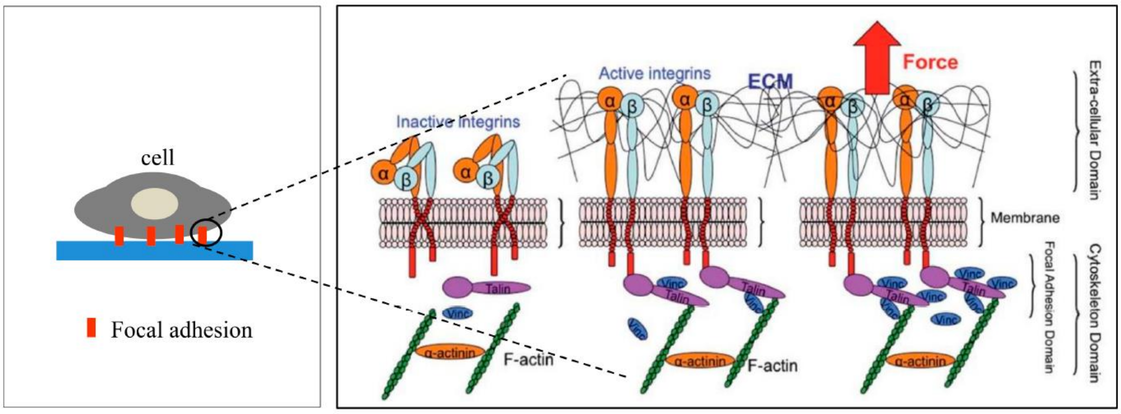

Figure 2.17 - Schematic representation of activated integrin and formation of ECM-integrin-cytoskeleton linkages in the focal adhesion site upon application of an external tensile load (KHALILI; AHMAD, 2015).

Focal contact is the place where *in vitro* cells adhere to the material surface keeping a distance from 10 nm to 15 nm; indeed, fibronectin and vitronectin facilitate the formation of focal contacts for *in vitro* cultures, and substrates without vitronectin have showed deficient cell attachment and spreading (ANSELME, 2000; CAMERON et al., 2012). It has been found that some bone proteins such as fibronectin, osteopontin, bone sialoprotein, thrombospondin, type I collagen and vitronectin possess adhesion properties since they have a specific sequence of three aminoacids: arginine, glycine and aspartic acid (Arg-Gly-Asp), named RGD sequence, that is recognized by cell surface receptors such as integrins (ANSELME, 2000; GRZESIK, WOJCIECH J, ROBEY, 1994). hMSCs can adhere to substrates coated with type I and IV collagen, fibronectin, and vitronectin, being strongly differentiate in type I collagen and vitronectin (WANG; CHEN, 2013).

Another key point is that the chemical properties of the surface influence the morphology of osteoblasts; as a matter of fact, cell shape and differentiation are strongly related. Therefore, remodeling through assembly and disassembly of the actin cytoskeleton is a determinant factor in osteogenesis. Another important feature is that cells can adhere better to a hydrophilic surface than to a hydrophobic one, generating an increased spreading of cells on materials. Anselme *et al.* studied the adhesion of human osteoblasts on metallic materials with different surface roughness and found a homogenous generation of focal contacts on cell membranes in contact with smooth surfaces (ANSELME et al., 2004; KIESWETTER et al., 1996).

2.13.2 Cell-cell adhesion and gap junctions

Cell-cell adhesion permits the connection between neighboring cells by cadherins. These molecules are transmembrane glycoproteins that recognize specific ligands on the membrane of neighboring cells or the ECM and can connect with the intracellular environment by catenins, which interact with intracellular proteins, as shown in Figure 2.16 (ANSELME, 2000). This process is important for cell fate decisions in adult bone marrow mesenchymal stem cells and is vital for the formation of the gap junctions (STAINS; CIVITELLI, 2005).

The gap junction is a particular type of cell-cell interaction that is formed by two hemichannels put side by side connecting adjacent cells (Figure 2.16); this transcellular channel is like a bridge through which the ions, metabolites and second messengers can easily move (ANSELME, 2000). The main structural component of the channels is a family of integrin membrane proteins known as connexins, and the basic unit of structure or hemichannel is a hexameric array of connexion subunits. They can form channels with different charge, permeability and molecular size, and their molecular permeability and electric conductance can be regulated by phosphorylation and membrane voltage. These channels can assemble signaling complexes such as protein kinase C, cscr, and catenin. These channels are almost permeable to hydrophilic molecules whose diameters are equal to or smaller than 1.5 nm (KUMAR; GILULA, 1996). When cell communication through gap junction is inhibited, a decrease in osteogenic gene expression and mineralization has been observed. These connexions between neighboring cells by cadherins and gap function are vital for the osteogenesis process because these different signaling cascades can induce and modify gene transcription (STAINS; CIVITELLI, 2005).

2.14 Ceramics in osteogenic differentiation

Ideal biomaterials for bone tissue engineering should lead to osteogenic differentiation of mesenchymal stem cells. Many studies have shown that inorganic substrates such as HA, bioglasses, Biosilicate, and calcium phosphate are capable of stimulating osteogenic differentiation with or without osteogenic factors, making them promising candidates for applications in bone tissue engineering and regenerative medicine (CAMERON et al., 2012; MAHDAVI et al., 2017; RAMEZANIFARD et al., 2016; ZHAI et al., 2013). Ramezanifard *et al.* found that ASCs cultured on willemite-coated poly (L-lactide acid) (PLLA) showed higher ALP activity, calcium formation, and gene expression of some important osteogenic factors such as osteonectin, RUNX2, COLI, and osteocalcin than those ones cultured on PLLA (RAMEZANIFARD et al., 2016). Cameron *et al.* assayed osteogenic differentiation of MSCs in the absence of soluble factors using silicate-substituted calcium phosphate (Si-CaP) and unmodified HA. Si-CaP stimulated both cell adhesion and proliferation and induced a higher up-regulation of some osteoblast-related genes such as ALP, RUNX2, COL1A1, and BGLAP as well as better mineralization (CAMERON et al., 2012). Mahdavi *et al.* evaluated the osteogenic potential of equine adipose-derived stem cells (e-ASCs) over a nano-bioactive glass (nBGs) coated PLLA nanofibers scaffold and demonstrated that the nBGs-PLLA scaffold induced significantly higher ALP activity, calcium content, and expression of bone-related genes compared with PLLA scaffold without glass coating (MAHDAVI et al., 2017). Zhai *et al.* investigated the osteogenic differentiation of human bone marrow mesenchymal stem cells (hBMSCs) using bredigite ($Ca_7MgSi_4O_{16}$), akermanite ($Ca_2MgSi_2O_7$) and diopside ($CaMgSi_2O_6$). They found that ionic extracts of these ceramics enhanced the expression of some osteogenic factors such as COLI, ALP, OCN, BSP, and osteopontin, and this effect augmented with the increase of Si concentration in the extract (ZHAI et al., 2013).

3 MATERIALS AND METHODS

3.1 Foams

For the preliminary tests, a fully reticulated polyurethane (PU) foam with 35 pores per inch (ppi) was used as the sacrifice template for the replication method. This sponge was fabricated by Foam Partner (Germany) and was cut with a foam cutter (Depron/MP-30) based on the requirements of suitable ASTM F2883-11 standards for compressive strength tests of the scaffolds. PU foam (35 ppi) was cut into square prisms of 15x15x30 mm^3. The square prism-shaped foams were designated as 860SP-PU foams, 860 is related to foam pore size and SP to foam shape.

For the other tests, a fully reticulated polyurethane (PU) foam with 45 ppi was used as the sacrifice template for the replication method. This sponge was donated by Recticel (Belgium) and was cut with a foam cutter (Depron/MP-30); this foam was named 590-PU foam, 590 is related to foam pore size. PU foam (45 ppi) was cut into rectangular prisms of 80x50x30 mm^3. Rectangular prism-shaped foams were designated as 590RP-PU foam, 590 is related to foam pore size and RP to foam shape. Also, 45 ppi foam was cut into a cylindrical shape with a diameter of 15 mm and a length of 30 mm to fulfill the requirements of suitable ASTM F2883-11 standards for compressive strength tests of the scaffolds. This foam was designated as 590C-PU foam, 590 is related to foam pore size and C to foam shape.

3.2 Glass preparation

For the preparation of 300 g of glass precursor, Na_2CO_3 (Vetec), $CaCO_3$ (PA-JT Baker), SiO_2 (Zetasil2-Santa Rosa Mining Co.), and Na_2HPO_4 (PA-JT Baker) were used. After weighing on an analytical balance, the raw materials were mixed in a mixer (Solab) at 30 rpm for 12 hours.

Fusion was performed in an electrical furnace (Deltech/DT-33-RS-812-C), which was preheated to 1350 °C. The mixture was slowly put into a crucible inside the furnace. When all the powder was placed in the crucible, the mixture was fused for one hour. Then, the glass was poured into the water and remelted again. This process was carried out three times to obtain glass frits smaller than 5 mm. Finally, the glass was dried in an oven at 100 °C for 12 h.

F18 glass powder with an average particle size (APS) ~ 5 μm was kindly provided by Vetra High-Tech Bioceramics.

3.3 Milling

Dry glass pieces bigger than 5 mm were broken in a porcelain mortar. Then, those smaller than 5 mm were ground in a mill with rotating discs sprayers (MA700-Marconi), with a gap of 0.5 mm between alumina discs. Subsequently, the obtained powder was ground in a planetary mono mill (Pulverisette6-Fritsch) following the conditions describe below:

- For 860SP-PU foam, the following conditions were used to obtain the Biosilicate powder used for the first and second dipping:

    1. Milling with 30 mm agate milling ball at 500 rpm/30min.
    2. Milling with 20 mm agate milling ball at 500rpm/30min.
    3. Milling with 10 mm agate milling ball at 500 rpm/30min.

- For 590RP-PU and 590C-PU foams, the following conditions were used to obtain the Biosilicate powder used for the first and second dipping:

    1. Milling with 30 mm agate milling ball at 500 rpm/30min.

For the second dipping of 590RP-PU and 590C-PU foams, the conditions used for 860SP-PU foam, described above, were used too.

3.4 Particle size distribution measurements (PSD)

The PSD measurements were performed in a particle size analyzer (Horiba-LA-93). As medium was used isopropyl alcohol (99.5%-QHEMIS). It was added 75 mg of glass or Biosilicate powder in 30 mL isopropyl alcohol. The mixture was added in the analyzer drop by drop until around 90% transmission

(%T) and particle size distribution measurements were registered for each slurry.

3.5 Biosilicate and F18 slurry preparation

Different slurries of Biosilicate (125 mL) and F18 (125 mL) were prepared using the concentrations describe in Table 3.1. Each mixture was homogenized in a planetary mono mill (Pulverisette6-Fritsch) and the conditions used depended on foam size and shape.

Table 3.1 - Concentration of the reagents used to prepare the slurries.

Slurry	Biosilicate %(v/v)	PVB %(v/v)	ethyl alcohol %(v/v)	F18 powder %(v/v)
35.BS	35	4	61	-
30.BS	30	4	66	-
25.BS	25	3	72	-
20.BS	20	3	77	-
20.F18	-	3	77	20
15.F18	-	3	82	15

- For 860SP-PU foams, 30.BS, 25.BS and 20.F18 slurries were used and all of them were homogenized with 10 mm agate milling balls at 500 rpm for 2 hours.

- For 590RP-PU foams were used:
  - ✓ 30.BS slurry that was homogenized with 30 mm agate milling balls at 500 rpm for 30 minutes.
  - ✓ 20.BS and 15.F18 slurries that were homogenized with 10 mm agate milling balls at 500 rpm for 2 hours and 30 minutes.

- For 590C-PU foams were used:
    - ✓ 35.BS slurry that was homogenized with 30 mm agate milling balls at 500 rpm for 30 minutes.
    - ✓ 20.BS and 15.F18 slurries that were homogenized with 10 mm agate milling balls at 500 rpm for 2 hours and 30 minutes.

3.6 Scaffold preparation

When the samples deformed during the heat treatment, the sintering temperature and heating rate of Biosilicate were diminished. When the samples deformed during foam burning, the pyrolysis of the foams was carried out in different stages. The best conditions for sintering were chosen based on the surface morphology of the scaffolds; and slurry concentrations were adjusted to avoid closed pores in the reticular structures.

3.6.1 Synthesis of F18-860SP.BioS scaffolds

First, 860SP-PU foam was dipped in 30.BS slurry (section 3.5). Second, the foam was taken out and squeezed to remove the excess of the slurry. Later, the sample was dried for 24 hours at room temperature and this process was repeated one more time. Subsequently, the sintering process was performed in sintering furnace (Incon-CNT120) using the **Heat Treatment 1 (HT1)** described below.

1. Temperature gradient from 30 °C to 410 °C at 1 °C/min.
2. 410 °C for 240 minutes.
3. Temperature gradient from 410 °C to 950 °C at 2.5 °C/min.
4. 950 °C for 180 minutes.
5. Cooling from 950 °C to 30 °C at 5 °C/min.

After sintering, scaffolds synthesized with 860SP-PU foam were tied with floss and hung inside a 45 mL tube that contained 20 mL of 25.BS slurry and some holes through which the air was removed. Then, the tube was closed and put inside a 1000 mL vacuum filter flash, which was closed with a rubber stopper. The flash was connected to a vacuum system and turned on for 2 minutes (Figure 3.1). When all the air in the tube and the scaffold had gone out, the flash was twirled to allow the slurry to be in contact with the Biosilicate scaffold under vacuum conditions. Subsequently, the scaffold was taken out from the tube and the excess of the slurry was removed using compressed air. Finally, the scaffold was dried at room temperature for 24 hours and sintered using the conditions for HT1, described above. This scaffold was named **860SP.BioS**.

Figure 3.1 - Image of the system used to do vacuum and force the slurry gets inside the porous walls. This system was used to carry out the preliminary tests.

Then, 860SP.BioS scaffold was dipped in 20.F18 slurry using the system of the Figure 3.1 and the slurry excess was removed by compressed air. Finally, the dry sample was subjected to the **Heat Treatment 2 (HT2)** described below:

1. Temperature gradient from room temperature to 385 °C at 5 °C/min.
2. 385 °C for 180 minutes.
3. Temperature gradient from 385 °C to 800 °C at 5 °C/min.
4. 800 °C for 180 minutes.
5. Cooling to room temperature.

F18 coating was repeated three more times, using the same conditions mentioned above. And this scaffold was named **F18-860SP.BioS.**

3.6.2 Synthesis of F18-590RP.BioS scaffolds

A better vacuum system (Figure 3.2) was designed, which permitted easier handle of the samples during infiltrations, and the vacuum used in each assay was standardized to 500 mmHg. This system was used to infiltrate the scaffolds synthesized with 590RP-PU and 590C-PU foams.

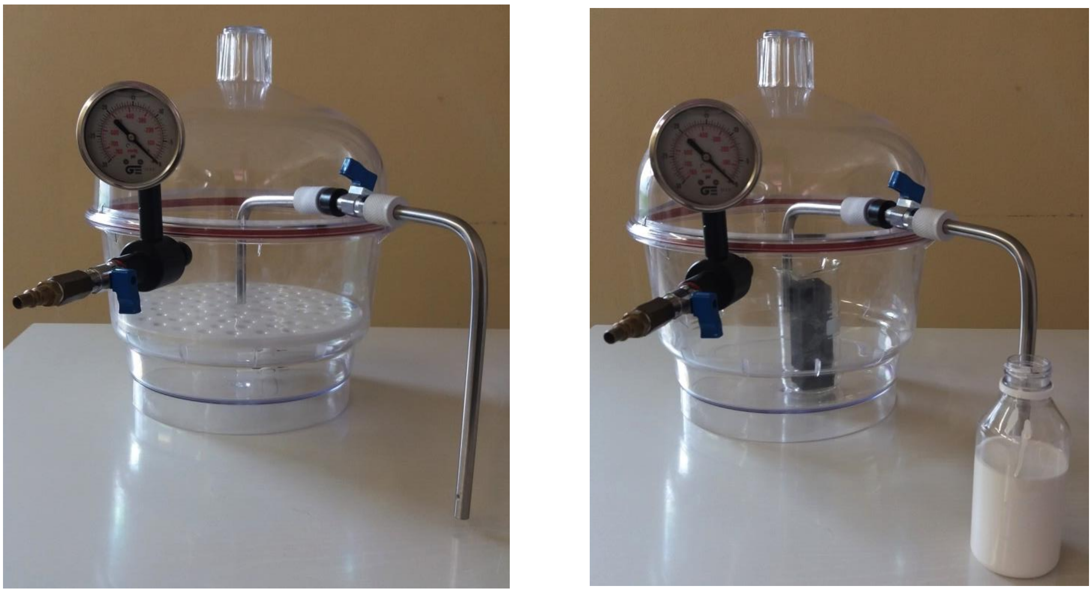

Figure 3.2 - Vacuum system to infiltrate scaffolds during second, third, fourth, fifth and sixth dipping.

First, 590RP-PU foam was dipped in 30.BS slurry (section 3.5). Second, the foam was taken out and squeezed to remove the excess of slurry. Later, the sample was dried for 24 hours at room temperature; this process was carried out only one time to avoid the sponge deformation produced by its large size. Subsequently, the sintering process was performed in a sintering furnace (Incon-CNT120) using the **Heat Treatment 3 (HT3)** described below.

1. Temperature gradient from 30 °C to 410 °C at 1 °C/min.
2. 410 °C for 240 minutes.
3. Temperature gradient from 410 °C to 900 °C at 2.5 °C/min.
4. 900 °C for 180 minutes.
5. Cooling from 900 °C to 30 °C at 5 °C/min.

After sintering, the scaffold synthesized with 590RP-PU foam, together with the slurry, was subjected to vacuum (Figure 3.2). Then, the scaffold was infiltrated with 20.BS slurry (Table 3.1) for three minutes under vacuum. Subsequently, the scaffold was taken out from the vacuum system and the excess of the slurry was removed using compressed air. Finally, the scaffold was dried at room temperature for 24 hours and sintered using the **Heat Treatment 4 (HT4)** described below. This scaffold was named **590RP.BioS**.

1. Temperature gradient from 30 °C to 410 °C at 1 °C/min.
2. 410 °C for 240 minutes.
3. Temperature gradient from 410 °C to 975 °C at 2.5 °C/min.
4. 975°C for 180 minutes.
5. Cooling from 975 °C to 30 °C at 5 °C/min.

Then, 590RP.BioS scaffold was dipped in 15.F18 slurry using the system of the Figure 3.2 and the slurry excess was removed by compressed air. Finally, the dry sample was subjected to the heat treatment 2 described in the section 3.6.1. This process was repeated three more times, using the conditions that were already mentioned. And this scaffold was named **F18-590RP.BioS.**

3.6.3 Synthesis of F18-590C.BioS scaffolds

First, 590C-PU foam was dipped in 35.BS slurry (section 3.5). Second, the foam was taken out and squeezed to remove the excess of slurry. Later, the sample was dried for 24 hours at room temperature and this process was repeated one more time. Subsequently, the sintering process was performed in a sintering furnace (Incon-CNT120) using the **Heat Treatment 5 (HT5)** described below.

1. Temperature gradient from 30 °C to 280 °C at 1 °C/min.
2. 280 °C for 60 minutes.
3. Temperature gradient from 280 °C to 380 °C at 1 °C/min.
4. 380 °C for 60 minutes.
5. Temperature gradient from 380 °C to 410 °C at 1 °C/min.
6. 410 °C for 60 minutes.
7. Temperature gradient from 410 °C to 900 °C at 2.5 °C/min.
8. 900°C for 180 minutes.
9. Cooling from 900 °C to 30 °C at 5 °C/min.

After sintering, the scaffold synthesized with 590C-PU foam, together with the slurry, was subjected to vacuum (Figure 3.2). Then, the scaffold was infiltrated with 20.BS slurry (Table 3.1) for three minutes under vacuum. Subsequently, the scaffold was taken out from the vacuum system and the excess of the slurry was removed using compressed air. Finally, the scaffold was dried at room temperature for 24 hours and sintered using the conditions for HT3 described in the section 3.6.2. This scaffold was named **590C.BioS**.

Then, 590RP.BioS scaffold was dipped in 15.F18 slurry using the system of the Figure 3.2 and the slurry excess was removed by compressed air. Finally, the dry sample was subjected to TH2 described in the section 3.6.1. This process was repeated three more times, using the conditions that were already mentioned. And this scaffold was named **F18-590C.BioS**.

3.7 Scaffold characterization

3.7.1 Thermogravimetric analysis (TGA)

PU foams were analyzed by TGA to determine the best temperature to remove them by pyrolysis. These assays were carried out under environmental conditions using the thermal analysis equipment (TGA Q500-TA instrument) of the Materials Characterization & Development Center (DEMA/UFSCar). The tests were carried out in platinum crucibles and the heating rate used was 1 °C/min from 25 °C to 950 °C. Moreover, TGAs for PVB and foam coated with Biosilicate slurry were carried out.

3.7.2 Scanning electron microscopy (SEM)

SEMs were performed to observe the microstructures of the sintered samples obtained by the replicate technique. It was utilized FEG Philips (XL-30) equipment from the structural characterization laboratory (LCE-DEMa/UFSCar) and FEI (PHENOMTM) equipment from the vitreous material laboratory (LaMaV/UFSCar). The samples were covered with gold for 180 seconds.

FEI Inspect S50 was used to carry out chemical microanalysis to analyze contamination in samples. These assays were done in the structural characterization laboratory (LCE-DEMa/UFSCar).

3.7.3 Porosity and pore size determination

Porosity was calculated using the geometric method for five 860SP.BioS, five F18-860SP.BioS, and ten F18-590C.BioS scaffolds. First, it was measured the length, height, and width of the prisms on their four faces or the diameter and height for the cylinders. Then, the average volume of the different test bodies was calculated. Subsequently, the average density of each scaffold was calculated using its weight. Finally, the average porosity for each type of scaffold was determined using equation 3.1, where Biosilicate density value is 2.79 g.cm^{-3}.

$$Porosity = 100 - \left(100 * \left(\frac{scaffold\ density}{Biosilicate\ density}\right)\right) \tag{3.1}$$

Average size of pores was measured using Image-J software.

3.7.4 Compression strength

Measurements of compressive strength were calculated for five 860SP.BioS, five F18-860SP.BioS, and ten F18-590C.BioS scaffolds. The parallel faces of the scaffolds were tied with epoxy resin to aluminum discs with 32 mm diameter and 2.5 mm thickness (Figure 3.3). These assays were carried out in a mechanical testing system (Instron-4467 model), with a load cell of 50N and a rate of 0.5 mm/min. Data acquisition starts at a minimum compression strength of 0.005 MPa.

Figure 3.3 - Mechanical testing system (Instron-4467 model).

3.8 Cell culture

Different factors related to osteogenesis were assayed to evaluate the potential of the scaffolds to induce osteogenesis in stem cells. All processes were done following manufacturer’s indications.

Human adipose-derived mesenchymal stem cells (hASCs) were purchased from Sciencell and maintained under nitrogen atmosphere in

Locator™ Plus Rack and Box Systems (Thermo Scientific-model 316306). All cell culture processes were carried out in a biological safety cabinet (Microzone Corporation-model BK-2-4) under sterilized conditions.

At 2-4 passage, hASCs were cultured in 24-well plates (Cellstar®-Greiner) using Mesenchymal Stem Cell Medium (MSCM) (Sciencell-Canada) in a humidified incubator (Thermo Scientific-Steri-Cycle) for 4 days at 37 °C with 5% CO_2 until confluent. The medium was changed every 2 days. To differentiate these cells into mature osteoblastic cells, hASCs were seeded in Mesenchymal Stem Cell Osteogenic Differentiation Medium (MODM) (Sciencell- Canada) at a density of 1 x 10^5 cells.cm^{-2}. MODM was changed every 3-4 days for 7, 14, or 21 days relying on the tests. The samples treated in this way were used as the controls. Also, hASCs were passaged over F18 glass-coated 590.BioS scaffolds. The scaffolds were previously sterilized in a convection oven (Thermo Scientific-model 6520) at 180 ºC for three hours. Then, the scaffolds were immersed for 1 hour in a vitronectin solution, and hASCs were passaged over the scaffold at a density of 1 x 10^5 cells.cm^{-2} following the same procedure used for the controls. Additionally, the ions of the scaffolds were extracted in MODM as follows: 10 mL of MODM were left for 48 hours with 1 g of the scaffold in an incubator at 37 °C with 5% CO_2 in a humidified incubator; then, the mixture was filtered with a sterilized syringe filter (VWR-Ø 0.2 µm) and MODM was added until reaching a final volume of 50 mL. These dissolution products (osteogenic medium) were used to differentiate hASCs following the same procedure used for the controls.

The concentration of calcium ions was determined by a photometric method, the concentration of phosphate groups was determined by a UV photometric method, and the concentration of sodium ions was established with an ion-selective electrode at the Maricondi Laboratory (São Carlos-Brazil).

3.9 Evaluation of cell viability

Live/Dead staining was performed for the control, F18 glass-coated 590.BioS scaffolds and the dissolution product group. The staining solution was prepared added 2 µl Calcein AM (Invitrogen-Life Technologies) and 4 µL ethidium homodimer-1 (Invitrogen-Life Technologies) in 2 mL of PBS and mixed. Then, the staining solution was added on the scaffolds (1 mL), the controls (0.5 mL) and the dissolution product group (0.5 mL) and incubated for 30 minutes at room temperature. The cells were observed using a microscope with a fluorescence light source (Lumen Dynamics-X-Cite series 120Q). Calcein AM was excited using an optical filter at 488 nm and EthD-1 was excited using an optical filter 543 nm.

3.10 **Alkaline phosphatase (ALP)**

ALP activity was determined by both staining and colorimetric quantification.

3.10.1 Colorimetric quantification

ALP quantification was performed for the control, F18 glass-coated 590.BioS scaffolds and the dissolution product group. After 7, 14, and 21 days of culture, ALPase activity of cells was determined using ALP Colorimetric Assay Kit (Abcam-Canada) according to the manufacturer’s instruction. This method uses *p*-nitrophenyl phosphate (pNPP) as a phosphatase substrate that dephosphorylates in the presence of ALP, producing yellowish *p*-nitrophenol (OD_{max} = 405 nm).

Cells were washed with cold PBS (Gibco) and resuspended in 50 µL of assay Buffer. Then, they were homogenized using a Dounce homogenizer and centrifuged at 4°C at 1000 rpm for 15 minutes. 5 µl of this lysate was added to a 96-well plate (Cellstar®-Greiner) with 75 µl assay buffer and 50 µL *p*NPP. The samples were covered to protect them from light for 1 h at 25 ºC. Then, 20 µl of Stop Solution (NaOH) was added to the wells and the outputs were measured at O.D. 405 nm on a microplate reader (Tecan-USA). Enzymatic activity was normalized to DNA content measured using a NanoVue Plus spectrophotometer (GE Healthcare). ALP activity was expressed as $\mu mol.min^{-1}.mL^{-1}.\mu g^{-1}$ DNA. To compare with the 3D scaffolds, we measured the ALP activity for a dense specimen of Biosilicate (F18-BioS), i.e., without the porous scaffold structure (Annex E).

With the calculated amounts of *p*NP for different known samples, the standard curve was plotted and ALP activity (μmol/min/mL or U/mL) in the test samples was calculated using equation 3.2.

$$ALP\ Activity\ = \left(\frac{B}{\Delta T\ x\ V}\right) * D \tag{3.2}$$

Where:

B = amount of *p*NP in sample well calculated from standard curve (μmol).

ΔT = reaction time (minutes).

V = original sample volume added into the reaction well (mL).

D = sample dilution factor.

3.10.2 ALP staining

ALP staining was performed for the control, F18 glass-coated 590.BioS scaffolds and the dissolution product group.

SIGMA FAST™ BCIP/NBT (5-Bromo-4-chloro-3-indolyl phosphate/Nitro blue tetrazolium) tablets (Sigma-Aldrich) were used to stain the cells. One tablet, dissolved in 10 mL of water, provides 10 mL of ready-to-use buffered substrate solution. The substrate solution contains BCIP (0.15 mg/mL), NBT (0.30 mg/mL), Tris buffer (100 mM), and $MgCl_2$ (5 mM), pH 9.25-9.75. Nitroblue Tetrazolium (NBT) is used with the alkaline phosphatase substrate 5-Bromo-4-Chloro-3-Indolyl Phosphate (BCIP) in immunohistological staining procedures. These substrate systems produce an insoluble NBT diformazan end product (Figure 3.4) that is blue to purple in color and can be observed visually for the detection of alkaline phosphatase (SIGMA, 2008a).

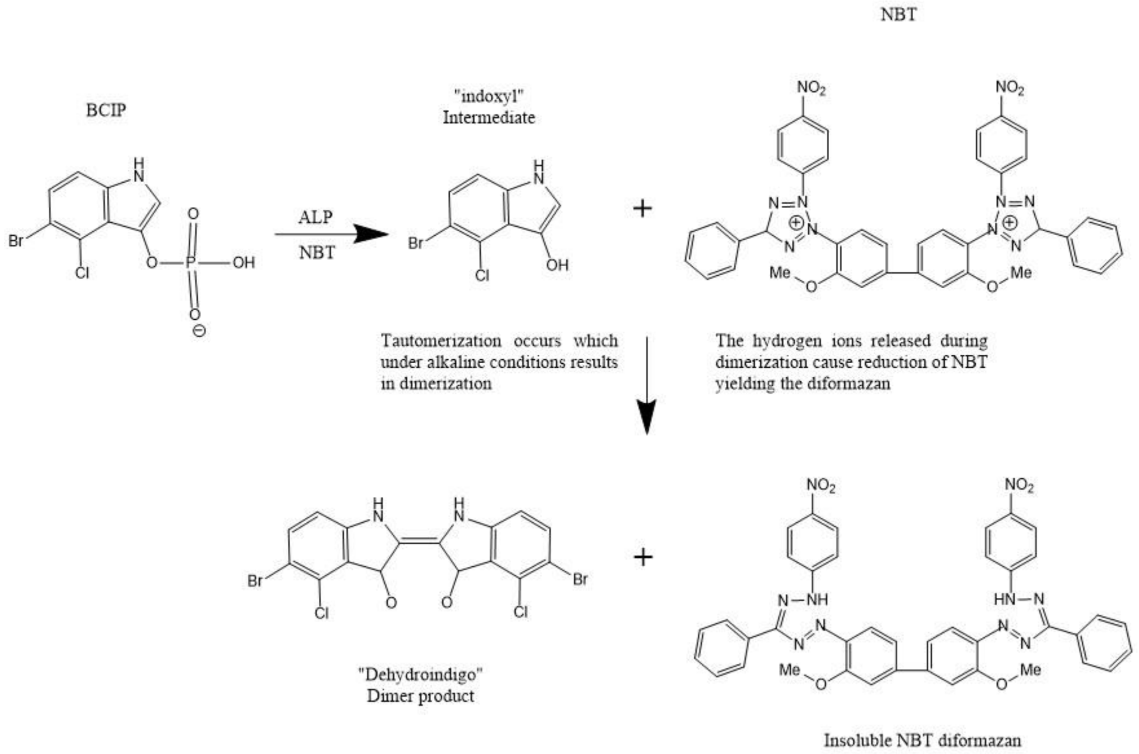

Tautomerization occurs which under alkaline conditions results in dimerization

The hydrogen ions released during dimerization cause reduction of NBT yielding the diformazan

Figure 3.4 - Reaction between Nitroblue Tetrazolium (NBT) and alkaline phosphatase substrate 5-Bromo-4-Chloro-3-Indolyl Phosphate (BCIP) in the presence of ALP that produces an insoluble NBT diformazan, which is blue to purple (SIGMA, 2008b).

Osteogenic medium was removed at 7, 14 and 21 days and the cells were rinsed twice with 0.17 M TRIS-buffer (pH 7.3, 37 °C). 1 mL of BCIP/NBT (Sigma-Aldrich) was added and the preparation was incubated for 10 minutes at room temperature. BCIP/NBT solution was removed and cells were rinsed with deionized water. ALP-positive cells stained blue.

3.11 **Alizarin red S staining quantification**

Mineralization was evaluated quantitatively and qualitatively using ARS. Alizarin Red S, an anthraquinone dye, has been widely used to quantitatively and qualitatively evaluate calcium deposits in cell culture. Osteogenesis can be determined by staining with Alizarin Red Solution, differentiated cells containing calcium deposits stain bright red with the alizarin red solution. ARS staining is quite resourceful because the dye can be pull out from the stained monolayer of cells and readily quantify at 405 nm (MILLIPORE, 2009; SCIENCELL, 2009).

Mineralization was quantitatively and qualitatively evaluated using Alizarin Red S (Sigma) after 7, 14, and 21 days of hASC culture in osteogenic medium. The media and the scaffolds were removed and the cells were washed with phosphate-buffered saline (1xPBS) three times and fixed in 4% formaldehyde (formalin) for 15 minutes at room temperature. Then, these cells were washed three times (5-10 minutes each time) with distilled water. The fixed samples were stained with 40 mM ARS and incubated at room temperature for 30 minutes with gentle shaking. The cells were washed 5 times with distilled water and the plate was inspected using a microscope (Lumen Dynamics-X-Cite series 120Q), and images were taken. After this qualitative test, the plate was stored at -20 °C prior to dye extraction. Next, the stained nodules were incubated in 10% acetic acid (Caledon) and incubated for an extra 30 minutes with shaking at room temperature. The collected cells were heated to 85 °C for 10 minutes and centrifuged at 20,000 x g for 15 minutes. The supernatant was neutralized with 10% ammonium hydroxide (Sigma) and the absorbance was determined at 405 nm. The level of ARS staining in the samples (in moles per liter) was determined according to a linear regression equation derived from a standard curve of known ARS concentrations.

SPSS 25.0 (IBM) software was used for statistical analysis of ALP activity and calcium content. All data were represented as mean ± S.D., and validated by t-test if they complied with the normal distribution and, if not, by the nonparametric Wilcoxon Rank-Sum test. P-values < 0.05 were considered statistically significant. The experiments were repeated in triplicate for each treatment group.

3.12 **RT^2 profiler PCR array human osteogenesis**

Real-Time PCR for RT^2 Profiler PCR Arrays Formats C (Quiagen) was used to analyze the gene expression of 84 human genes related to osteogenesis. Analysis of gene expression was performed for the control, F18 glass-coated 590.BioS scaffolds and the dissolution product group.

hASCs were cultured in 24-well plates and treated according to the same procedure in cell culture item (section 3.8). After 21 days of culture in the osteogenic medium, the cells were washed once in PBS and harvested for total RNA extraction with the RNAeasy Minikit (Qiagen-Canada) according to the manufacturer's protocol. Then, total RNA was converted to cDNA by the proprietary first-strand cDNA synthesis kit included in the PCR array system (Qiagen-Canada). The osteogenic pathway PCR array system (Cat#: PAHS-026Z, Qiagen-Canada) was selected for this study. cDNA and SYBR Green Master Mix were added to each well of the array plate according to the manufacturer's instruction. Real-time PCR was performed on the SteponeplusTM Real-Time PCR system (ThermoFisher Scientific-USA). All target gene expression results were normalized to ACTB, RPLP0, GAPDH, and HPRT1. Statistical analysis and fold change calculations were performed with the provided software at the Qiagen PCR Array Data Analysis web portal (https://geneglobe.qiagen.com/ca/analyze/). Gene expression changes of target genes were compared with the control group using the student’s t-test, and values of $P < 0.05$ were considered to be statistically significant. The experiments were repeated in triplicate for each treatment group.

4 RESULTS AND DISCUSSION

4.1 Compressive strength of bioactive glass scaffolds obtained by the Ryshkewitch and Gibson & Ashby models

It has long been suggested that, because of their low mechanical strength, highly porous scaffolds can be used clinically only in odontology or in craniofacial surgeries, where the biomaterial is not subjected to a high mechanical load. For other orthopaedic applications, scaffold must possess a compressive strength similar to that of cortical bone (100-150 MPa). In this section, two empirical mathematical equations will be used to verify if it is possible to synthesize, using the replica method, a macroporous scaffold keeping remarkable mechanical properties that allow its clinical applications in load-bearing sites.

Diverse studies have reported scaffolds with porosity between 30% to 95% and compressive strength in the range from 0.2 MPa to 150 MPa, being almost all of them in the range of value of mechanical strength for trabecular bone. As is known, mechanical strength can be altered not only for porosity but also for pore size distribution and geometry.

During the 1950s, Ryshkewitch found that mechanical strength of ceramic materials exhibits an exponential reduction with the increase of porosity according to equation 4.1 (RYSHKEWITCH, 1953).

$$\boldsymbol{\sigma_c = \sigma_0 \ \exp(-n.P)} \tag{4.1}$$

Where $\boldsymbol{\sigma_c}$ is the compressive strength of porous ceramic, $\boldsymbol{\sigma_0}$ is the compressive strength of fully dense ceramic, $\boldsymbol{P}$ is open porosity and $\boldsymbol{n}$ is an empirical constant that can vary between 2 and 5.

Figure 4.1 shows the variation of compressive strength with the porosity, estimated using equation 4.1. Since compressive strength for fully dense F18-coated Biosilicate scaffolds is unknown, it was assumed σ_0 = 250 MPa that corresponds to 50% of compressive strength for Bioverit I (σ_0 = 500 MPa), one of the most bioactive glass-ceramics (HOLAND; BEALL, 2002). This value is close to the maximum value found for Biosilicate (~ 220 MPa) (CROVACE et al., 2016). The n values used to calculate the compressive strength were between 2 and 5.

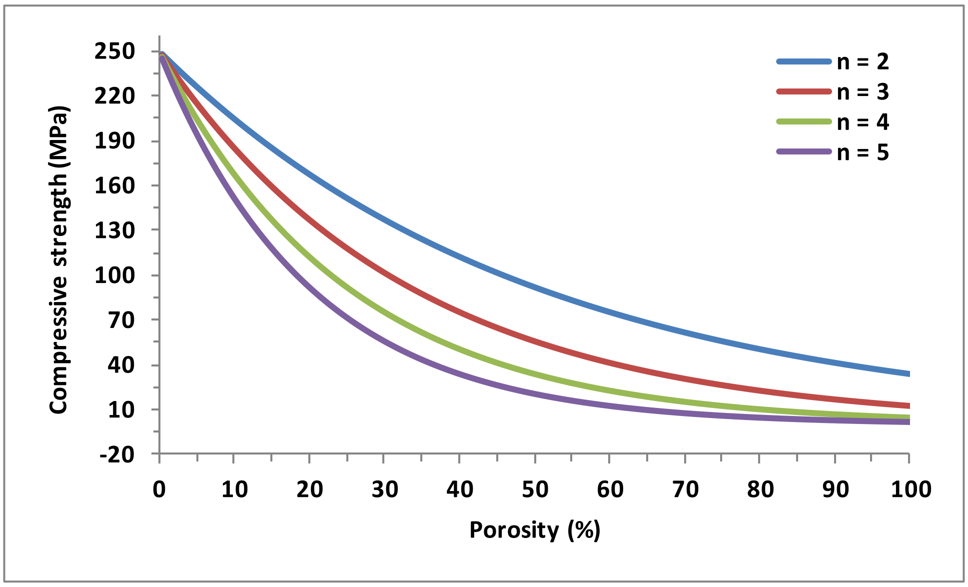

Figure 4.1 - Plot of mechanical strength versus porosity calculated using equation 4.1, with σ_0 = 250 MPa and n values from 2 to 5.

Clearly, σ_c decreased exponentially with the increase of the porosity, being this effect more significant for n = 5 than for n = 2. In different *in vivo* studies have been found that a porosity greater than 70% in volume is vital to obtain an optimal scaffold for bone regeneration. In fact, a porosity of less than 70% hinders angiogenesis and subsequently absorption of the scaffold. In the same way, some researchers believe that a porosity higher than 90% is essential for BTE. In spite of all this information, ideal porosity for bone scaffolds is still under investigation.

Table 4.1 shows the compressive strengths, in a range of porosity values from 70% to 95%, calculated with equation 4.1. When porosity increased from 70% to 95%, it was observed that for n = 2, compressive strength diminished from 62 MPa to 37 MPa; and for n = 5, it decreased from 8 MPa to 2 MPa, respectively. In conclusion, for porosities higher than 70%, no matter what n value is used, it is not possible to get compressive strengths similar to those one of cortical bone (100 - 150 MPa).

Table 4.1 - Mechanical strength (σ_c) for a range of porosity values from 70% to 95%, determined by equation 4.1. Being σ_0 = 250 MPa and n = 2, 3, 4 and 5.

Total porosity (%)	**σ_c (MPa)**			
	n = 2	**n = 3**	**n = 4**	**n = 5**
70	62	31	15	8
75	56	26	12	6
80	50	23	10	5
85	46	20	8	4
90	41	17	7	3
95	37	14	6	2

According to Duckworth (RYSHKEWITCH, 1953), the calculated data obtained with the Ryshkewitch equation do not agreed with the experimental data for high porosities. Later, Gibson & Ashby developed one empirical mathematical model for brittle cellular glass and ceramics with close and open cells (equation 4.2) (GIBSON; ASHBY, 1999).

$$\frac{\sigma_c}{\sigma_0} = \mathbf{0.2} \left(\frac{\rho_{porous}}{\rho_{solido}}\right)^{\frac{3}{2}} \frac{1+\left(\frac{t_i}{t}\right)^2}{\sqrt{1-\left(\frac{t_i}{t}\right)^2}} \tag{4.2}$$

Where σ_c is the compressive strength of porous ceramic, σ_0 is the compressive strength of fully dense ceramic, ρ_{porous} is the density of porous material, ρ_{solid} is the density of the dense material, t_i is the central void diameter of the strut and t is the strut diameter. Figure 4.2 showed t_i and t parameters.

Equation 4.2 was developed for solids with porosity greater than 60%. Indeed, this model fits well for ceramics synthesize by replica technique because these ceramics have hollow struts that are created during foam burning.

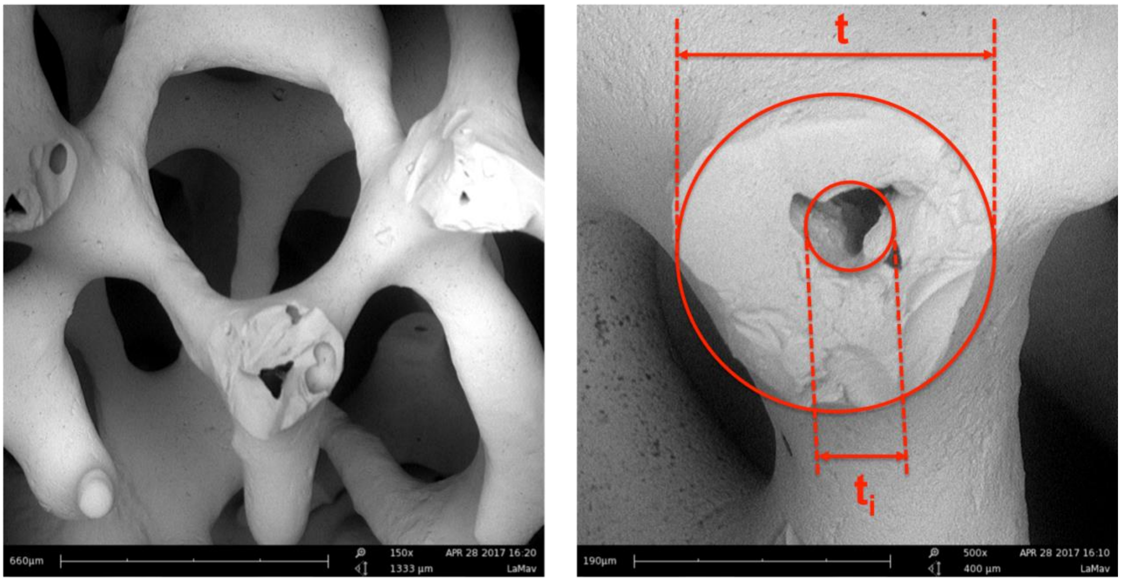

Figure 4.2 - SEM micrographs showing the strut of the scaffold and $\boldsymbol{t_i}$ and $\boldsymbol{t}$ parameters.

Under ideal conditions, the hollow struts are completely dense, the ratio between $\boldsymbol{t_i}$ and $\boldsymbol{t}$ tends to zero. In this case, equation 4.2 is reduced to equation 4.3.

$$\frac{\sigma_c}{\sigma_0} = \mathbf{0.2}\ \left(\frac{\rho_{poroso}}{\rho_{solido}}\right)^{\frac{3}{2}} \tag{4.3}$$

And this modified Gibson & Ashby equation can be rewritten as follows:

$$\frac{\sigma_c}{\sigma_0} = \mathbf{0.2}\ (\mathbf{1} - \boldsymbol{P})^{\frac{3}{2}} \tag{4.4}$$

Being **P** the open porosity of material.

Figure 4.3a shows how the compressive strength, calculated with equation 4.4, varies with porosity for σ_0 = 250 MPa. This plot was compared with the curve calculated using equation 4.1, for σ_0 = 250 MPa and n = 5. And as can be seen in Figure 4.3a, the curve determined using the modified Gibson & Ashby equation exhibited remarkable differences respect to that one calculated using the Ryshkewitch equation, mainly for porosities lower than 50%. Gibson & Ashby equation underestimated σ_c values for low porosities.

Figure 4.3b shows that the curves intersected at a porosity of 79%. And for higher porosities, the compressive strengths estimated using the Gibson & Ashby equation decreased faster than for those calculated with the Ryshkewitch equation.

(a)

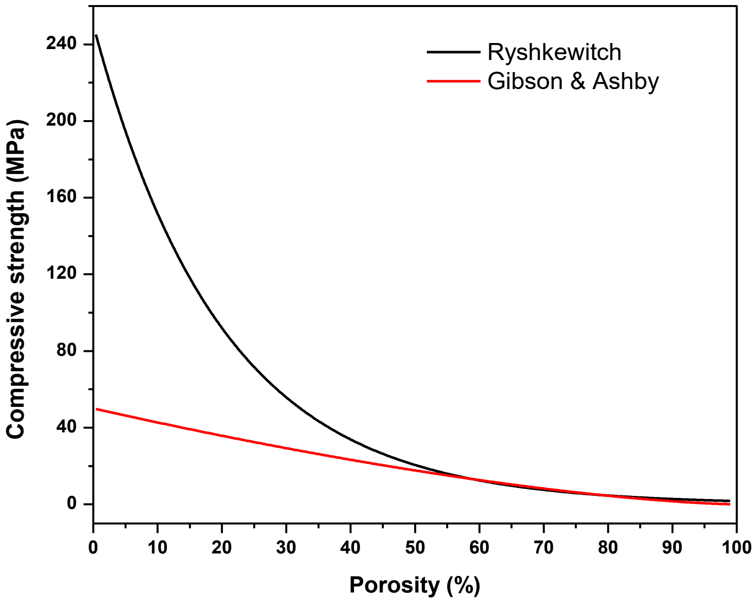

(b)

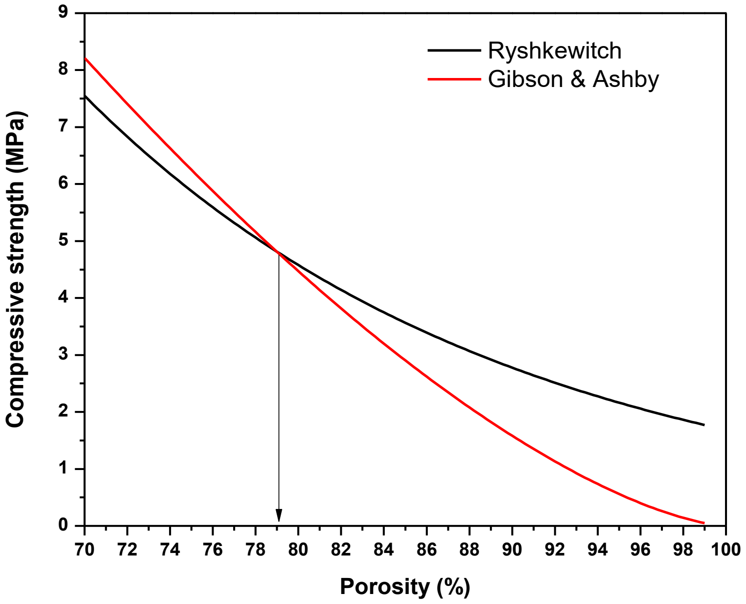

Figure 4.3 - Values of compressive strength versus porosity determined by the Ryshkewitch (equation 4.1) and Gibson & Ashby (equation 4.4) models.

Table 4.2 shows the compressive strengths calculated for a porosity range from 70% to 95%, using the Ryshkewitch (equation 4.1) and Gibson & Ashby (equation 4.4) models. Values obtained by the Ryshkewitch equation varied from 7.5 MPa (P = 70%) to 2.2 MPa (P = 95%); and for the Gibson & Ashby model, the compressive strength varied from 8.2 MPa (P = 70%) to 0.6 MPa (P = 95%). Both models proved that it is not possible to produce scaffolds with compressive strengths similar to those ones of cortical bone using typical Bioglasses. The σ_c values found using both models are agreed with the experimental data obtained for scaffolds in different studies (FU et al., 2013).

Table 4.2 - Compressive strength values determined using the Ryshkewitch (equation 4.1) and Gibson & Ashby (equation 4.4) models for a range of porosity values from 70% to 95%.

Total Porosity (%)	**σ_c (MPa) Ryshkewitch [σ_0 = 250 MPa, n = 5]**	**σ_c (MPa) Gibson & Ashby [σ_0 = 250 MPa]**
70	7.5	8.2
75	5.9	6.3
80	4.6	4.5
85	3.6	2.9
90	2.8	1.6
95	2.2	0.6

Using the Ryshkewitch and Gibson & Ashby models, it is possible to calculate the necessary mechanical strength of dense material (σ_0) to produce a scaffold with compressive strength values similar to those of cortical bone. To do these calculations was used σ_c = 100 MPa, which represents the lowest value of compressive strength for cortical bone (100-150 MPa). For equation 4.1, n used was 5.

σ_0-porosity graphs obtained by both models exhibited similar behaviors when the porosity was lower than 79% (Figure 4.4a). Nevertheless, for higher porosities, the Gibson & Ashby model foresees a remarkable increase of σ_0 (Figure 4.4b), whereas, this increase is small for the Ryshkewitch model.

(a)

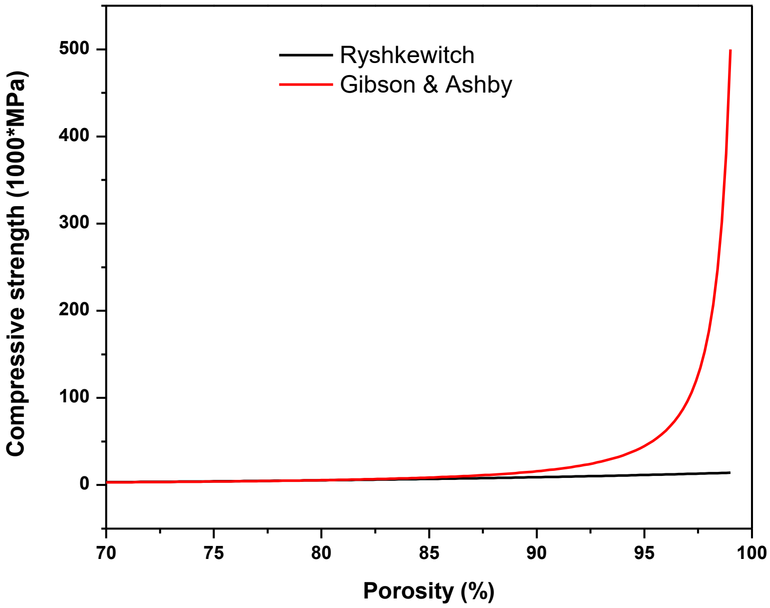

(b)

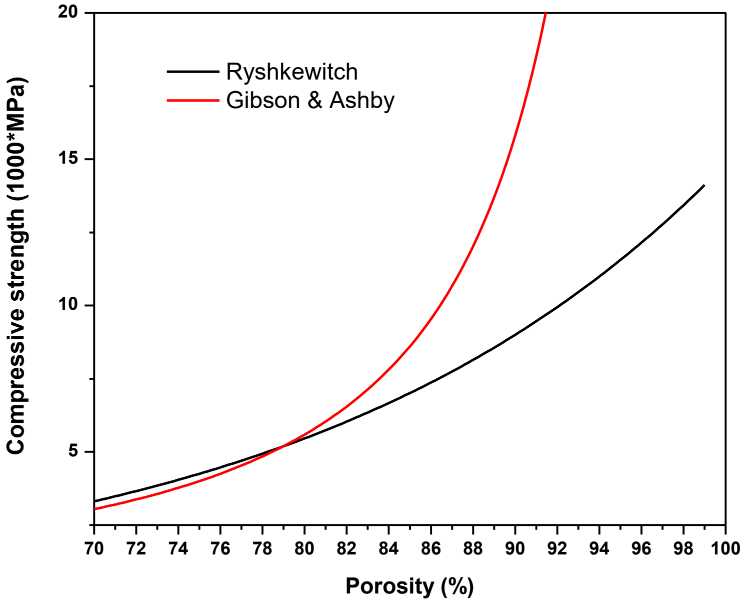

Figure 4.4 - Influence of porosity on the compressive strength of dense material (σ_0), evaluated by the Ryshkewitch (equation 4.1) and Gibson & Ashby (equation 4.4) models.

Table 4.3 shows the σ_0 values for a range of porosity values from 70% to 95%, calculated by the Ryshkewitch (equation 4.1) and Gibson & Ashby (equation 4.4) models. It was observed that the σ_0 values calculated using equation 4.1 and 4.4 varied from 3 GPa (P = 70%) to 12 GPa (P = 95%) and from 3 GPa (P = 70%) to 45 GPa (P = 95%), respectively. Thus, based on these models, it is necessary to use a material with σ_0 = 3 GPa to obtain a scaffold with a total porosity of 70% and a compressive strength of 100 MPa. The most resistant bioactive material known is the glass-ceramic A/W Cerabone®, whose σ_0 is around 1 GPa. Therefore, only a material as resistant as high alumina (σ_0 ~ 4.5 GPa) could give origin to a scaffold with these properties (P = 70% and σ_c = 100 MPa). For a porosity of 90%, which is considered optimal for some researchers, the mechanical strength of raw material should be larger than that of high alumina. Hence, it is crucial that the optimal porosity for a scaffold be established with higher accuracy.

Table 4.3 - Compressive strengths of dense material (σ_0) for a range of porosity values from 70% to 90%, evaluated by the Ryshkewitch (equation 4.1) and Gibson & Ashby (equation 4.4) models.

Total Porosity (%)	**σ_0 (GPa) Ryshkewitch [σ_c = 100 MPa, n = 5]**	**σ_0 (GPa) Gibson & Ashby [σ_c = 100 MPa]**
70	3.3	3.0
75	4.3	4.0
80	5.3	5.6
85	7.0	8.6
90	9.0	15.8
95	11.6	44.7

4.2 Assays for scaffolds prepared with 860SP-PU Foam

Initially, as a proof of concept, it was used a sponge of 35 ppi already available, i.e., with cell size in the range from 525 to 1530 µm. Although this range is above desired, we wanted to answer the following question: "Does Biosilicate scaffold infiltration with F18 bioactive glass significantly contribute to increase the mechanical strength?"

4.2.1 Polyurethane sponge characterization

Thermogravimetric analysis of the PU foam was performed to determine the best temperature to remove the sacrificial polymer template (Figure 4.5).

The peak of the first derivative indicates the maximum weight loss rate. For the PU foam the inflection point or the first derivative peak temperature is ~ 330 °C, which is the optimal temperature to remove quickly the foam by thermolysis.

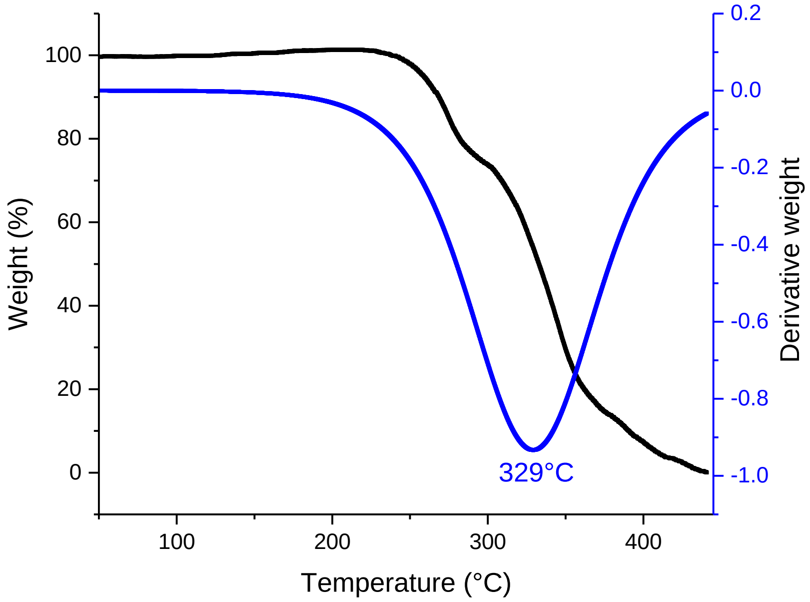

Figure 4.5 - Weight loss curve for the 860SP-PU foam and its first derivative.

4.2.2 Scaffold preparation

Initially, the 860SP-PU foams (Figure 4.6) were coated with 25.BS slurry (25% BioS), but in most cases, sintered structures deformed (Figure 4.7b) as a result of the differential retraction, losing their square prism form (Figure 4.7a). In addition, all of these structures crumbled easily because of their low mechanical properties, making difficult their handling.

Figure 4.6 - The 860-PU foam cut in a square prism shape, with 15 x 15 mm^2 square base and 30 mm length to synthesize F18-860SP.BioS scaffolds.

Under these circumstances, the 860SP-PU foams were coated with slurry 30.BS (30% BioS, APS ~ 5 µm) and sintered at 950 ˚C for 3 hours at a heating rate of 2.5 °C/min. This slurry with higher concentration of Biosilicate permitted synthesizing sintered structures with a square prism shape similar to that of the PU foams (Figure 4.7a), although with smaller size. Moreover, these scaffolds displayed structures slightly more resistant, allowing a better handling of the scaffold even though the structure can collapse easily. After this step, scaffolds were recoated (under vacuum) with 25.BS slurry (25% BioS, APS ~ 5 µm) and sintered at 950 ˚C for 3 hours at a heating rate of 2.5 °C/min. A less concentrated Biosilicate slurry was used to avoid closed pores in the structures, but nevertheless a few pores was clogged. This infiltration permitted increasing the scaffold (860SP.BioS) resistance, being more easily manipulated.

Subsequently, the 860SP.BioS scaffolds were infiltrated (under vacuum) with 20.F18 slurry (20% F18, APS ~ 5 µm) and sintered at 800 ˚C for 3 hours at a heating rate of 5 °C/min. This infiltration process was done four times, using the same condition. On balance, after the 860SP.BioS scaffolds were recoated several times with F18 glass, F18-860SP.BioS scaffolds showed a considerably increase of mechanical strength, conserving their highly porous interconnected structures.

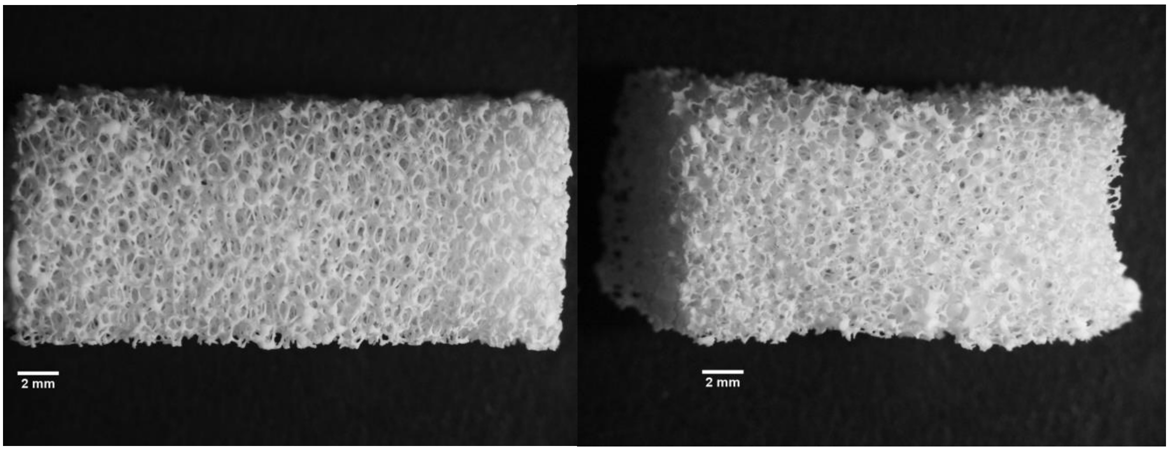

(a) (b)

Figure 4.7 - Photographs showing Biosilicate scaffolds synthesized with 860SP-PU foam coated (a) with 30.BS slurry and (b) with 25.BS slurry.

4.2.3 Scaffold characterization

4.2.3.1 SEM

SEM analyses were carried out for 860SP.BioS scaffolds and F18-860SP.BioS scaffolds. A comparison of the typical microstructure of the scaffold before and after coating with F18 glass is presented in the Figure 4.8a and 4.8b. It can be observed that the structures produced by foam replica technique present highly interconnected and open pores, i.e., a cellular structure.

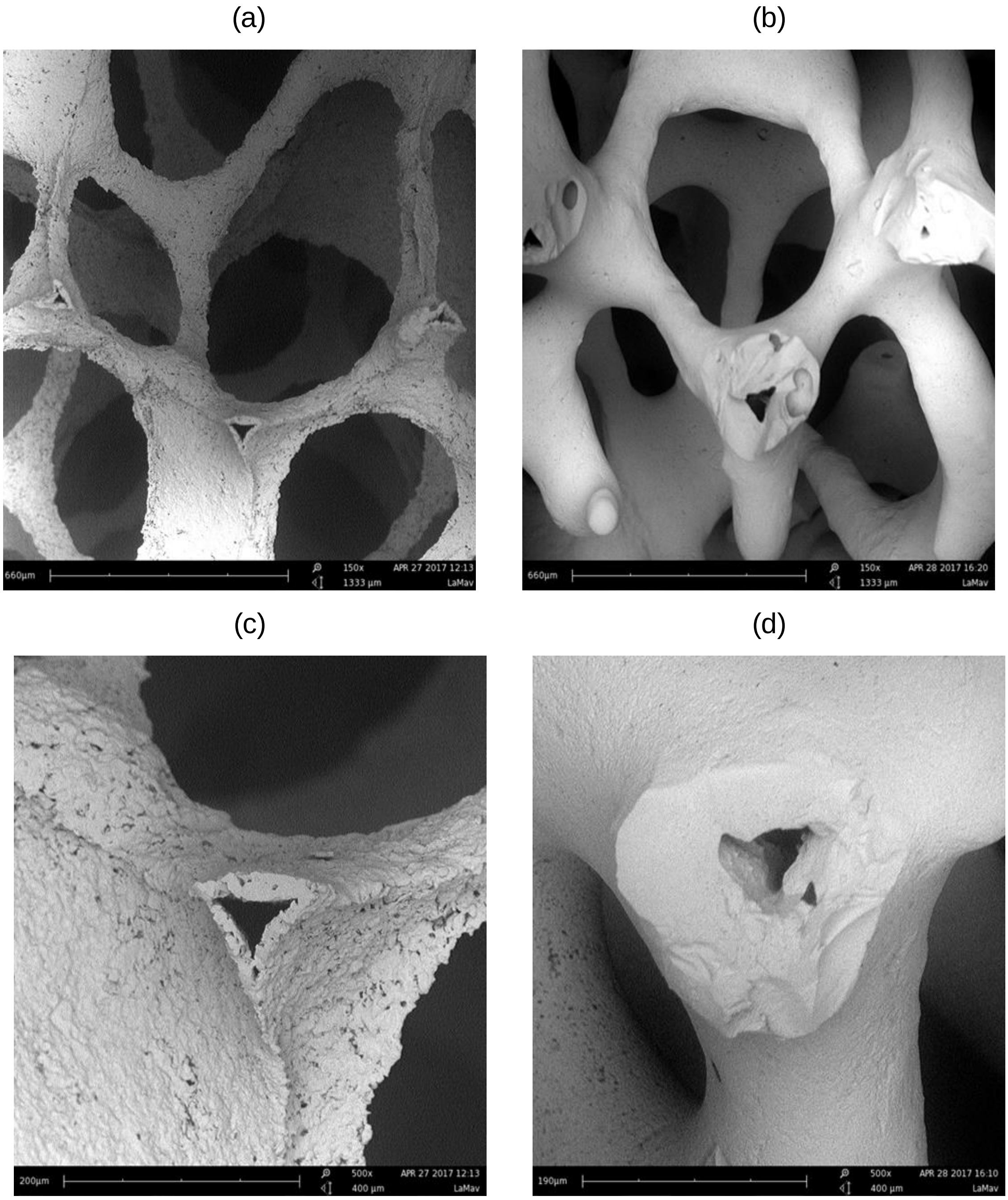
(a)
(b)
660µm
150x
APR 27 2017 12:13
1333 µm
LaMav
660µm
150x
APR 28 2017 16:20
1333 µm
LaMav
(c)
(d)
200µm
500x
APR 27 2017 12:13
400 µm
LaMav
190µm
500x
APR 28 2017 16:10
400 µm
LaMav

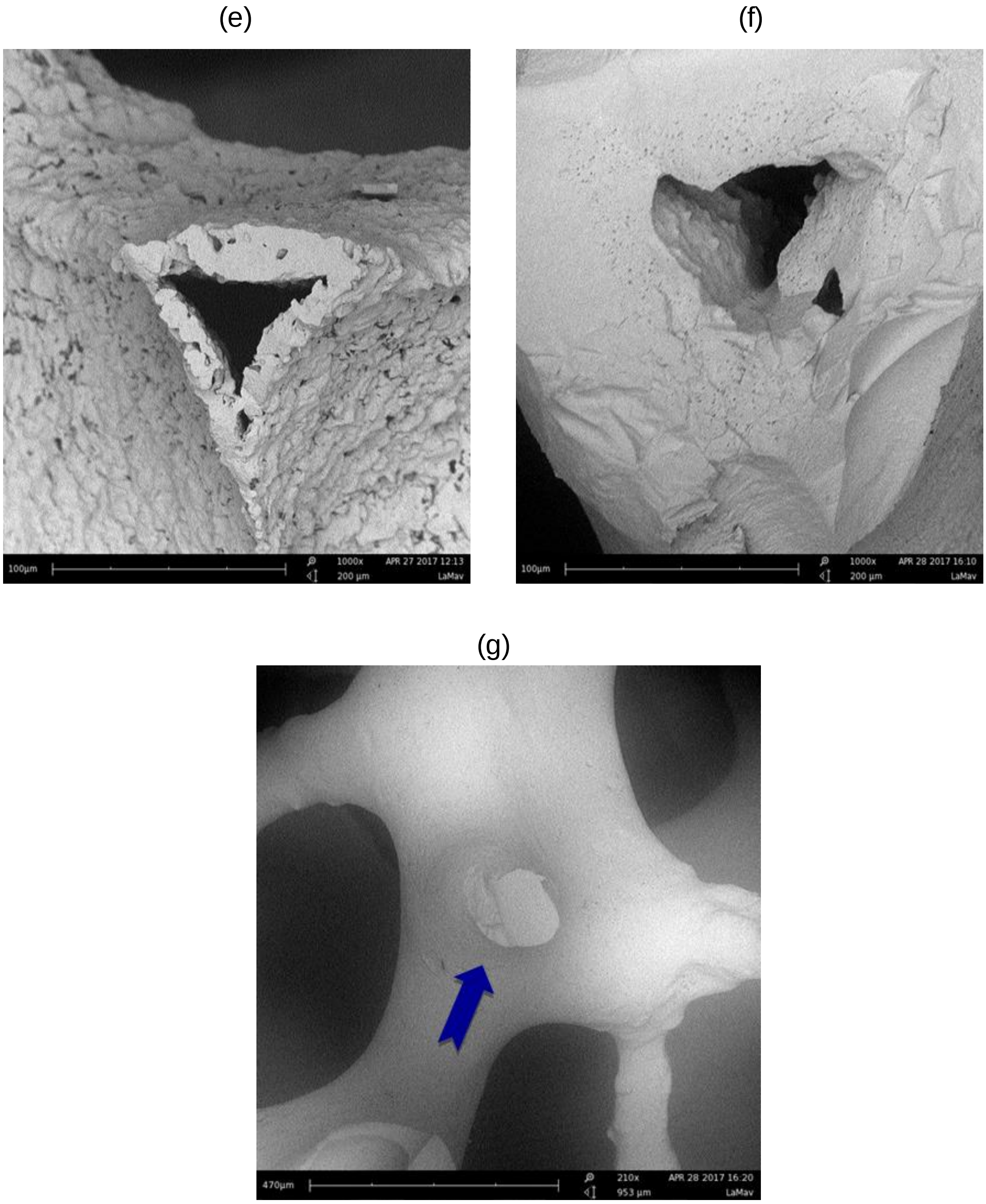

Figure 4.8 - SEM micrographs showing the 860SP.BioS scaffolds with highly interconnected and open pores (a) before and (b) after coating with F18 glass (F18-860SP.BioS scaffolds) fabricated by the foam replica method. SEM micrographs showing the microcracks and micropores in the 860SP.BioS-struts (c) before and (d) after coating with F18 glass amplified 500 times. SEM micrographs showing microcracks and micropores in the 860SP.BioS-struts (e) before and (f) after coating with F18 glass amplified 1000 times. (g) SEM micrograph showing one hollow strut, which was infiltrated and completely closed for F18 glass (blue arrow).

The surface of the “struts” in the 860SP.BioS scaffold presents both microcracks and micropores (Figure 4.8c). These features weaken the scaffold structure, which negatively affects its compressive strength, as will be shown in the item 4.2.3.3.

After dipping the 860SP.BioS scaffolds in F18 slurry for four times (under vacuum), it was expected that bioglass not only coated structure surface but also infiltrated into the hollow structure of the scaffold through the remaining porosity or microcracks, as has been observed in polymer-coated Bioglass® 45S5 scaffolds (YUNOS; BRETCANU; BOCCACCINI, 2008). The typical surface morphology of a strut of F18-860SP.BioS scaffold is displayed in the Figure 4.8d. Three features can be noted:

- F18 glass was able to coat the scaffold surfaces homogeneously, increasing the thickness of the struts being observed only few closed pores due to the incomplete removal of F18 slurry (Figure 4.8e, 4.8f, 4.9b).
- The strut surface is smooth; the majority of micropores and other defects were covered by a F18 layer.
- F18 glass partially penetrated in the hollow structure, and solid struts were observed (blue arrow - Figure 4.8g).

These features contributed to a higher compressive strength, as will be showed in the item 4.2.3.3. The hollow structure of the scaffold was not completely filled with F18 glass, as expected. This probably occurred because the vacuum employed was not high enough to compel the infiltration of the F18 slurry homogeneously through the hollow structure. Another possible explanation is that the slurry did not encountered open pores in specific regions of the scaffold structure.

4.2.3.2 Porosity

The calculated total porosity values of 860SP.BioS scaffolds, using the geometric method, before and after F18 bioactive glass coating were 96 ± 1 and 83 ± 2 %, respectively. The open pore structure of sintered scaffolds was preserved after coating with F18 glass, observing only few blocked pores by F18 (Figure 4.9b). Porosity of scaffolds decreased 13% after coating, but nevertheless, this porosity (83%) is adequate for application in tissue regeneration and the coating permitted improving the compressive strength of the structures.

Images of the scaffolds (Figures 4.9a and 4.9b) and the PU foam (Figure 4.10) were obtained using optical microscopy. We determined their average cell sizes using the ImageJ software. The average cell sizes for the PU foam, 860SP.BioS scaffolds, and F18-860SP.BioS scaffolds were 860 ± 300 μm, 830 ± 267 μm, and 770 ± 290 μm, respectively. Also, the size distributions were found in the range of 525 to 1530 μm, 420 to 1400 μm, and 395 to 1320 μm, respectively. It can be noted that for the 860SP.BioS scaffolds, the pore size reduced about 4% compared with pore size of the 860SP-PU foam and the pore size of the 860SP.BioS scaffolds suffered a reduction about 7% after coating with F18 bioglass. However, different studies (DESIMONE et al., 2013; GRANITO et al., 2009, 2011; RENNO et al., 2013) in bone repair have found that the appropriate pore size for this kind of application lies in the range from 300 to 600 μm, stimulating bone and blood vessels ingrowth. Hence, it was necessary to change the sacrificial template (PU sponge) for other that presented one adequate size distribution since these preliminary biomaterials showed an average pore size (770 μm) above the upper limit. For a matter of comparison, the values of porosity, average cell size, and compressive strength are presented in the table 4.4.

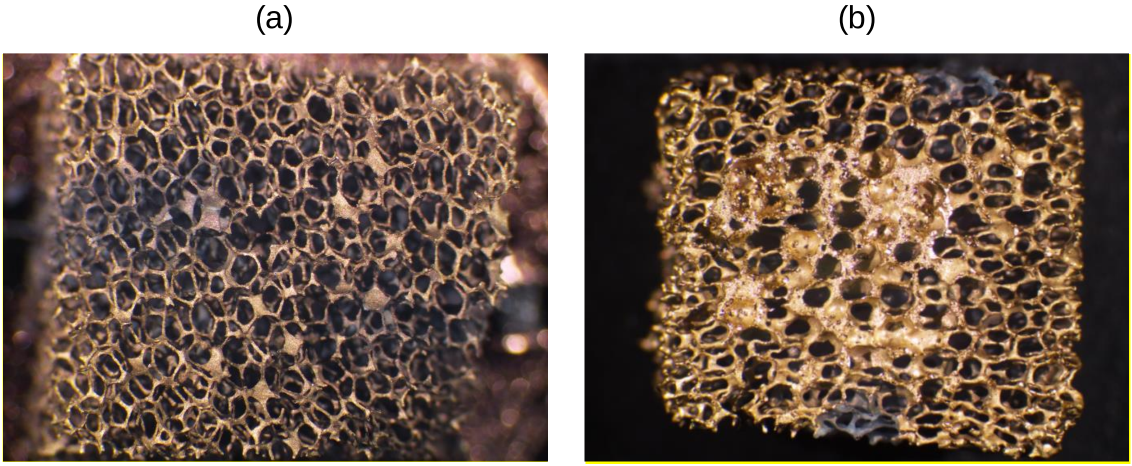

Figure 4.9 - Photographs showing (a) 860SP.BioS scaffolds and (b) F18-860SP.BioS scaffolds coated with sputtered gold.

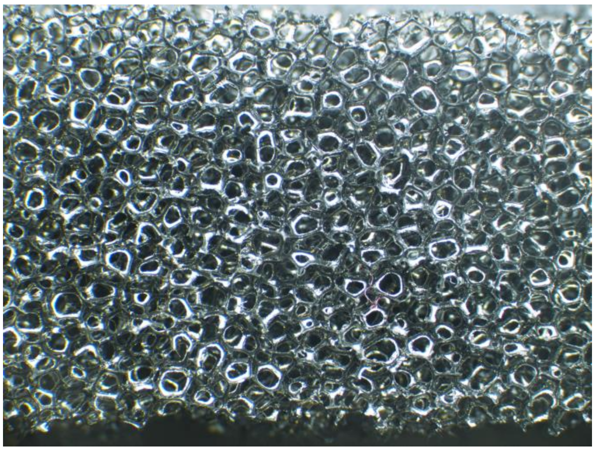

Figure 4.10 - Photograph taken with optical microscope showing a highly interconnected porous structure of 860SP-PU foam.

Table 4.4 - Total porosity, average cell size, and compressive strength for the Biosilicate scaffolds before and after coating with F18 glass.

Scaffold type	Total porosity (%)	Average cell size (μm)	Compressive strength (MPa)
860SP.BioS	96 ± 1	830 ± 267	0.02 ± 0.005
F18-860SP.BioS	83 ± 2	770 ± 290	1.0 ± 0.4

4.2.3.3 Compressive strength

To do these tests, aluminum discs were joined parallel to scaffold faces using an epoxy resin, as shown in Figure 4.11.

The mechanical tests evidenced that the compression strengths of the 860SP.BioS scaffolds are very low (Figure 4.12), showing an average compression strength of 0.020 ± 0.005 MPa. Besides a high total porosity and large cell size, one of the factors that contributed markedly to diminish the mechanical properties of the scaffolds was that obtained structures are hollow. For F18-860SP.BioS scaffold, we observed an average compression strength of 1.0 ± 0.2 MPa (Figure 4.13), leading to an increase by about 50 times of the value found for the 860SP.BioS scaffolds (Figure 4.14). This increase of the compressive strength is related to the F18 bioglass coating, which was able to penetrate the pore walls in some parts of the hollow structure permitting certain degree of filling of these defects in the scaffolds. It is necessary to point out that the scaffold showed a lower total porosity, as well as lower average cell size (Figure 4.14).

Figure 4.11 - Image showing the arrangement of the scaffolds for mechanical tests.

As is well known, the compressive strength of natural cancellous bone is in the range from 2 to 12 MPa when its relative density is about 0.1 (GONG et al., 2006; NASERI et al., 2015). Even though, the preliminary results reached in this study (~ 1 MPa) are close to the lower limit, the scaffolds could be handled without difficulty. Moreover, it expected that the mechanical properties of the scaffolds designed using this technique could be increased using one PU foam with a smaller average cell (e.g., 500 µm). This is part of the next step of this work. In addition, other slurry concentrations and different particle size distributions of F18 glass were tested. Additionally, a new device for scaffold infiltrations was used, assuring a stronger vacuum in order to find better conditions that allow a homogeneous filling of the hollow structure present in the scaffolds.

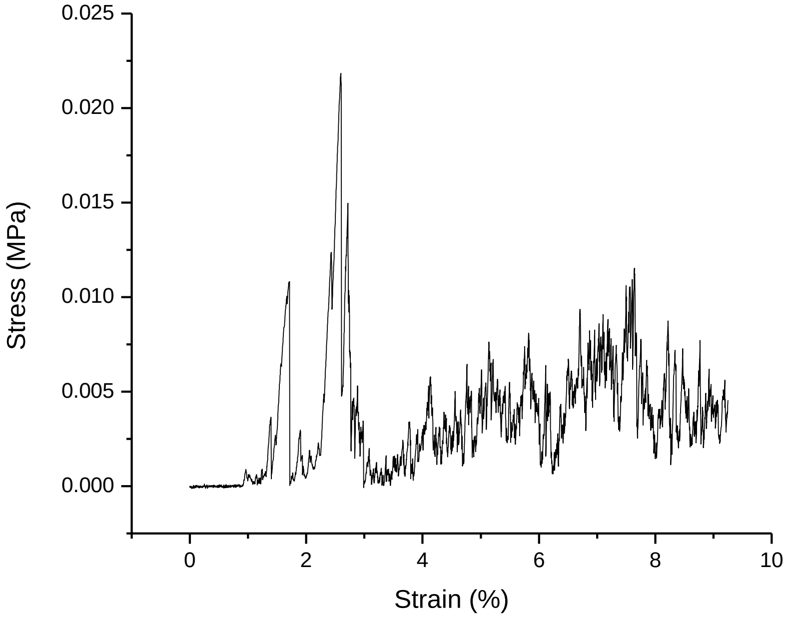

Figure 4.12 - Typical stress-strain curve for the 860SP.BioS scaffold.

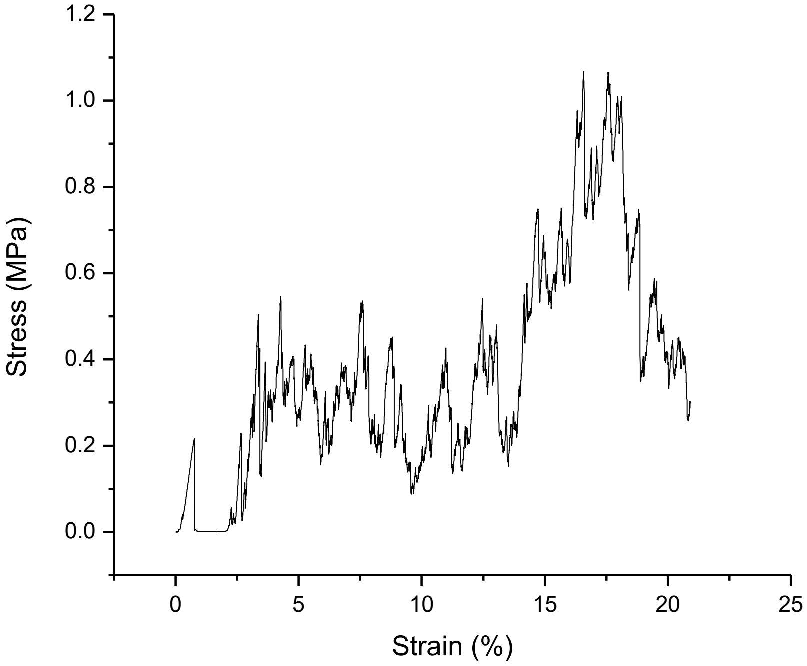

Figure 4.13 - Typical stress-strain curve for F18-860SP.BioS scaffold.

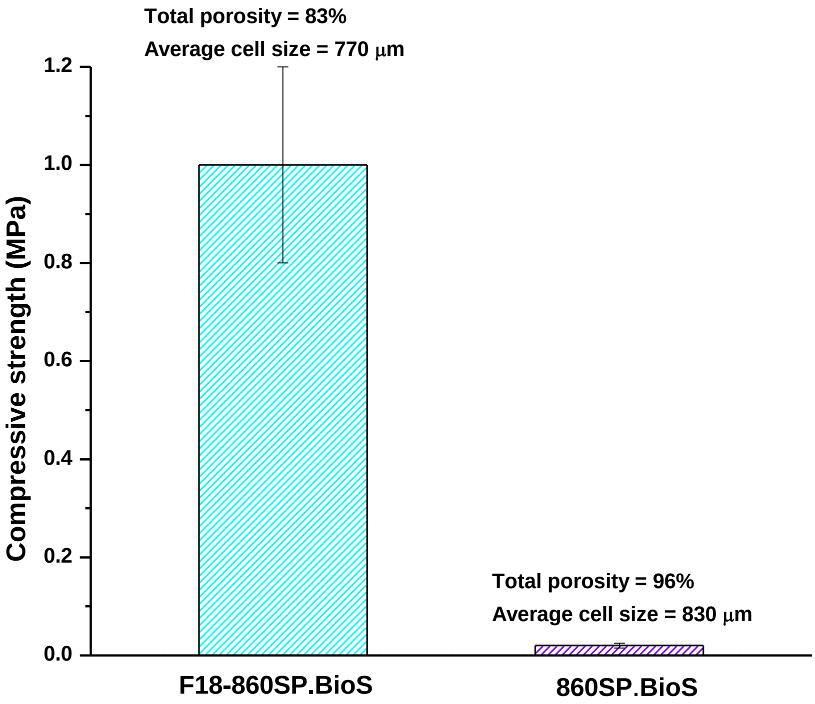

Figure 4.14 - Bar graph comparing the compressive strengths between 860SP.BioS scaffolds with and without glass coatings.

4.3 Assays for scaffolds prepared with 590-PU Foam

Since previous tests have shown that it is possible to increase the mechanical strength of Biosilicate scaffolds using the F18 bioglass infiltration strategy, a new type of PU foam was tested. In this case, considering the firing shrinkage, the 590-PU foam probably would lead to an average cell size within the ideal range. In this second part, three new questions arose:

- Will the cells remain open after infiltration with the F18 bioglass suspension?
- Is it possible to obtain scaffolds with mechanical compressive strength similar to the existing commercial products?
- Does the mechanical strength obtained experimentally agree with the theoretical values?

4.3.1 Polyurethane sponge characterization

As can be observed in Table 4.5 and Figure 4.15, the pure 590-PU foam decomposition proceeded in three steps and the main decomposition occurred between room temperature and 460 °C losing around 87% of mass. Between room temperature and 330 °C, weight loss was around 32% and the maximum decomposition rate was at 290 °C. Between 330 °C and 460 °C, weight loss was more significant (55%) and the maximum decomposition rate was at 400 °C. For these reasons, during the heat treatment, the 590C-PU foam was kept for one hour at 280 °C and for another hour at 380 °C to permit the foam to reach the maximum decomposition rate slowly and to avoid sample deformation. The third step between 460 °C and 950 °C caused a weight loss of 6% and represents combustion of the sponge residues (SIFONTES et al., 2010). For PVB, the main decomposition occurred between room temperature and 590 °C, where binder lost around 99% of mass (Figure 4.16). Between room temperature and 480 °C, weight loss was around 86% and the maximum decomposition rate was at 360 °C. Between 480 °C and 590 °C, weight loss was 13% and the maximum decomposition rate was at 520 °C.

When the foam is coated with the Biosilicate slurry, weight loss at 290 °C was 14% and the maximum decomposition rate was at 270 °C, this corresponds to the first step of foam decomposition (Figure 4.17). Between 290 °C and 400 °C, weight loss was 19% and the maximum decomposition rate was at 340 °C. In this step, PVB and the PU foam lost more mass; this was expected because around 400 °C foam lost around 55% of weight and at 360 °C PVB lost around 86% of weight. As can be seen in Figure 4.18, thermogravimetric weight loss plots of PVB, 590-PU foam, and slurry-coated 590-PU foam are similar, although, the first derivative peak temperature of slurry-coated 590-PU foam moved to lower temperature and it lost only 41% of mass at 950 °C because Biosilicate did not decompose (JIANG et al., 2014).

Table 4.5 - Weight loss for PVB, 590-PU foam, and 590-PU foam coated with BioS slurry.

Sample	Temperature range (ºC)	Weight loss (%)
590-PU foam	25 → 330	32
	330 → 460	55
	460 → 950	6
PVB	25 → 480	86
	480 → 590	13
	590 → 950	0.3
PU foam with slurry	25 → 290	14
	290 → 400	19
	400 → 950	8

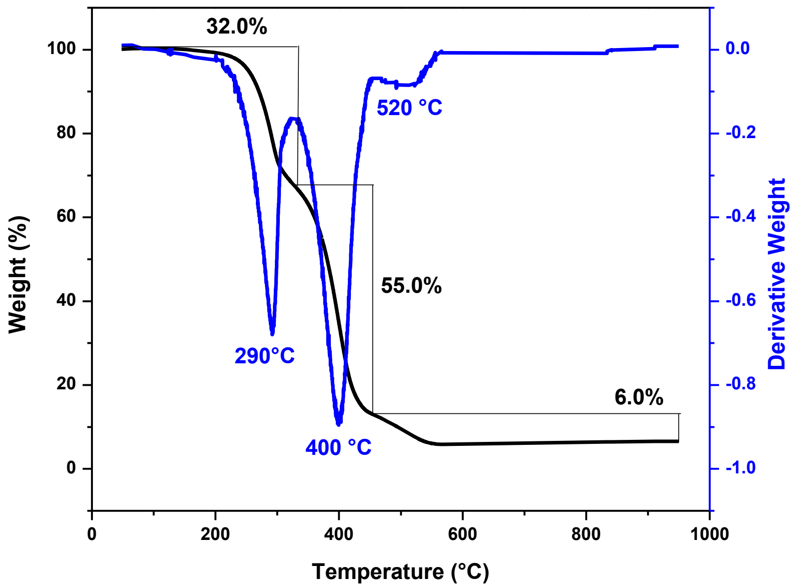

Figure 4.15 - Weight loss curve for the 590-PU foam and its first derivative.

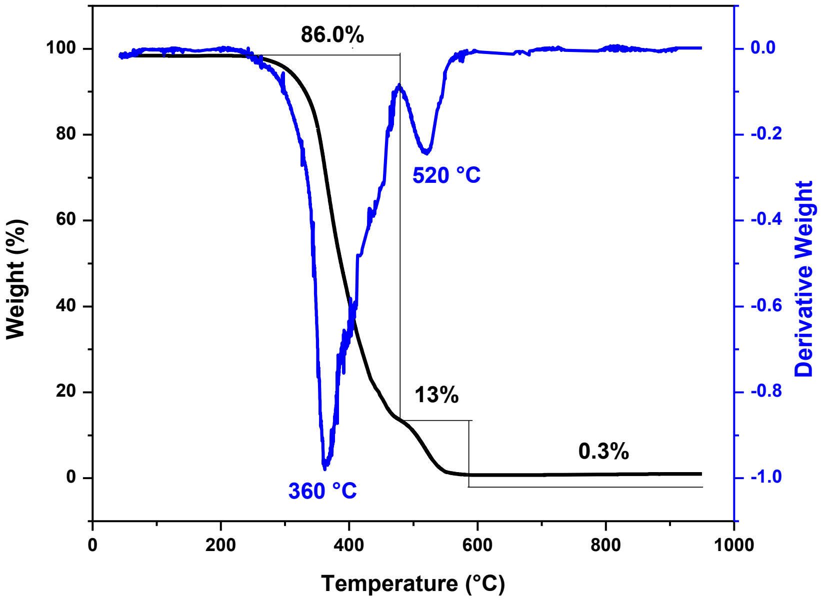

Figure 4.16 - Weight loss curve for PVB and its first derivative.

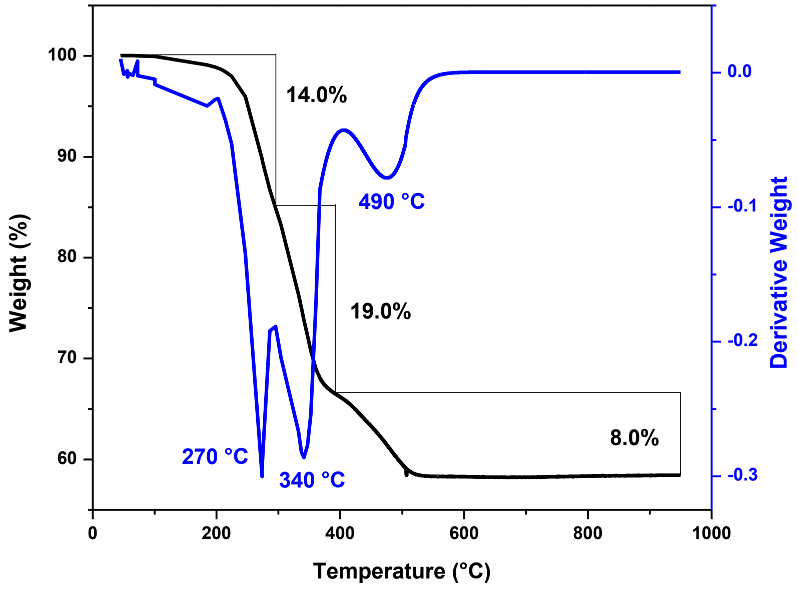

Figure 4.17 - Weight loss curve for 590-PU foam coated with BioS slurry and its first derivative.

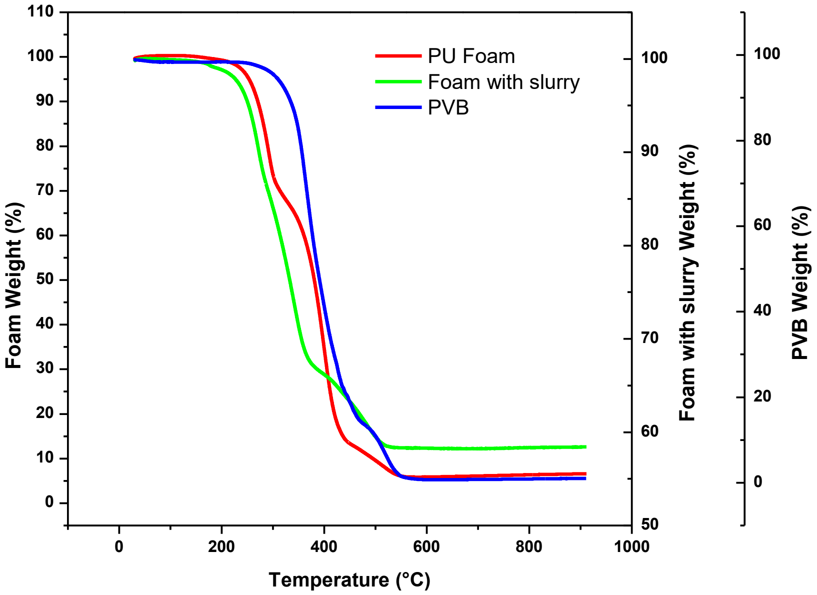

Figure 4.18 - Weight loss curves for PVB, 590-PU foam, and 590-PU foam coated with Biosilicate slurry.

4.3.2 Maximizing the infiltration of slurry into hollow structure

To maximize the infiltration of slurry into the hollow structure, always present in the scaffolds, two actions were taken:

- To use a coarse Biosilicate powder in the first dipping procedure to increase the porosity of the struts, facilitating the slurry penetration in the subsequent step.
- To use slurries containing very fine powders in the subsequent dipping procedures, so that the slurry can penetrate into the struts.

4.3.3 Preparation of the F18-590RP.BioS and F18-590C.BioS scaffolds

The samples prepared in this section were used to do the *in vitro* tests.

To synthesize 590RP.BioS scaffolds was used 30.BS slurry to coat the 590RP-PU foam. The Biosilicate powder used to prepare the 30.BS slurry was milled with 30 mm agate milling balls at 500 rpm for 30 minutes. This Biosilicate powder was gently milled because larger particles allow generating a more porous surface, which would facilitate the penetration of the slurries into the hollow structure. The concentrations and reagents used to prepared 30.BS slurry are found in section 3.5. Two different conditions (10m and 30m) were used to homogenize the 30.BS slurry.

- Milling with 30 mm agate milling ball at 500 rpm for 10 minutes (10m).
- Milling with 30 mm agate milling ball at 500 rpm for 30 minutes (30m).

To prepare 590RP.BioS scaffolds using 10m homogenization, first, PVB with alcohol was milled for 30 minutes for a complete dissolution. Then, the Biosilicate powder was added and milled for 10 minutes. Later, 590RP-PU foams were dipped in 30.BS slurry. This process was done only one time because the foam deformed during the second immersion in the slurry since foam size was large. When the bodies were dried, the heat treatment 6 (HT6) was performed as described below. In item 3, 4 and 5, the sintering temperatures (**X**) used were 900 °C, 950 °C, and 975 °C.

1. Heating from 30 °C to 410 °C at 1 °C/min.
2. 410 °C for 240 minutes.
1. Heating 410 °C to **X** °C at 2.5 °C/min.
2. **X** °C for 180 minutes.

3. Cooling from **X** °C to 30 °C at 5 °C/min.

Initially, the S10m.975, S30m.975, S10m.950, and S30m.950 samples were prepared and sintered using the following conditions and using the heat treatment 6 (HT6):

- 10m homogenization and sintering temperature of 975 °C (S10m.975).
- 30m homogenization and sintering temperature of 975 °C (S30m.975).
- 10m homogenization and sintering temperature of 950 °C (S10m.950).
- 30m homogenization and sintering temperature of 950 °C (S30m.950).

In Figure 4.19 can be observed that the porosity over surfaces of the scaffolds were similar. Therefore, we decided to prepare 30.BS slurry using 30m homogenization; after this treatment, the average particle size of the 30.BS slurry was 15 µm. Moreover, the sintering temperature was reduced to 900 °C to increase the porosity of the surface. This was the conditions used to coat 590RP-PU foam and sintered the Biosilicate scaffold.

Other methodology was assayed to prepare a finer powder for the second dipping because it is desirable to use particles with smaller size, which are able to penetrate into the hollow structure. Moreover, it is necessary to reach particle size around 0.5 µm to use a deflocculant that stabilize the slurry (GOULART; DE SOUZA, 2017). The Biosilicate powder was milled with vibratory mill using zirconia balls of 5 mm, these powders were baptized relies on the used conditions. It was tested the following conditions:

- Per 1 g of Biosilicate powder (5b-24h) was used 5 g of zirconia balls and it was milled for 24 hours.
- Per 1 g of Biosilicate powder (20b-24h) was used 20 g of zirconia balls and it was milled for 24 hours.
- Per 1 g of Biosilicate powder (5b-48h) was used 5 g of zirconia balls and it was milled for 48 hours.

- Per 1 g of Biosilicate powder (20b-48h) was used 20 g of zirconia balls and it was milled for 48 hours.
- Per 1 g of Biosilicate powder (5b-72h) was used 5 g of zirconia balls and it was milled for 72 hours.

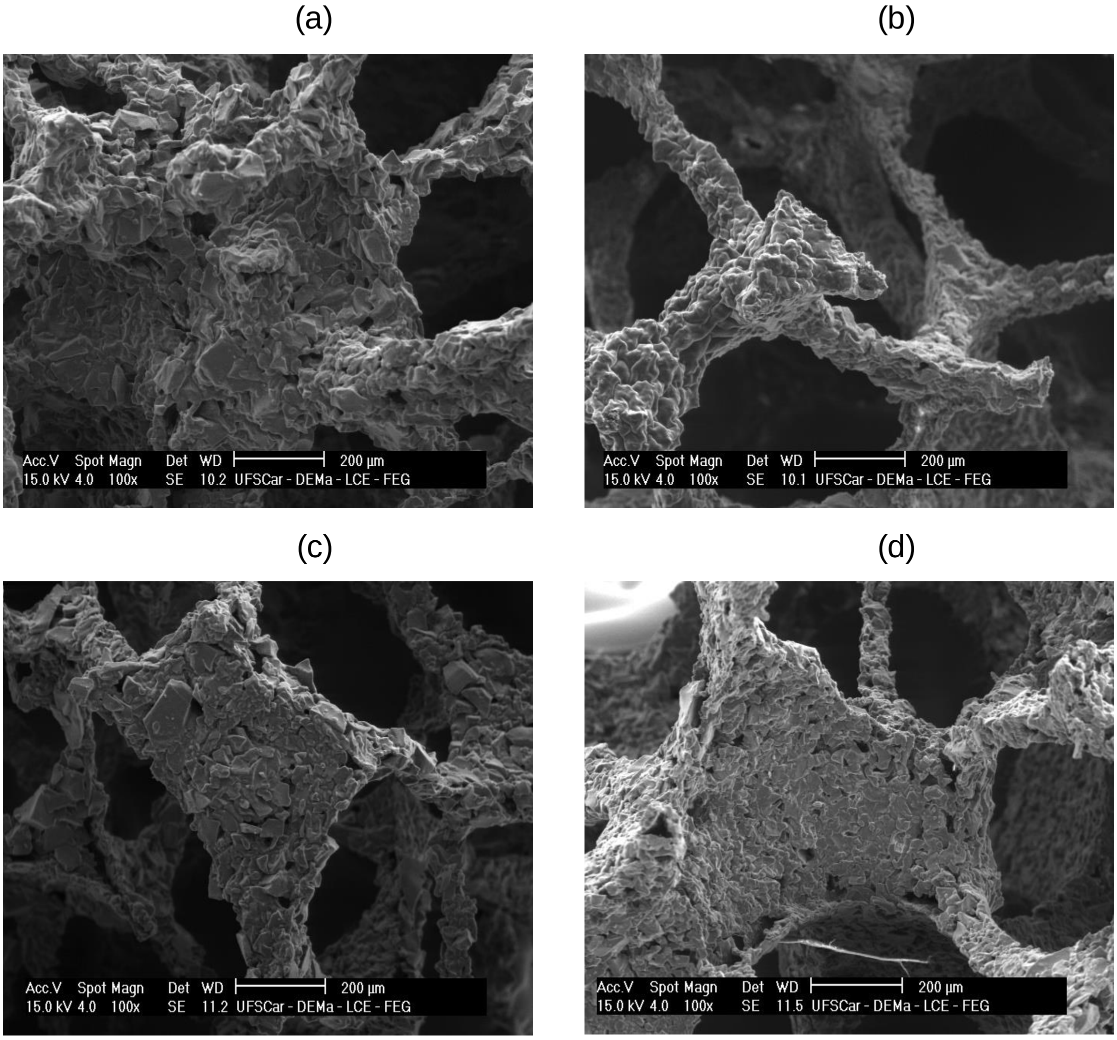

Figure 4.19 - SEM micrographs showing the surface of the scaffolds for the a) S10m.975, b) S30m.975, c) S10m.950, and d) S30m.950 samples.

The Biosilicate powder milled for 24 hours using 20 g of balls exhibited an average particle size smaller (5.1 µm) than that of powder (8.8 µm) milled using 5 g of balls for 24 hours (Figure 4.20 and 4.21). Nevertheless, when milling time was increased, the particle sizes and their distributions had no significant change compared with 20b-24h Biosilicate powder (Table 4.6, Figure 4.22, 4.23, and 4.24). It was not possible to reach the adequate particle size to control the rheological properties of the slurries. Three different deflocculants were tested: sodium polyacrylate, ammonium polyacrylate and triton X-100. However, the viscosity measurements were not reproducible, some results can be found in Annex A. Aware that the suspension is not perfectly stable, all dipping procedures were performed under magnetic stirring. Apart from the inadequate particle size, a suitable deflocculant for the system used (Biosilicate or F18 glass powder + ethanol) could not be found.

Table 4.6 - Average size of Biosilicate powder milled with vibratory mill using 5 grams of zirconia balls (5 mm) per 1 gram of Biosilicate (5:1) for 24, 48 and 72 hours; and 20 grams of zirconia balls (5 mm) per 1 gram of Biosilicate (20:1) for 24 and 48 hours.

Sample	**5b-24h**	**20b-24h**	**5b-48h**	**20b-48h**	**5b-72h**
Average size (μm)	8.8	5.1	6.7	5.1	4.9

All of these Biosilicate powders (5b-24h, 20b-24h, 5b-48h, 20b-48h, and 5b-72h) were used to prepare slurries for the second dipping. The slurries were prepared using 15% of specific powder, 3% of PVB, and 82% ethylic alcohol in 150 mL HDEP bottle (Nalgene) and milled for 2 hours in vibratory mill. The concentration was low because: the smaller particle size is, the higher viscosity is. The PU foams were impregnated with these slurries and sintered. Figure 4.25 shows that highly dense struts were obtained for all samples. Therefore, It was chosen the slurry prepared with the 20b-24h Biosilicate powder to carry out the second dipping for the Biolisicate scaffolds since this permitted saving time. The infiltrations from second dipping to sixth dipping were carried out using the vacuum system showed in Figure 3.2 (controlled vacuum).

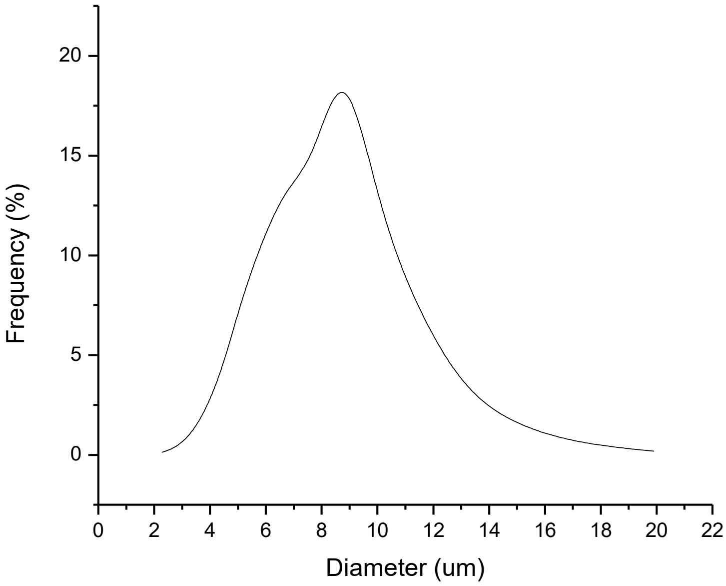

Figure 4.20 - Particle size distribution of Biosilicate powder milled for 24 hours using vibratory mill and zirconia balls; per 1 g of Biosilicate was used 5 g of zirconia balls.

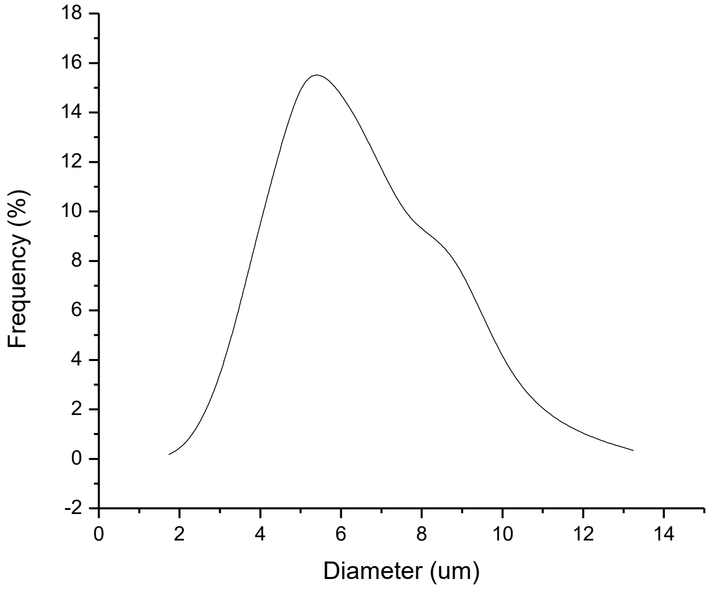

Figure 4.21 - Particle size distribution of Biosilicate powder milled for 24 hours using vibratory mill and zirconia balls; per 1 g of Biosilicate was used 20 g of zirconia balls.

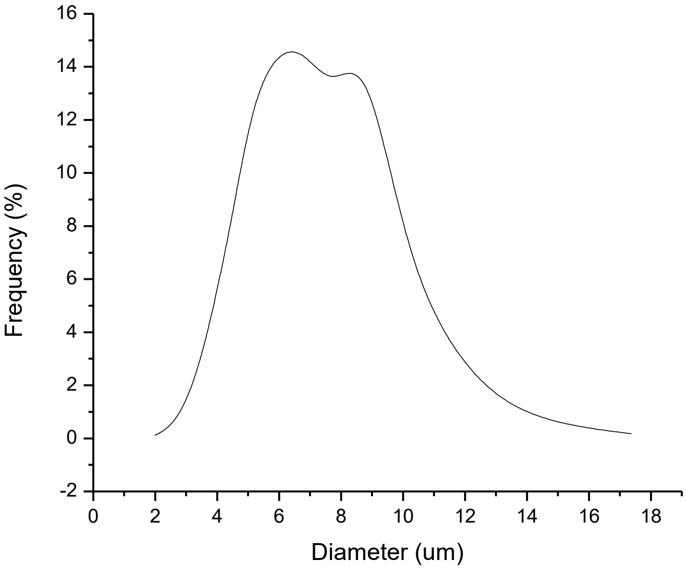

Figure 4.22 - Particle size distribution of Biosilicate powder milled for 48 hours using vibratory mill and zirconia balls; per 1 g of Biosilicate was used 5 g of zirconia balls.

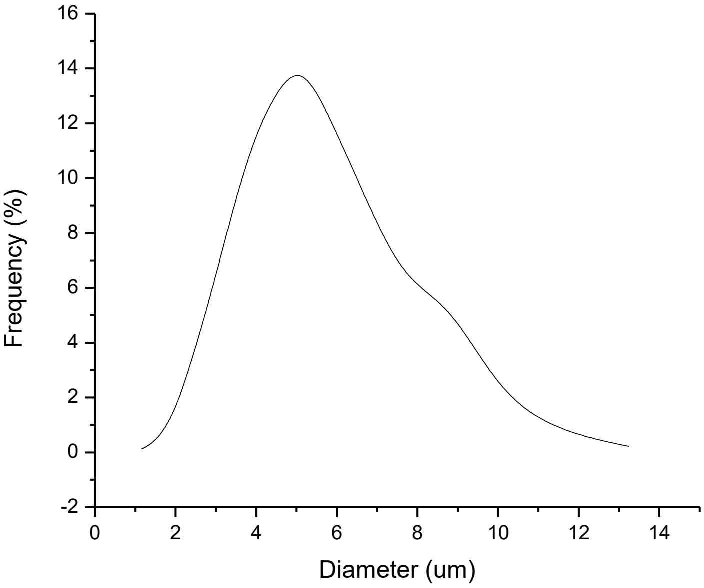

Figure 4.23 - Particle size distribution of Biosilicate powder milled for 48 hours using vibratory mill and zirconia balls; per 1 g of Biosilicate was used 20 g of zirconia balls.

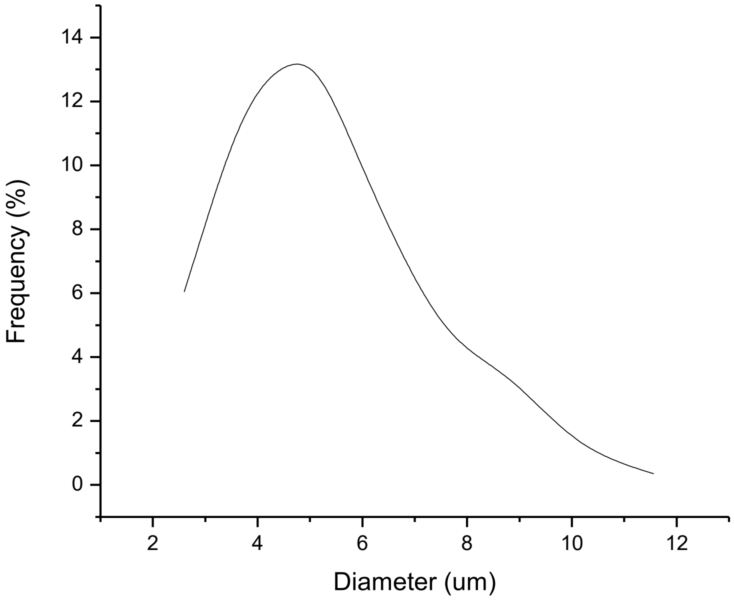

Figure 4.24 - Particle size distribution of Biosilicate powder milled for 72 hours using vibratory mill and zirconia balls; per 1 g of Biosilicate was used 5 g of zirconia balls.

Other slurries for the second dipping were prepared using Biosilicate powder milled in planetary ball mill using the following conditions and sequence:

1. Milling with 30 mm agate milling ball at 500 rpm/30min.
2. Milling with 20 mm agate milling ball at 500rpm/30min.
3. Milling with 10 mm agate milling ball at 500 rpm/30min.

With this Biosilicate powder were prepared 25.BS and 20.BS slurries. Both mixtures were homogenized in planetary mono mill with 10 mm agate milling ball at 500 rpm for 2 hours to reach an average particle size around 5 µm. Then, the Biosilicate scaffolds synthesized with 590RP-PU foam were subjected to the second dipping using 20b-24h, 25.BS, and 20.BS slurries and sintered (Figure 4.26). In these images can be noted that all scaffolds presented an inhomogeneous surface with many defects. On account of the facts that the scaffolds recoated with the 25.BS slurry showed many closed pores, and that preparation of 20b-24h Biosilicate powder is time-consuming and it does not lead to a clear advantage, 20.BS slurry was chosen to do the second dipping. The scaffold was sintered at 975 ºC and named as **590RP.BioS**.

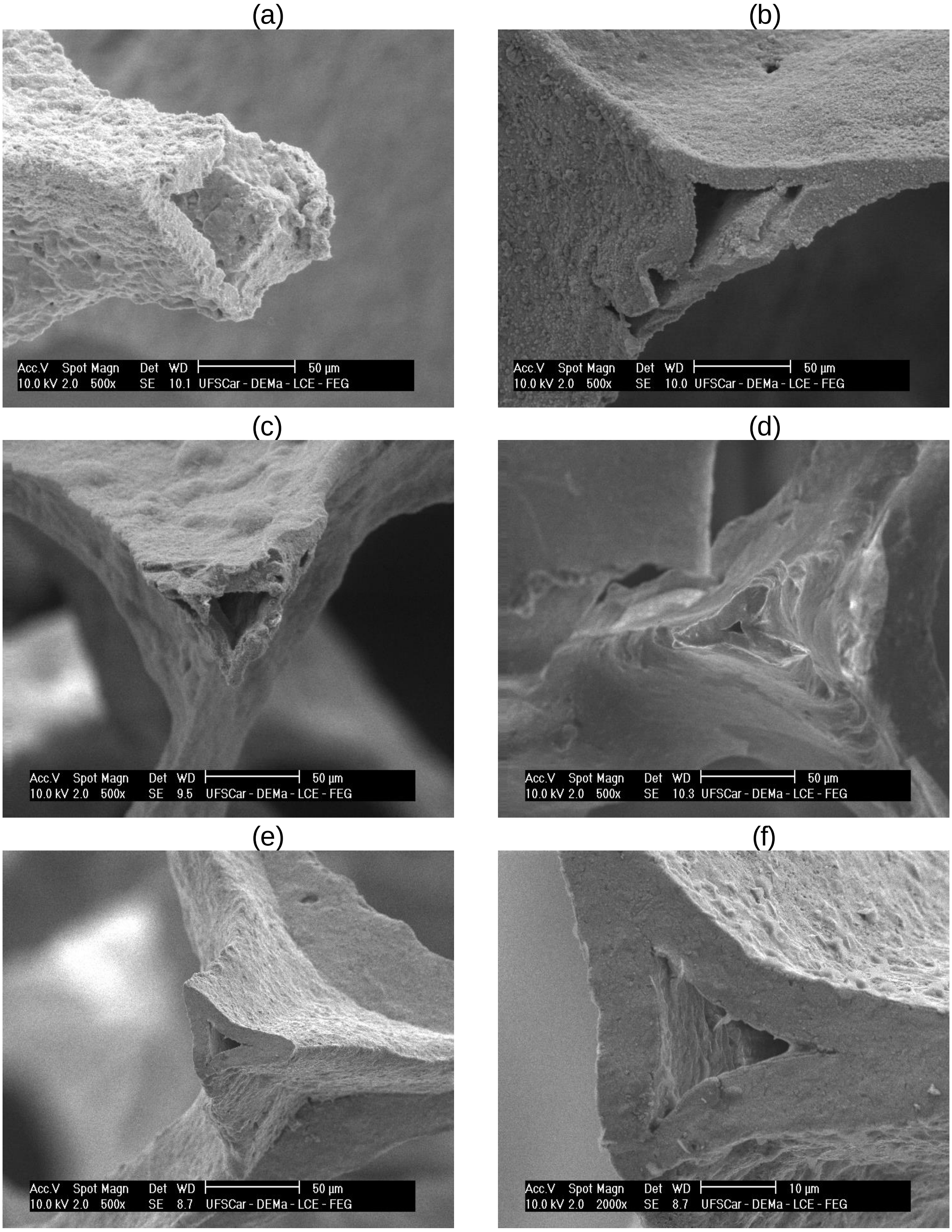

Figure 4.25 - SEM micrographs of scaffolds prepared using powder milled in vibratory mill. Following conditions were used for milling: 1 g of Biosilicate milled with a) 5 g of zirconia balls for 24 h, b) 20 g of zirconia balls for 24 h, c) 5 g of zirconia balls for 48 h, d) 20 g of zirconia balls for 48 h and e) and f) 5 g of zirconia balls for 72 h.

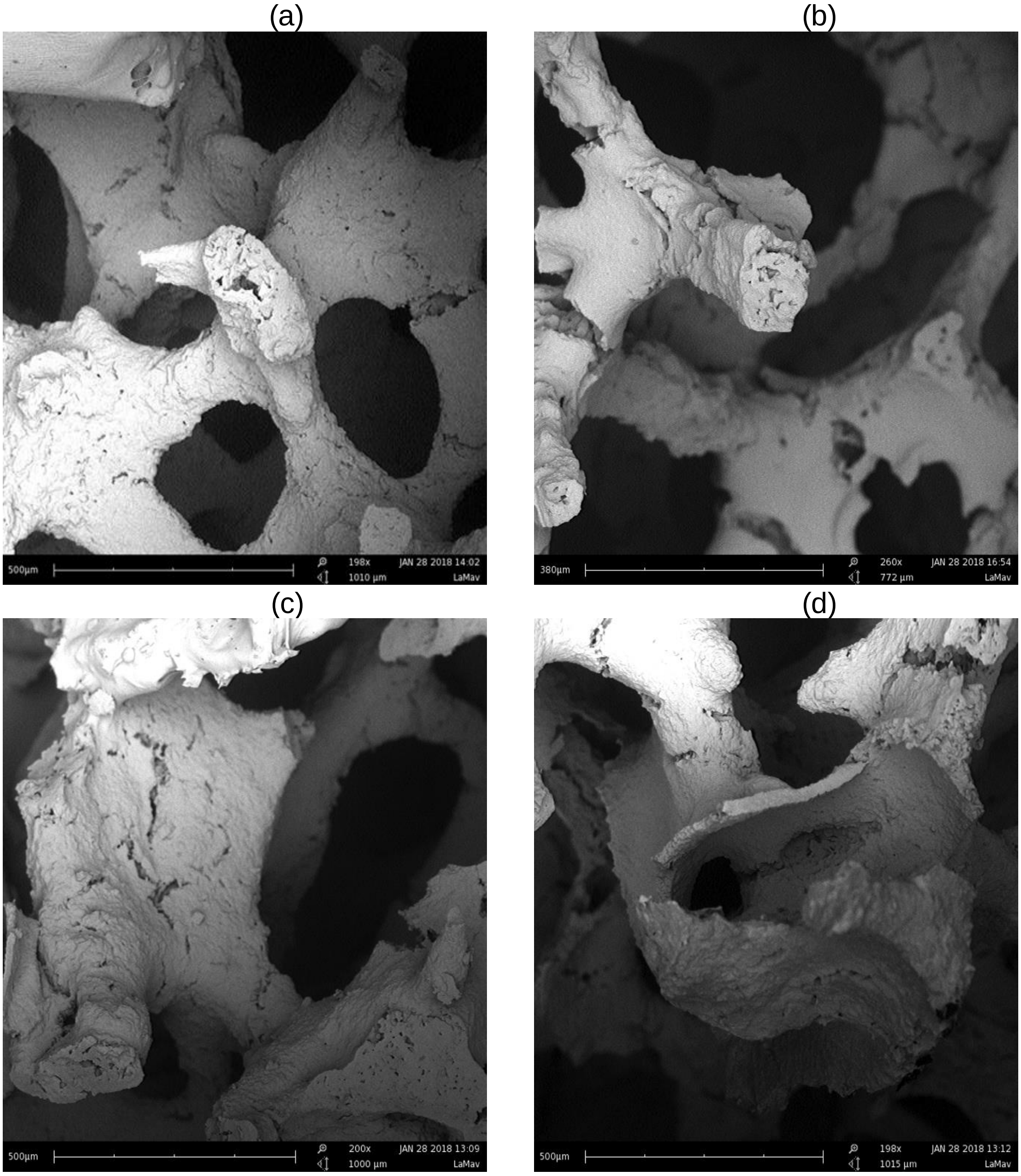

Figure 4.26 - SEM micrographs of the Biosilicate scaffolds prepared with 590-PU foam after second dipping in a) 20.BS slurry b) 25.BS slurry c) and d) 20b-24h slurry (15% BioS).

F18 bioglass was used to prepare 15.F18 slurry for the third, fourth, fifth and sixth dipping. 15.F18 slurry was homogenized (section 3.5) until reaching an average particle size around 5 µm, which is ideal to penetrate the hollow structure of the scaffold. Then, 590RP.BioS scaffolds were infiltrated with 15.F18 slurry, dried and sintered at 800 °C. This process was done four times using the same conditions to produce **F18-590RP.BioS** scaffolds.

Unfortunately, after first dipping with F18 glass, some black spots appeared in the sintered scaffolds (Figure 4.27). To identify the origin of this contamination, one chemical analysis of the scaffold, over point D (Figure 4.28), was carried out using SEM/EDS. This analysis showed that contamination was mainly composed of carbon, which represents 60% of weight (Figure 4.29). Probably, the contaminant is the binder (PVB) that was not completely burned-out during sintering. When the scaffold is produced using a small sponge, this phenomenon is not observed. Possibly, the bigger the sample is, the more difficult PVB leaves from the sample. Then, the sample was burned for some hours at 400 °C, but the contamination continued inside the material. One possible solution to fabricate scaffolds with this size is assayed other binders.

Figure 4.27 - Image of F18 glass-coated 590RP.BioS scaffold after heat treatment. PU foam size used as polymer template was 80x50x30 mm^3.

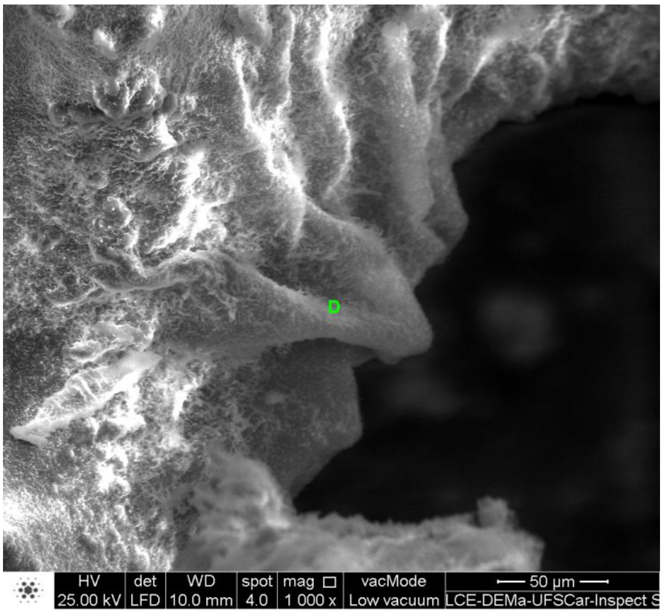

Figure 4.28 - SEM of the contamination in F18 glass-coated 590RP.BioS scaffold. D indicates the part of the sample used to do chemical analysis.

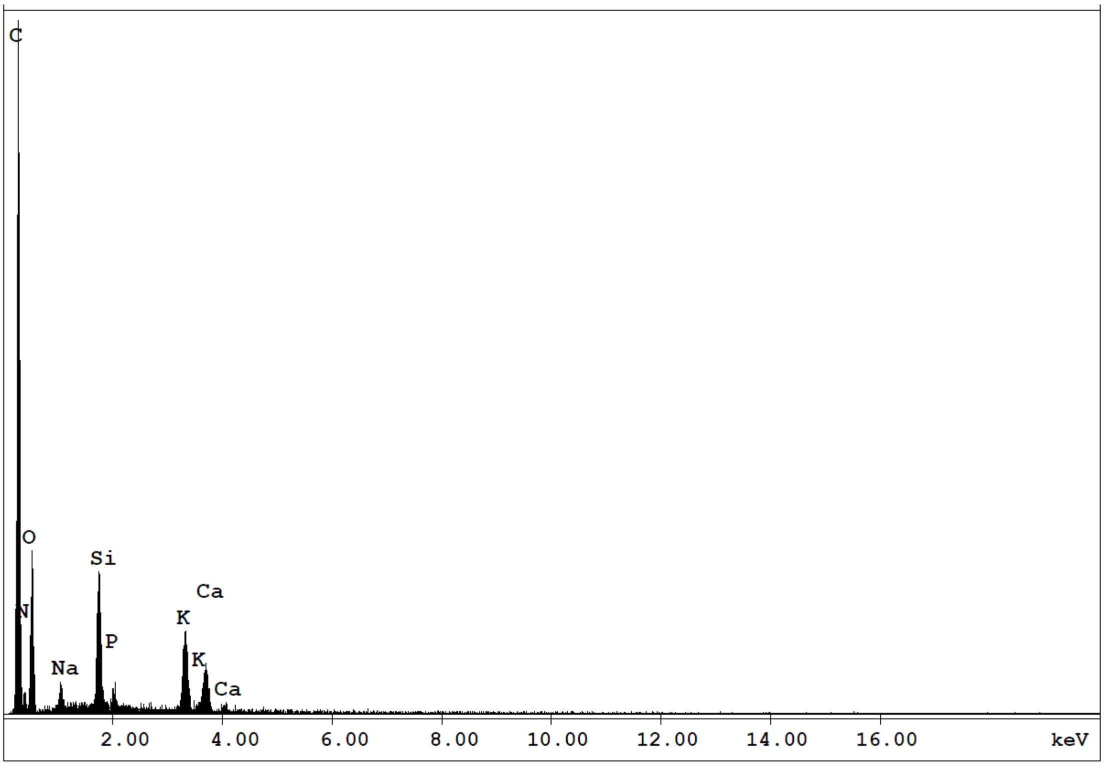

Figure 4.29 - Chemical analysis of the contamination in F18 glass-coated 590RP.BioS scaffold.

Figure 4.30 showed that after the third F18 coating, many defects over the 590RP.BioS scaffold surface were eliminated; nevertheless, the hollow struts were not completely infiltrated.

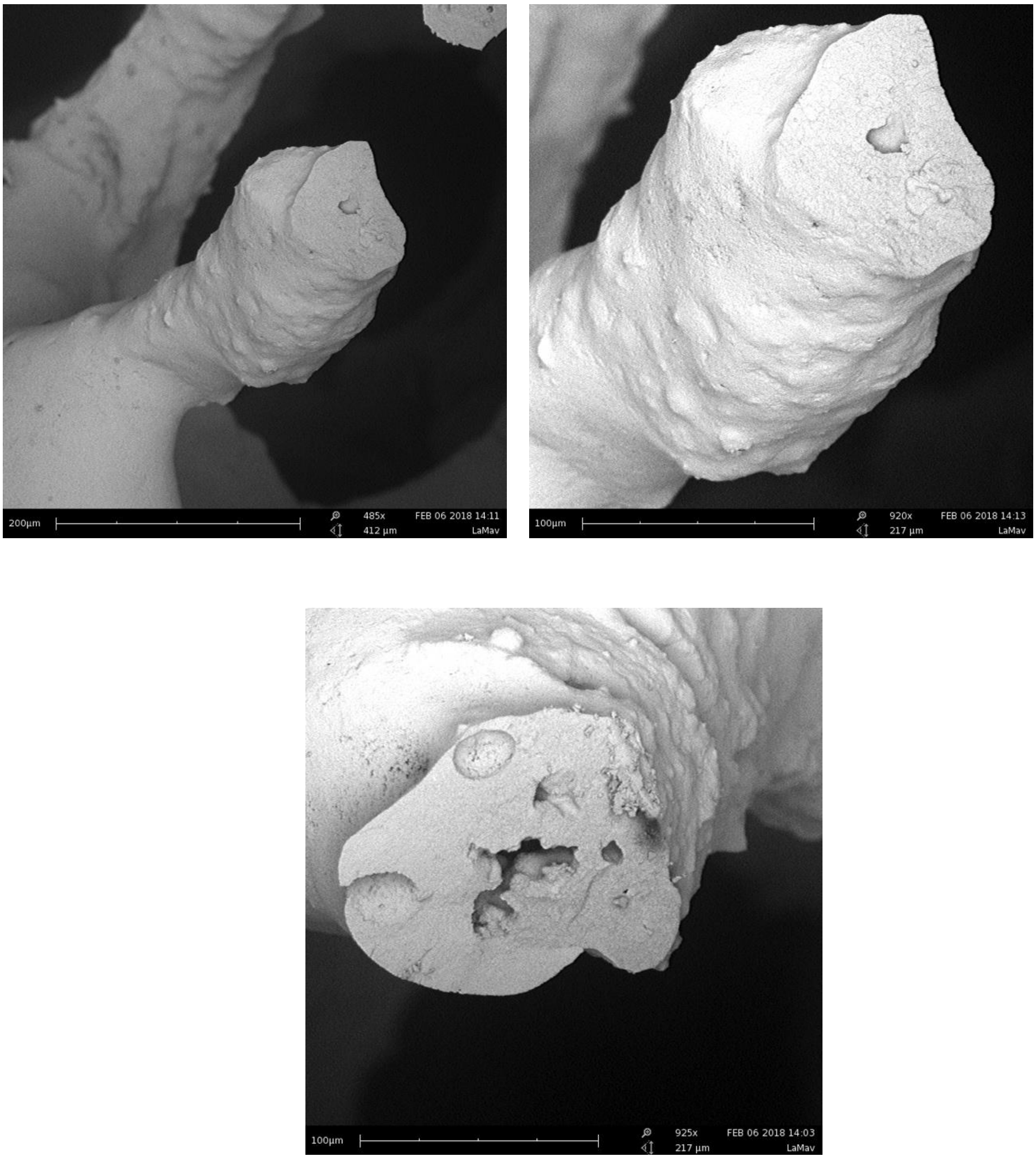

Figure 4.30 - SEM micrographs of typical strut of 590RP.BioS scaffold after third dipping with F18 glass.

The conditions used to synthesize F18-590RP.BioS scaffold were used to synthesize F18-590C.BioS scaffold. Nevertheless, since the latter was synthesized with a smaller sponge compared with 590RP-PU foam, some changes had to be done. To coat the 590C-PU foam was use the 35.BS slurry with a higher concentration (35% BioS) because the scaffolds deformed when less concentrated slurry was used. Moreover, after second dipping with Biosilicate the sintering temperature was reduced to 900 °C because of sample deformation. Indeed, this was also the sintering temperature (900 °C) used for the first coatings of the 590C.BioS and 590RP.BioS scaffolds because during foam pyrolysis the scaffold deformed. Moreover, the 590C-PU foams were burnt in different steps (section 3.6.3) based on the TGAs (section 4.3.1) because this avoided sample deformation.

4.3.4 Scaffold characterization

4.3.4.1 SEM

Microstructures of 590C.BioS and F18-590C.BioS scaffolds were evaluated by SEM. It can be seen in Figure 4.31a that 590C.BioS scaffold presented a highly interconnected porous structure. This structure has many defects (Figure 4.31e) such as microcracks and micropores over surface as well as hollow struts that are considerably reduced after diverse F18 glass coatings (Figure 4.31b and 4.31d).

As can be observed in Figure 4.31c and 4.31g, 590C.BioS scaffolds presented triangular voids with different sizes; after F18 glass coatings it was observed that F18 glass penetrated the hollow struts (Figure 4.31f and 4.31h). Unfortunately, the hollow struts of scaffolds were only partially closed after all coatings (Figure 4.31h, 4.31k and 4.31l), exhibiting smaller sizes (Figure 4.31h) in comparison with those of 590C.BioS scaffolds (Figure 4.31c). As shown in section 4.3.3, when 590-PU foam was coated with slurry prepared with Biosilicate powder (5b-72h), milled with vibratory mill, the dimensions of the hollow struts (figure 4.25f) were small too. It would be interested to recoat this Biosilicate scaffold (5b-72h) using the same conditions described in section 4.3.3 and compare with mechanical properties of F18-590C.BioS scaffolds.

(a)

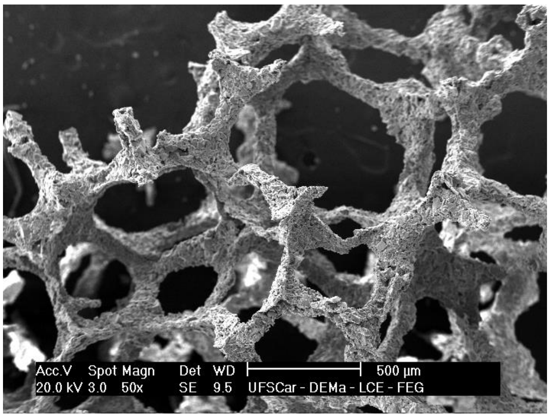
Acc.V Spot Magn Det WD 500 µm
20.0 kV 3.0 50x SE 9.5 UFSCar - DEMa - LCE - FEG

(b)

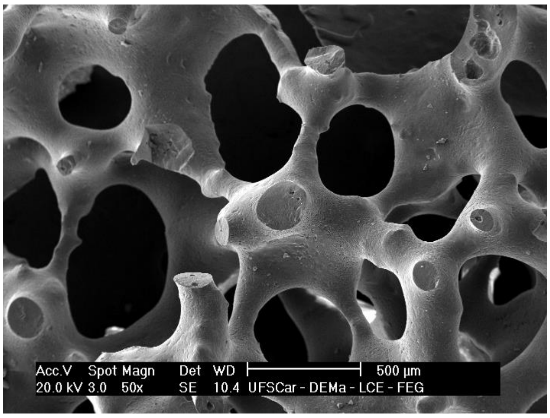
Acc.V Spot Magn Det WD 500 µm
20.0 kV 3.0 50x SE 10.4 UFSCar - DEMa - LCE - FEG

(c)

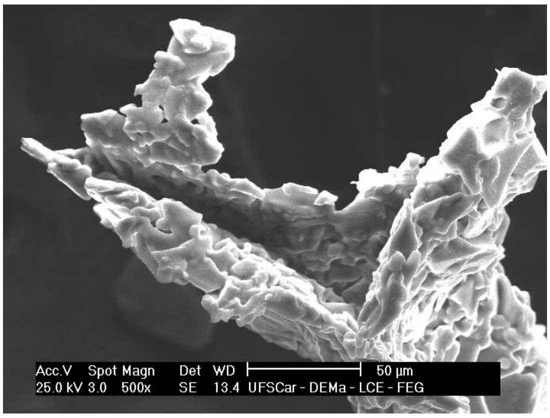
Acc.V Spot Magn Det WD 50 µm
25.0 kV 3.0 500x SE 13.4 UFSCar - DEMa - LCE - FEG

(d)

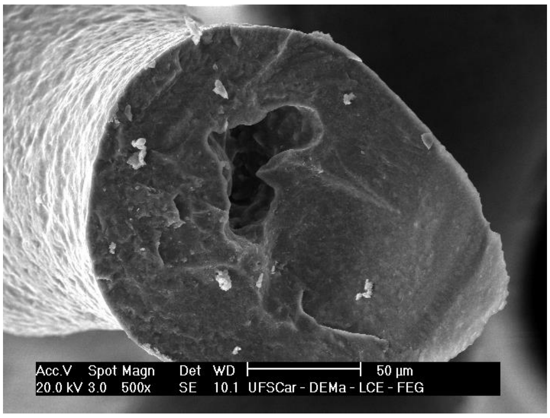
Acc.V Spot Magn Det WD 50 µm
20.0 kV 3.0 500x SE 10.1 UFSCar - DEMa - LCE - FEG

(e)

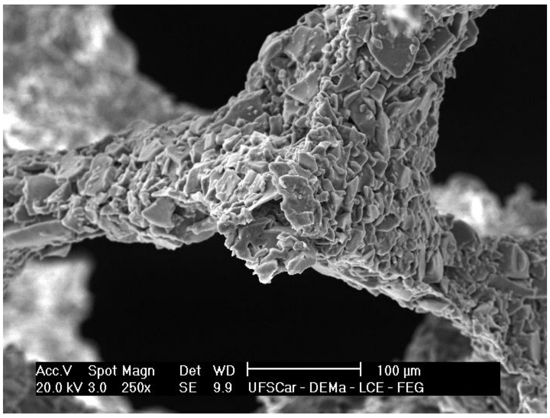
Acc.V Spot Magn Det WD 100 µm
20.0 kV 3.0 250x SE 9.9 UFSCar - DEMa - LCE - FEG

(f)

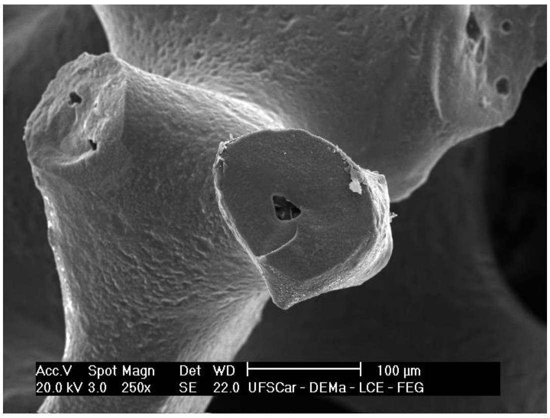
Acc.V Spot Magn Det WD 100 µm
20.0 kV 3.0 250x SE 22.0 UFSCar - DEMa - LCE - FEG

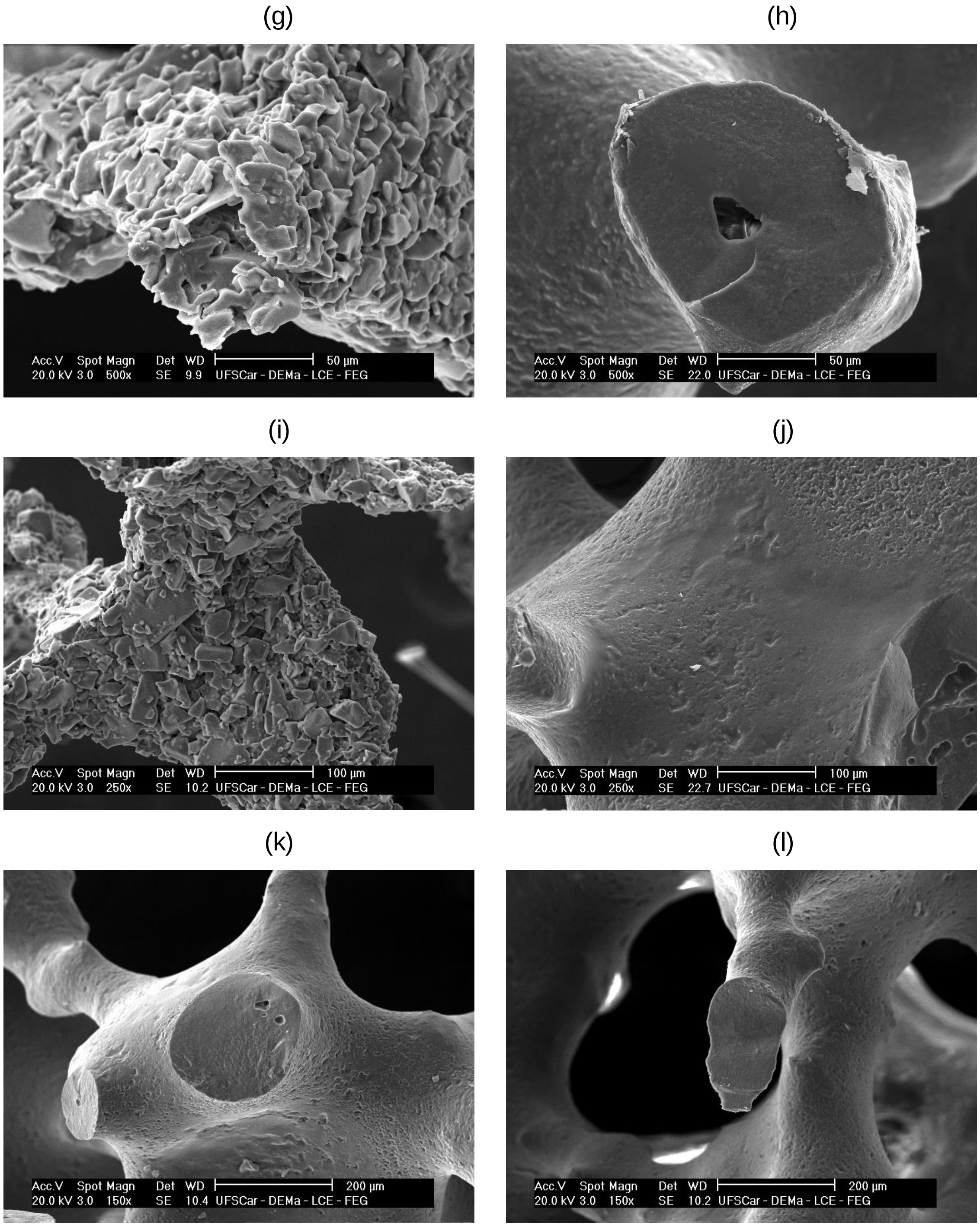

Figure 4.31 - SEM micrographs showing 590C.BioS scaffolds with highly interconnected and open pores (a) before and (b) after F18 glass coating, fabricated by the foam replica method. SEM micrographs showing the microcracks and micropores in the 590C.BioS-struts (c) and (g) before, and (d) and (h) after F18 glass coating amplified 500 times. SEM micrographs showing microcracks and micropores in the 590C.BioS-struts (e) and (i) before, and (f) and (j) after F18 glass coating amplified 250 times. And SEM micrographs showing structures that were infiltrated and (k) nearly or (l) completely closed for F18 glass amplified 150 times.

4.3.4.2 Porosity

The average cell sizes for 590-PU foam and F18-590C.BioS scaffolds were 590 ± 170 μm and 525 ± 220 μm, respectively. Also, the size distributions were found in the range from 310 to 1230 μm and from 230 to 1140 μm, respectively. The total porosity for F18-590C.BioS scaffolds was 82.0 ± 1.3% (Table 4.7). This value is similar to that presented for F18-860SP.BioS scaffolds (83%). Human trabecular bone presents a porosity range from 70% to 90%; nevertheless, a porosity over 90% could affect the mechanical properties of the scaffold (WANG et al., 2017; WU et al., 2010). Therefore, the maximum permeability must be reached without affecting the mechanical integrity of the scaffold (CHIN et al., 2017). Some *in vitro* and *in vivo* studies have found that Biomaterials with a porosity close to 80% exhibited better bone ingrowth, bone tissue formation, cellular proliferation and viability (DE OLIVEIRA et al., 2018; WANG et al., 2017).

When the average cell size of 590-PU foam (590 μm) and F18-590C.BioS scaffolds (525 μm) are compared, it can be noted that these values are similar. This happened because the linear shrinkage during sintering process was little. An interconnected pore structure with an average cell size of 525 μm and a porosity higher than 80% are essential for cell penetration, tissue ingrowth, new vascularization, and nutrient delivery (BOCCACCINI; CHEN; REZWAN, 2007).

Table 4.7 - Total porosity, average cell size, and compressive strength for the Biosilicate scaffolds, synthesized with 590C-PU and 860SP-PU foams, after coating with F18 glass.

Scaffold type	Total porosity (%)	Average cell size (μm)	Compressive strength (MPa)
F18-590C.BioS	82.0 ± 1.3	525 ± 220	3.3 ± 0.3
F18-860SP.BioS	83.0 ± 2.0	770 ± 290	1.0 ± 0.2

4.3.4.3 Compressive strength

To do these tests, aluminum discs were joined parallel to scaffold faces using an epoxy resin, as shown in Figure 4.32.

It was found that the average compression strength for F18-590C.BioS scaffolds was 3.3 ± 0.3 MPa (Figure 4.33). This value was bigger than that (1.0 MPa) found for F18-860SP.BioS scaffolds. Considering that struts of 590-PU foam are thinner than those of 860-PU foam, it is reasonable to think that the triangular voids produced during foam burning have smaller sizes, increasing the mechanical strength of the structures. Figure 4.34 shows that when the cell size of the ceramic foams diminishes, their mechanical strength increase. As has been noted, the mechanical strength of F18-590C.BioS scaffolds was 2.3 MPa bigger than that of F18-860SP.BioS scaffold, this happened because the sacrificial polymer template, 860-PU foam, was changed to 590-PU foam whose average cell size is 30% smaller. Other factor related to this result is that when cell size reduces, the porosity of the foam does too.

Desimone, *et al*. found that Biosilicate scaffolds synthesized by replica technique using 45 ppi PU foam have compressive strength of 0.06 ± 0.01 MPa when the porosity is 95% and the average cell size is 350 µm (Figure 4.34) (DESIMONE et al., 2013). We found that 860SP-BioS scaffolds (35 ppi) have a compressive strength of 0.02 MPa, a porosity of 96% and an average cell size of 830 µm (Figure 4.34); after F18 glass coating, 860SP-BioS scaffolds showed an increase in mechanical strength of 1 MPa and their total porosity and cell size were 83% and 770 µm, respectively. Similarly, when the 590C.BioS scaffolds (45 ppi) were recoated with F18 Bioglass, their mechanical resistance increased significantly (3.3 MPa) compared with Biosilicate scaffolds synthesized by Desimone *et al.* As shown above, the total porosity of the latter was 13% higher than that of F18-590C.BioS scaffolds; this porosity reduction represented one increase in compressive strength of more than 3 MPa. This behavior has been observed in other studies that have established that a porosity reduction of 10% can cause an increase of compressive strength from 2 to 15 MPa (CHEN; THOMPSON; BOCCACCINI, 2006; GERHARDT; BOCCACCINI, 2010). One factor that contributed to this porosity reduction was the homogeneous F18 glass layer deposited over strut surface, which increased the thickness of the struts strengthening the structure. Moreover, F18 glass coatings sealed cracks present in microporous 590C.BioS-struts increasing the mechanical integrity of the overall scaffold. Another key point is that F18 glass slurry penetrated inside the hollow 590C.BioS-struts, filling partially the voids and increasing the structure resistance. This showed that several infiltrations with F18 glass slurry, under vacuum, increased significantly the mechanical properties of the 590C.BioS scaffolds. To summary, F18-590C.BioS scaffolds have a compressive strength in the range of values for trabecular bone (2-12 MPa), a high bioactivity (osteoconduction and osteoinduction), a highly interconnected porous structure, an adequate cell size and an appropriate porosity, which allow them to mimic the trabecular bone structure inducing the osteogenesis process. Moreover, a compressive strength similar to that of trabecular bone is enough for dentistry applications such as sinus lifting and vertical augmentation surgeries, which do not involve high load-bearing bones, and consequently, the scaffolds are not under strong tensions giving the adequate resistance to the tissue during healing process.

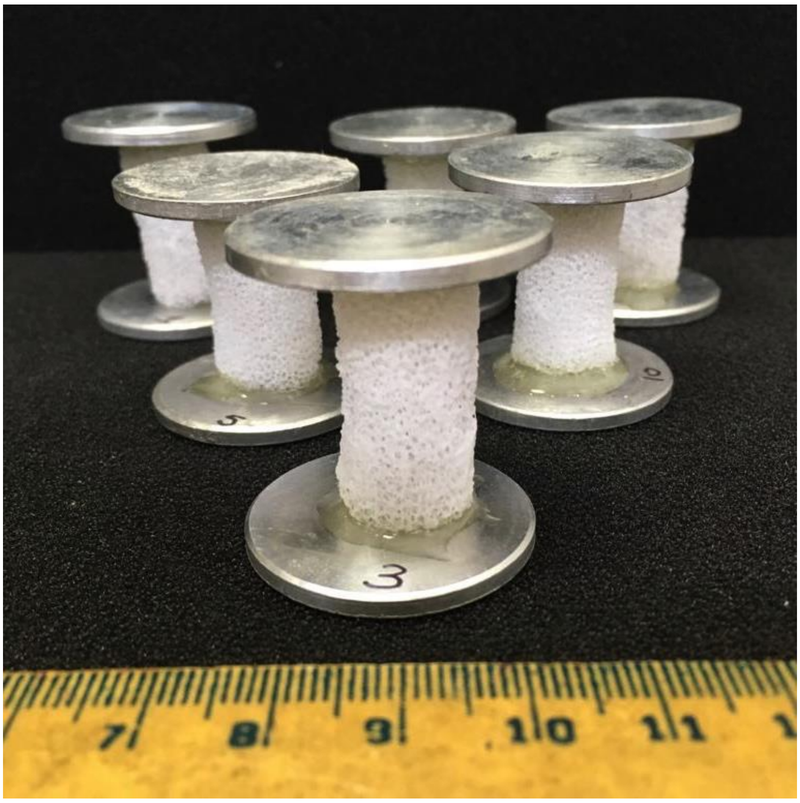

Figure 4.32 - Image showing the arrangement of F18-590C.BioS scaffolds for mechanical tests.

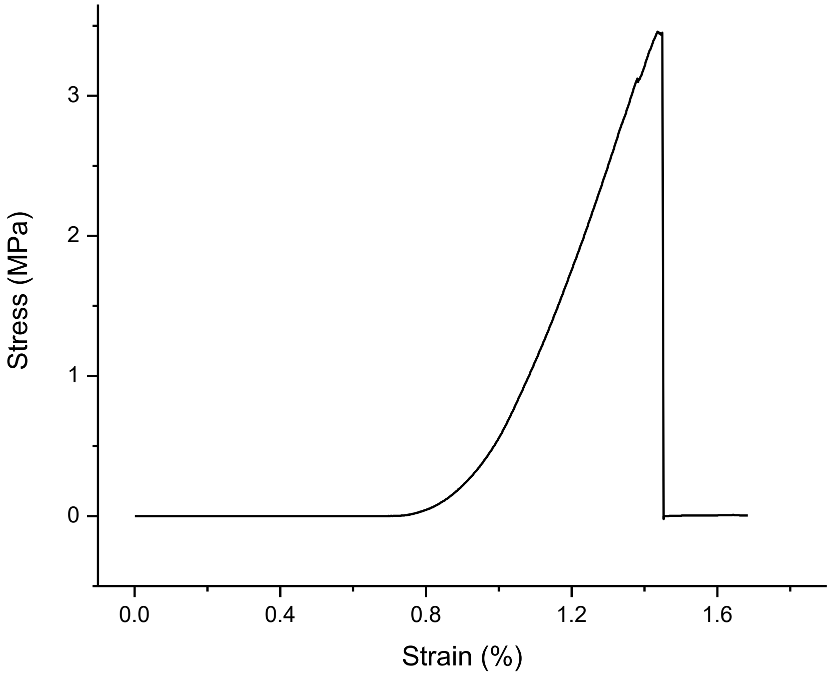

Figure 4.33 - Typical stress-strain curve for F18-590C.BioS scaffolds.

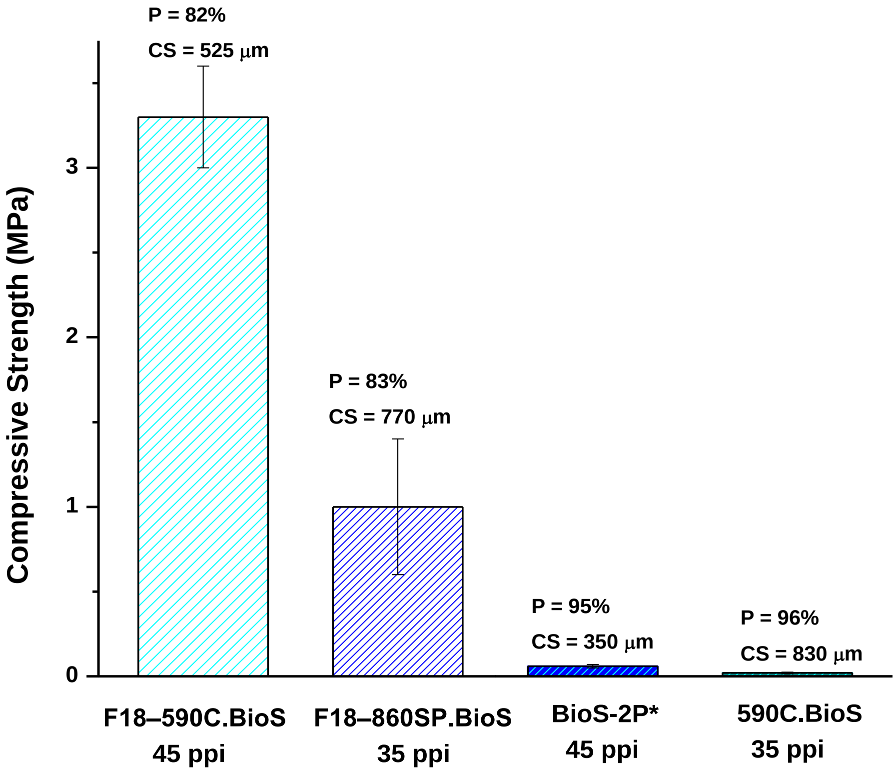

Figure 4.34 - Bar graph comparing the compressive strengths between F18 glass-coated Biosilicate scaffolds synthesized using 45 ppi and 35 ppi PU foams; and between Biosilicate scaffolds synthesized using 35 ppi and 45 ppi PU foams. P = porosity and CS = cell size. * Scaffolds synthesized by Desimone, *et al*. (DESIMONE et al., 2013).

Figure 4.35 shows the comparison among the values of the compressive strength calculated using the Ryshkewitch and Gibson & Ashby models and the experimental data obtained for F18-590C.BioS scaffolds, when n = 5, σ_0 = 250 MPa and porosity is 82%. As can be seen in Table 4.8, the experimental value was near to theoretical ones. Nevertheless, it was lower since the Ryshkewitch model is for dense materials and the modified Gibson & Ashby model assumes that the structure is not hollow in the central region of the struts. Given these points, it is reasonable that the experimental value be lower. Although, the experimental data fitted well to both models when n = 5 and σ_0 = 250 MPa, it is necessary to determine the exact values of these constants to verify if the experimental data really fit well to both models.

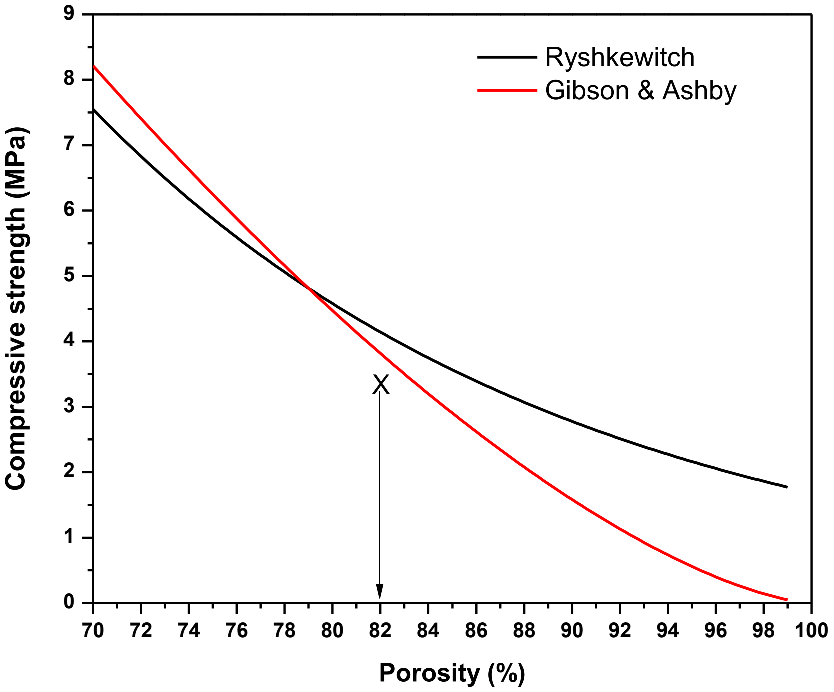

Figure 4.35 - Comparison among the compressive strength values calculated by the Ryshkewitch (equation 4.1) and Gibson & Ashby (equation 4.4) models (n = 5 and σ_o = 250 MPa), and the compressive strength of F18-590C.BioS scaffolds (X = 3.3 MPa) whose porosity is 82%.

Table 4.8 - Values of the compressive strength calculated by the Ryshkewitch (equation 4.1) and Gibson & Ashby (equation 4.4) models and the experimental data for the F18-590C.BioS scaffolds. Porosity for calculated and experimental data was 82%.

σ_c (MPa) Ryshkewitch [σ_0 = 250 MPa, n = 5]	σ_c (MPa) Gibson & Ashby [σ_0 = 250 MPa]	σ_c (MPa) F18-590C.BioS scaffolds
4.1	3.8	3.3

On the other hand, one possible strategy to increase the mechanical strength of the scaffold could be try to reduce the size of the hollow structure using one 60 ppi PU foam and smaller particle sizes to prepare the slurries. Similarly, when the cell size of PU foam diminished from 860 µm to 690 µm, it was noted that size of the void region in the center of the struts decreased too. Even though, the 60 ppi PU foam has an average cell size near to the inferior limit (300 µm), probably the reduction of cell size during sintering process would be little, conserving the ideal pore size for bone regeneration.

4.4 *In vitro* assays over scaffolds using MSC

All tests in this section were done using F18 glass-coated 590.BioS scaffolds (F18-590.BioS).

4.4.1 Human pluripotent stem cells and fibroblasts

Differentiation of human induced pluripotent stem (iPS) cells was performed using MesenCult^{TM} osteogenic differentiation kit (Human) (StemCell-Catalog #05465) and according to the manufacturer's instruction.

This kit was used to induce differentiation of human iPS cells into MSCs, which could have been subsequently differentiated into osteoblasts. These cells were chosen because of their high potential for application in BTE. The cells were passaged in a 6-well plate using TeSR™-TESR-E8™ medium to expand them over the plate (control) and the scaffolds. As can be seen in Figures 4.36a and 4.36b, after 2 days, control and scaffold samples exhibited human iPS cells morphology. When the cells reached complete confluence, complete medium was changed for induction medium to initiate differentiation process. After four days with the induction medium, many human iPS cells had died over bottom of the wells for the control and the scaffold samples (Figure 4.36c and 4.36d). To verify if cells had been able to adhere and survive over material surface, an assessment of cell viability (live/dead staining) was performed over scaffolds (Figure 4.37). This confirmed that the cells had died over biomaterial, but nevertheless, these were able to adhere over the scaffold surface. To avoid the loss of confluence was added more induction medium in each well.

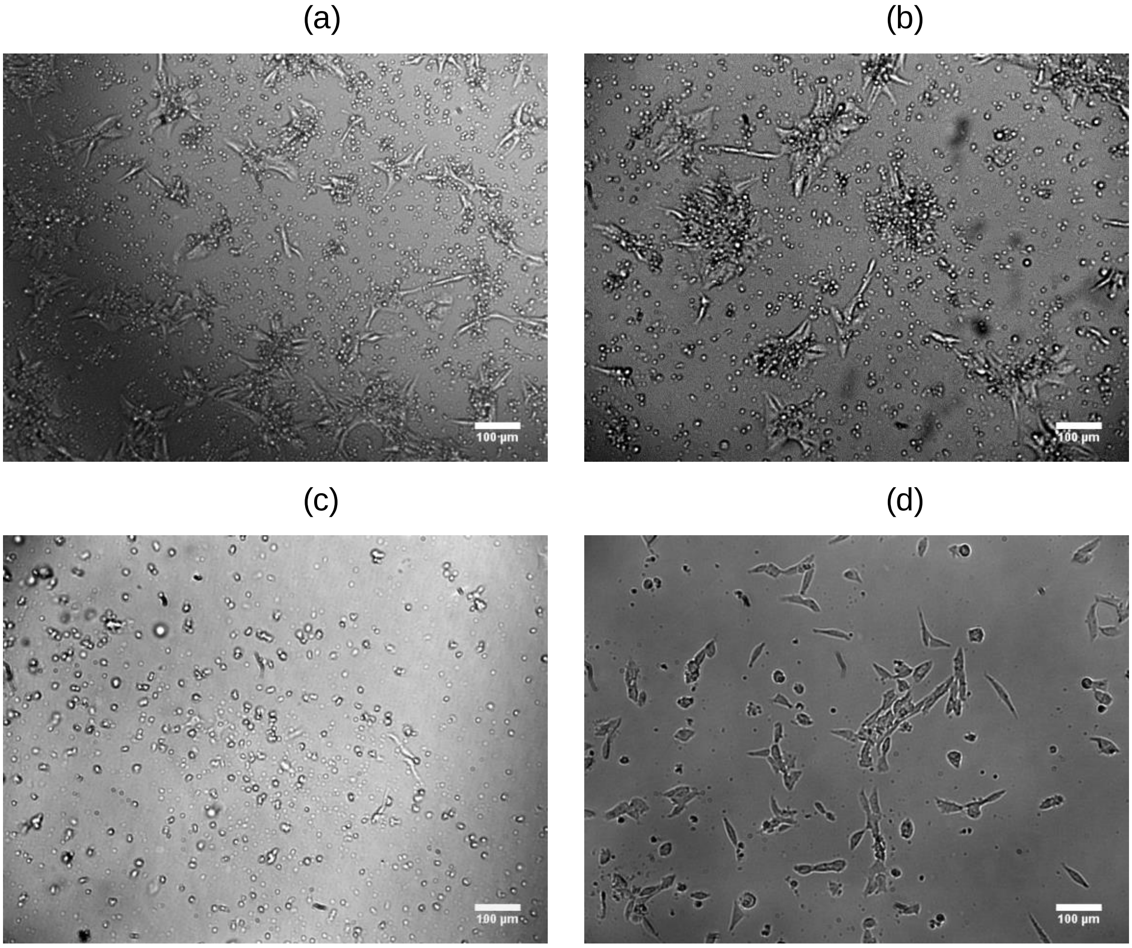

Figure 4.36 - Cell morphology of human iPS cells passaged a) on the plate using only TeSR™-TESR-E8™ (control) and b) over scaffolds at day 2. Human iPS cells in induction medium for 4 days for c) scaffold and d) control. Scale bar represents 100 µm.

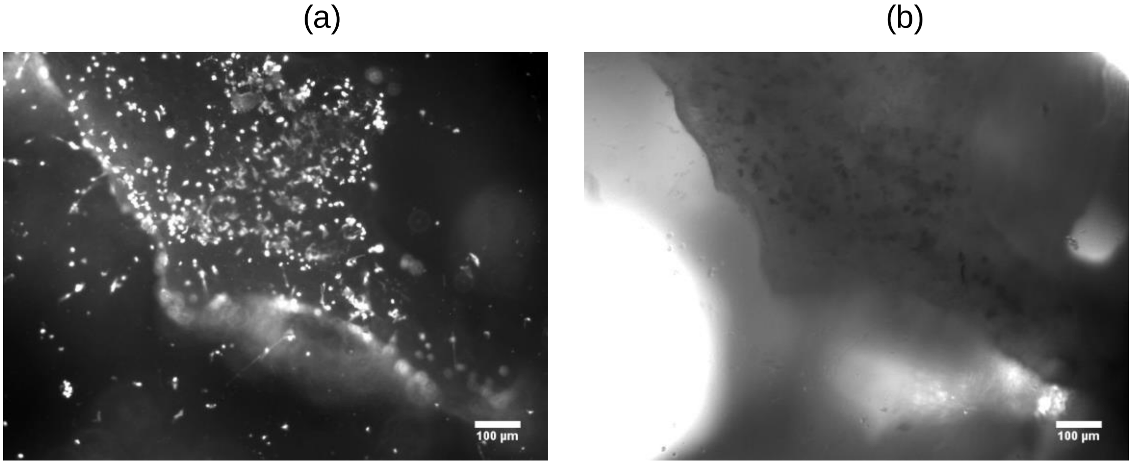

Figure 4.37 - a) Photo of dead cells over scaffold after live/dead staining when induction process finished, bright dots are dead cells and b) photo of optical microscope showing the same place on the scaffold. Scale bar represents 100 µm.

After process induction finished, derivation over the cells was induced. It were carried out six passages of cells (Figure 4.38), but unfortunately, the cells appeared to be sick (Figure 4.38a and 4.38c) and in some cases they showed one elongated shape (Figure 4.38b and 4.38d); this suggested that they have undergone a kind of differentiation. For that reason, the medium was changed more frequently, and cells were washed with PBS (Figure 4.38d), but any improvement was not observed. In all passages, the cells presented some black dots, and cell shape was flat; but, it did not seem as though they were contaminated with bacteria or fungi. Under those circumstances, the sick cells were kept in culture more time, even though no change was observed.

To evaluate the undifferentiated state of cells was done immunochemistry (annex B) during the derivation process after 5 passages. DAPI was used for nuclei staining, which is depicted in blue; moreover, it was used vimentin (depicted in red) that is a marker relates with the undifferentiated state and is expressed in all mesenchymal cells (Figure 4.39) (GARCIA, 2012; JANEBODIN et al., 2011). This marker is a cytoskeletal intermediate filament and is important for cell attachment and spreading (ŚMIESZEK et al., 2017). Figure 4.39 suggests that cells during the derivation process, at passage 5, preserved their pluripotency.

Material toxicity was evaluated because scaffolds released many particles into medium and many cells died. Hence, cell viability was estimated using fibroblasts (annex C) instead of human iPS cells because fibroblasts are stronger cells. As can be seen in Figure 4.40, cells survived and adhered over bottom of the well and over material and they presented a good confluence after expanding using AM medium for 2 days. Over the bottom of the wells was observed a high quantity of live cells. This confirmed that material did not affect the survival of human iPS cells when they were cultivated over scaffolds. As a conclusion, the induction medium is not adequate to culture and differentiate human iPS cells into MSCs. For that reason, human iPS cells were changed for human Adipose-derived mesenchymal Stem Cells (hASCs) to carry out all experiments.

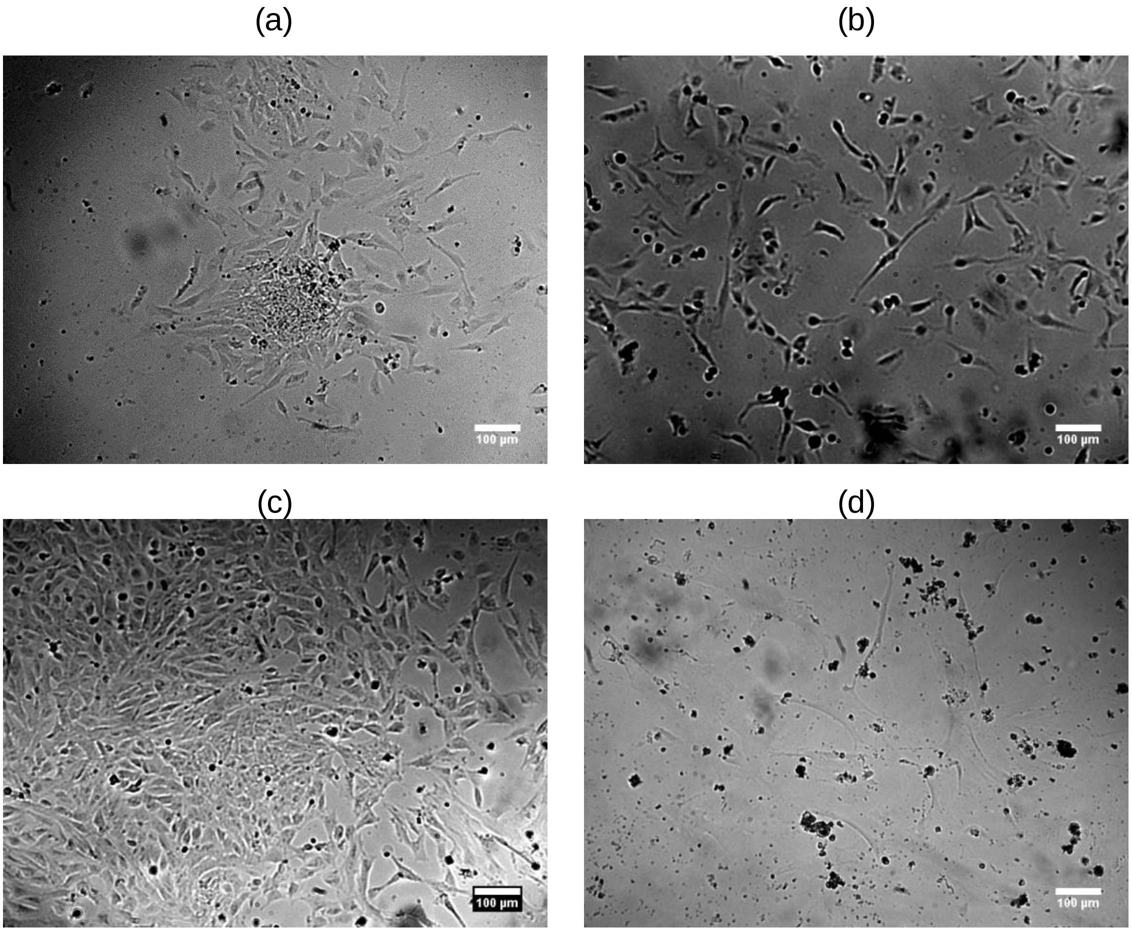

Figure 4.38 - Images of human iPS cells after derivation a) second passage, b) fifth passage, c) sixth passage and d) cells washed with PBS. a-c are controls and d is scaffold group. Scale bar represents 100 µm.

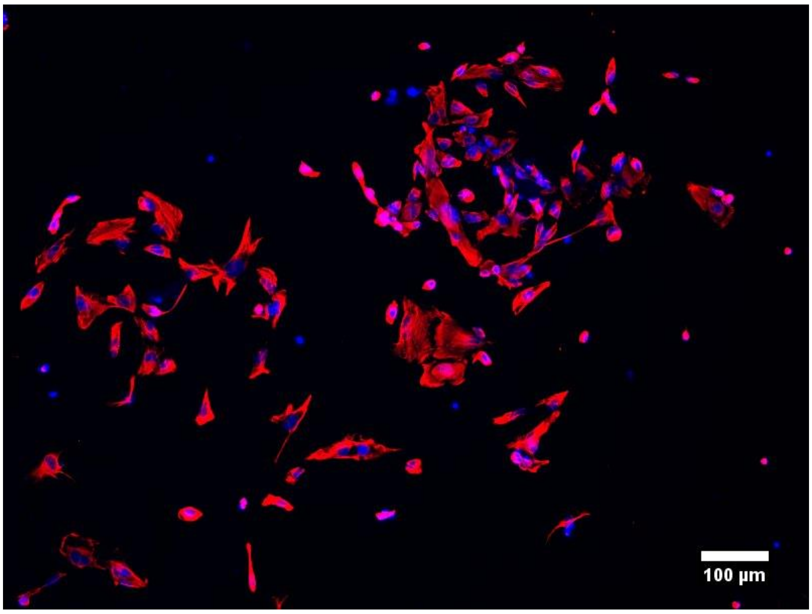

Figure 4.39 - Immunohistochemistry of human iPS cells (fifth passage) after derivation using the vimentin (Red) and DAPI (Blue) antibodies. Scale bar represents 100 µm. The images were merged using the ImageJ software.

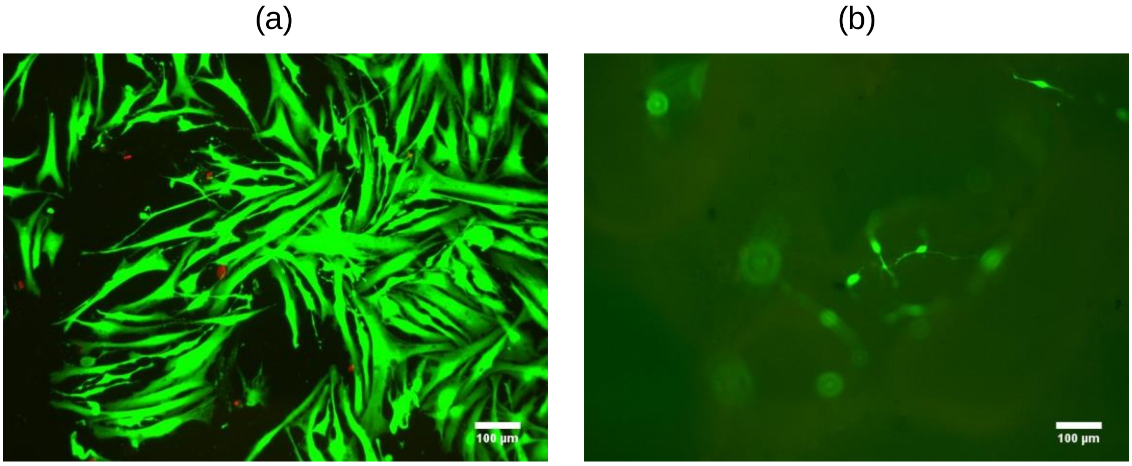

Figure 4.40 - Images of live/dead staining of fibroblasts cultivated in AM medium at day 2 a) over bottom of the well and b) over scaffold. Scale bar represents 100 µm. The images of the live and dead cells were merged using the ImageJ software.

4.4.2 Cell culture

The ion concentration in the osteogenic medium (dissolution product group) used to differentiate cells is showed in Table 4.9.

Table 4.9 - Concentration of calcium, sodium, and phosphate ions released for F18-590.BioS scaffolds when they were in contact with the osteogenic media for 48 hours at 37 ºC.

Ions	Concentration mmol.L^{-1}
Calcium	0.35
Phosphate	0.26
Sodium	10.0

In Figure 4.41 is shown the morphology of hASCs 24 hours after expanding in MSCM. Figure 4.41a shows the hASCs used for the control and the dissolution product group; both of them had the same conditions in this stage. When these cells are compared with ones passaged over scaffolds (Figure 4.41b), no differences were found in their morphologies. This indicates that the scaffolds do not generate any adverse environment for cellular growth during expansion. Figure 4.41c showed hASCs cultured in MSCM for four days, which have reached almost 100% confluent. Cells showed both hASCs morphology and healthy state, being appropriate for passaging and differentiating *in vitro* using MODM.

After exchanging MSCM for MODM, hASCs were able to survive for three weeks in all experiments without drawback (Figure 4.42). As can be observed in Figures 4.42a, 4.42b, and 4.42c after three days in osteogenic medium, cells showed good confluent, and in general, cell morphology for the control, the F18-590.BioS scaffold, and the dissolution product group are similar. After seven days of incubation with osteogenic differentiation medium, dark brown cell multilayers were observed under microscope (Figures 4.42d to 4.42f). This phenotypic change is attributed to matrix maturation. After matrix secretion by osteoblasts occurs, maturation phase is performed generating polymerization of collagen into an array of fibrils, bonds between collagen fibrils and calcium, and formation of protein-glycoaminoglycan complexes (DONALD; HEANEY, 2019; KOMAROVA et al., 2015). At 14 days, the dark zones increased in the plates. During this stage known as mineralization occurs the precipitation of calcium and phosphate that form hydroxyapatite [$Ca_{10}(PO_4)_6(OH)_2$] crystals within the organic bone matrix (Figure 4.43a). The mineralization was considerably higher in the scaffolds and the dissolution product group than in the controls (Figure 4.42g-4.42l). This is one qualitative probe that both scaffolds and dissolution products benefit the mineralization.

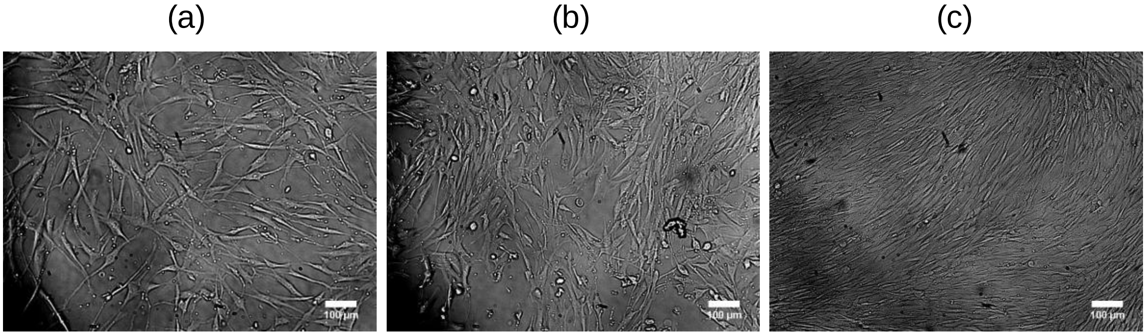

Figure 4.41 - Cell Morphology of hASCs a) in MSCM after 1 day, b) passaged over scaffold after 1 day and c) in MSCM after 4 days. Scale bar represents 100 µm.

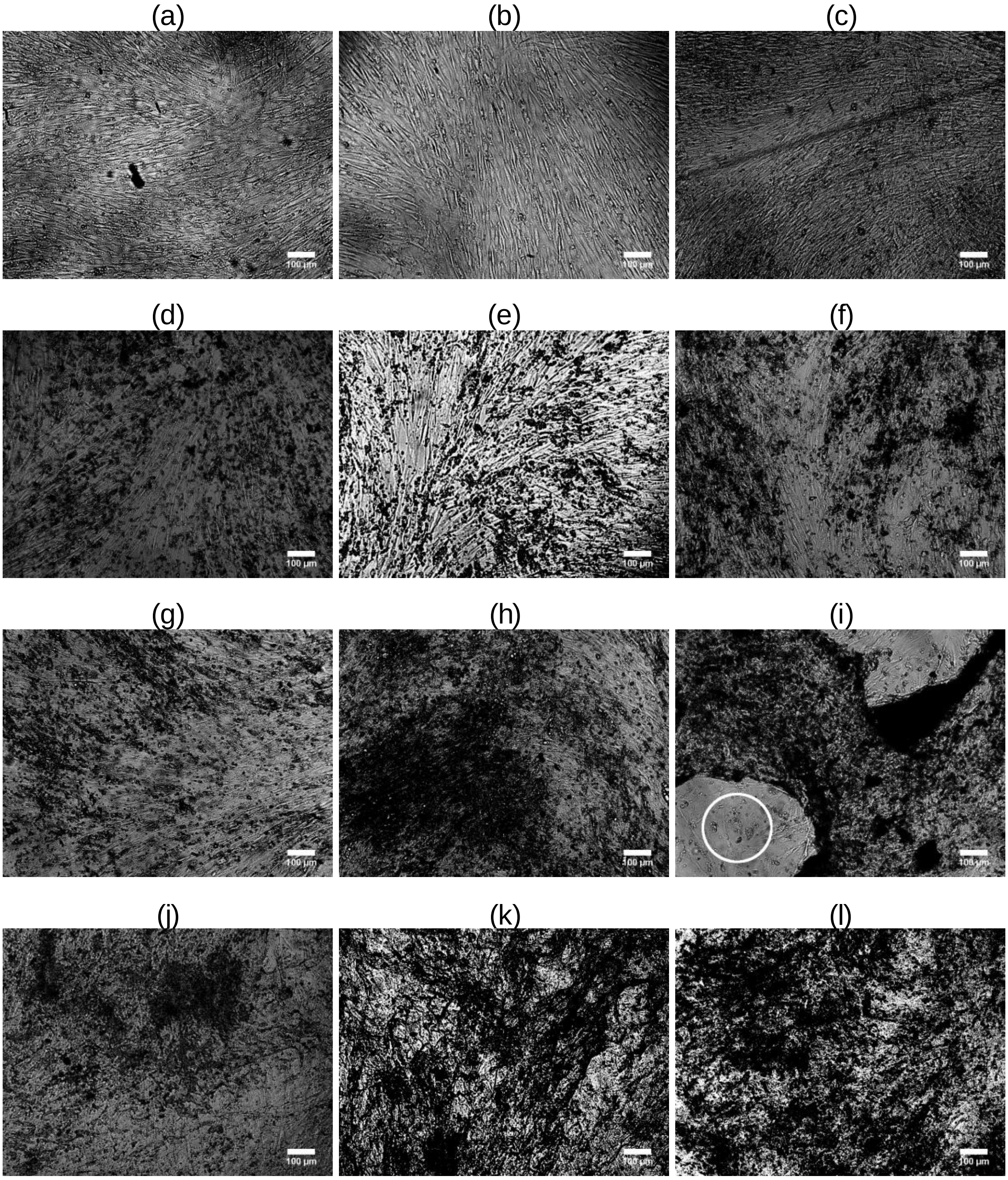

Figure 4.42 - Cell morphology of hASCs (M x100) after 3 days in osteogenic medium (MODM) for a) the controls, b) the dissolution product group, and c) the scaffolds; after 7 days in MODM for d) the controls, e) the dissolution product group, and f) the scaffolds; after 14 days in MODM for g) the controls, h) the dissolution product group, and i) the scaffolds (the white circle is over a place with little confluence); after 21 days in MODM for j) the controls, k), the dissolution product group, and l) the scaffolds. Scale bar represents 100 µm.

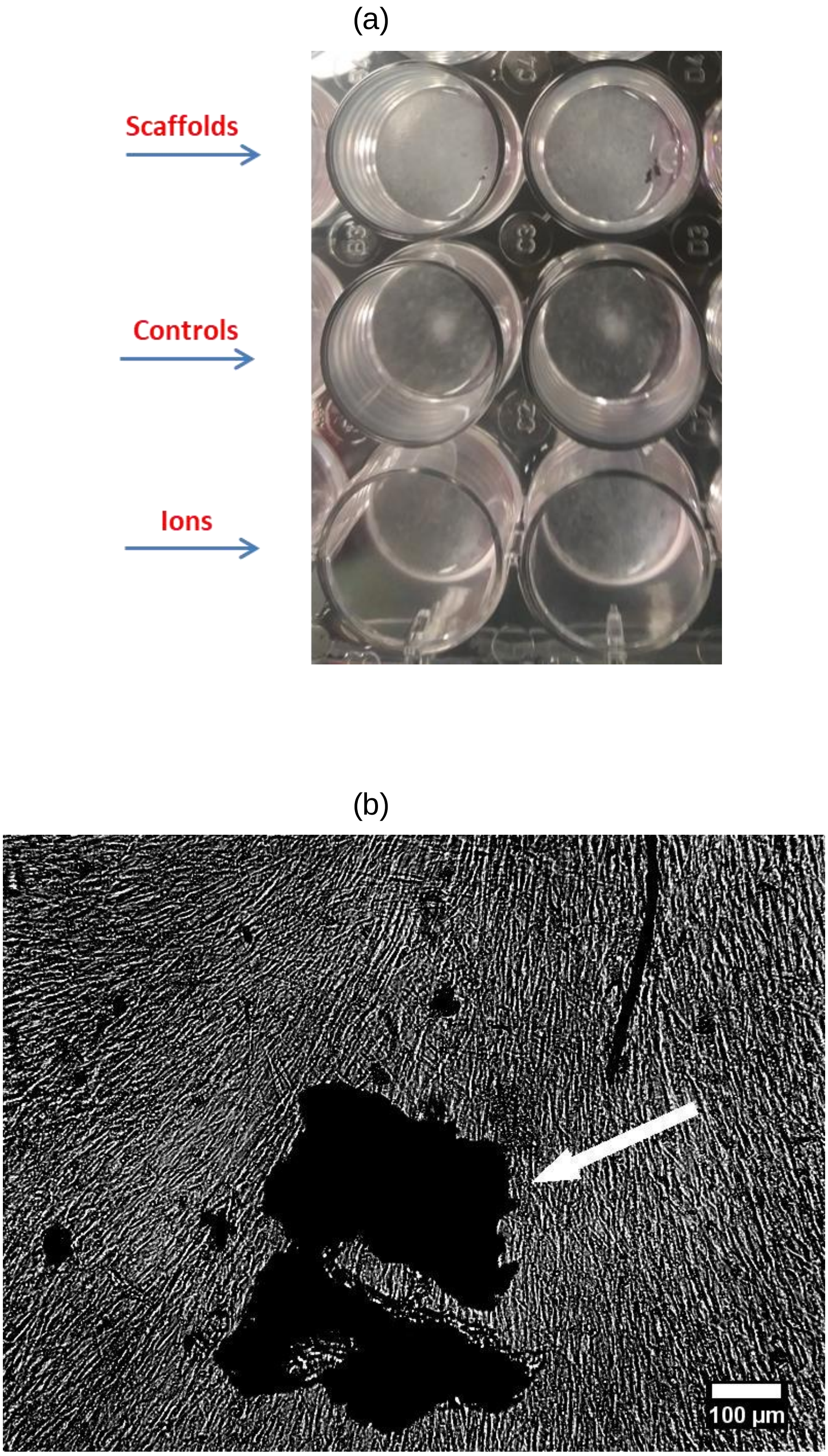

Figure 4.43 - a) Photo of hASCs cultured in 24-well plate using osteogenic medium for 14 days, b) hASCs (M x100) cultured using osteogenic medium and F18-590.BioS scaffold for 7 days, the white arrow points the particles released for the scaffold. Scale bar represents 100 µm.

On the other way, scaffolds presented zones where the confluence decreased markedly (Figure 4.42i, white circle), this was caused by the particles (Figure 4.43b) released for the material in contact with the medium, which accumulated over the cells disrupting the homeostasis that caused cell death. In multicellular organisms, proliferation and differentiation are regulated by external signals that involve the activation of complex mechanisms of the intercellular communication. In human, these mechanisms are based on cells communication with each other through non-contacted endocrine, autocrine or paracrine signaling via secreted chemicals; and cell-contact-dependent signaling. Several studies have shown that cell-cell interactions that are carried out by contact among neighboring cells, transfer of intracellular proteins, or soluble paracrine factors play a critical role in preserving stem cell homeostasis in culture (BORN et al., 2009; SELIMOVIĆ et al., 2013). Moreover, cellular interaction with the ECM and neighboring cells is necessary for osteoblast survival, proliferation, and differentiation (BORN et al., 2009). As a matter of fact, inhibition of gap junctional communication is related to reduction of osteoblast differentiation potential (STAINS; CIVITELLI, 2005). Probably, all these factors could have been altered for the released particles in cultures, affecting the confluence on the bottom of the 24-well plate of the scaffold samples. Despite of this fact, the confluence was bigger than 85%, being enough to get healthy osteoblasts cultures.

4.4.3 Assessment of cell viability

Live/Dead Staining was done to evaluate cell viability of hASCs in the controls, the scaffolds and the dissolution product group after being in contact with the MODM for two days. As can be seen in Figures 4.44a, 4.44b, and 4.44c, almost all cells were alive in the bottom of the wells of all groups. This means that the materials did not generate a toxic environment for cell differentiation, which permitted cell growth and the osteogenic process to be performed without any inconvenience. Moreover, in Figures 4.44d can be seen that hASCs were able to adhere and proliferate over the material surface. The results of cell viability over scaffold surface were confirmed with Guava®

ViaCount™ Reagent (Annex D). Surface properties such as topography, chemistry or surface energy establish how biomolecules adhere over the surface of biomaterials (ANSELME, 2000). Moreover, topography can help to induce certain factors involved in osteogenesis getting better the healing process (HAKKI; BOZKURT; HAKKI, 2012). Hakki *et al.* evaluated osteogenic expression of different factors when MC3T3-E1 cells were cultivated over titanium implants with surface of different roughness; they found that attachment and expression of the key factors such as BSP (bone sialoprotein), OCN (osteocalcin), SPP1 (osteopontin), ALP, COL I, MMP2, MMP9, different collagen types, FGFs, BMP2, BMP3, BMP5, BMP6 and their receptor were increased in roughness surfaces (HAKKI; BOZKURT; HAKKI, 2012). When the implant is in contact with the cells, it is vital attachment and diffusion of active matrix over porous roughness to facilitate osseointegration (HAKKI; BOZKURT; HAKKI, 2012).

The first contact between hASCs and material surface created contact focals that were mediating by vitronectin, this glycoprotein possesses the RGD sequence that is recognized for cell surface receptors such as integrins. When integrins bound to vitronectin, specialized protein clusters are formed, which induce both adhesion and directed assembly of actin filaments and signaling components as well as cytoskeletal tension changes, generating a series of mechanochemical signal pathways that induce osteogenesis process (BORN et al., 2009; SHEN et al., 2018). Therefore, in the initial stage of osteogenesis can be established that F18-590.BioS scaffolds foster the cell adhesion, which is essential for cell proliferation and differentiation. For the dissolution product group was observed a high amount of alive cells too (Figure 4.44b); it is a well-known fact that ions such as Na^+, Ca^{2+}, silicon and phosphate ions released for Biosilicate scaffold in the osteogenic medium are able to induce genetic control over the genes that regulate osteogenesis inducing differentiation (HOPPE; GÜLDAL; BOCCACCINI, 2011).

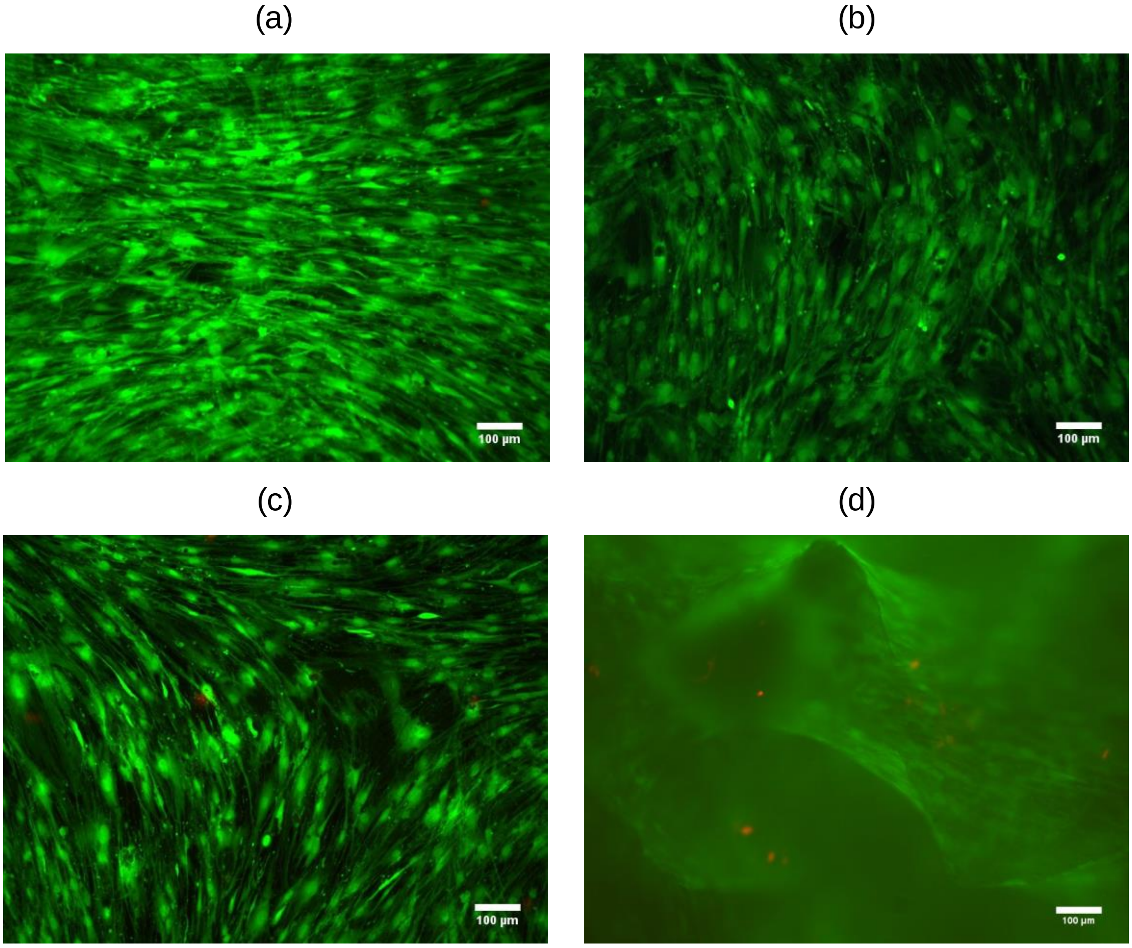

Figure 4.44 - Photos of the Live/Dead tests taken with an optical microscope after two days of culture in MODM for a) the controls, b) the dissolution product group, c) and d) the scaffold samples. a, b, and c are from bottom of the wells and d is over the scaffold surface. Green parts represent live cells, and red points represent dead cells. Scale bar represents 100 µm. The images of the live and dead cells were merged using the ImageJ software.

4.4.4 ALP staining and activity

ALP is an early marker for osteogenic differentiation that helps in the formation of bone-like nodules, which are employed during matrix mineralization (YANG et al., 2017). This metalloenzyme catalyzes the hydrolysis of phosphate esters being generated the phosphate groups need for the formation and deposition of hydroxyapatite during the osteogenic process. In its active site is produced serine phosphate, which is able to react with water at basic pH producing inorganic phosphate (GOLUB; BOESZE-BATTAGLIA, 2007).

Moreover, ALP fosters mineralization hydrolyzing extracellular inorganic pyrophosphate that is an inhibitor of mineralization (ORIMO, 2010).

Evaluation of this marker was done both qualitatively and quantitatively. Qualitative evaluation of ALP marker was carried out for the controls, the scaffolds and the dissolution product group after 7, 14, and 21 days in osteogenic medium. As can be seen in Figure 4.45, at day 7 and 14 all groups displayed positive ALP activity since they presented a dark purple color that is generated by the formation of insoluble NBT diformazan by the catalytic activity of ALP (section 3.10.2). On the other hand, at day 21 was observed one light blue since the ALP concentration diminished after 14 days in all groups. As is known, ALP is expressed early in the osteoblastic lineage concomitantly with the osteoid production, the organic phase of bone, but as matrix mineralization occurs, other genes such as osteocalcin begins being upregulated and ALP starts to be downregulated (DE GODOY et al., 2015; GOLUB; BOESZE-BATTAGLIA, 2007).

This result was confirmed by quantification of ALP using a colorimetric method. Figure 4.46 shows the standard curve used to determine the amount of nanomoles of *p*-Nitrophenol, which is directly proportional to ALP activity.

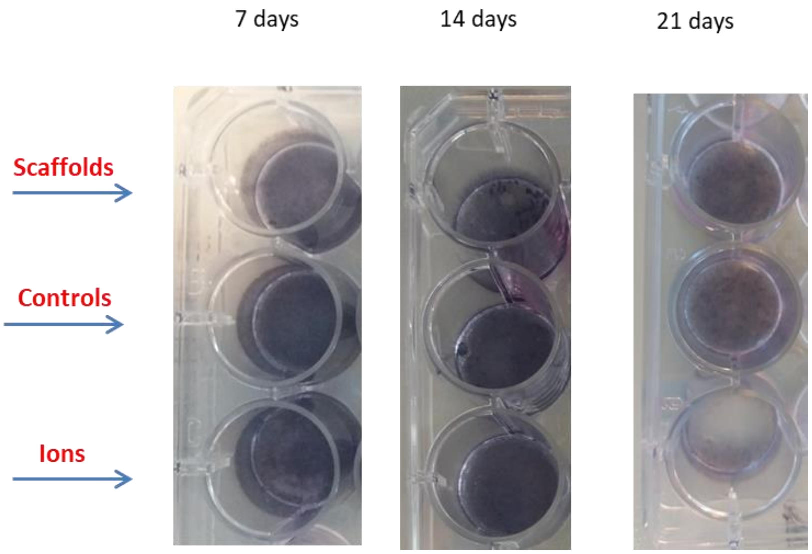

Figure 4.45 - hASCs cultured in 24-well plate using osteogenic medium for 7, 14, and 21 days were stained with BCIP-NBT.

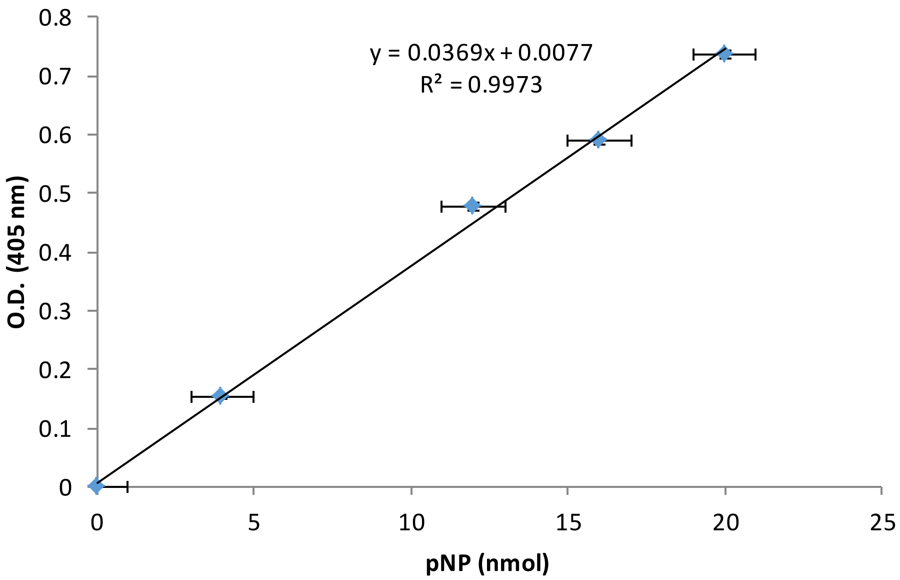

Figure 4.46 - *p*NP (p-Nitrophenol) standard calibration curve.

ALP activity normalized to the total DNA was confirmed for all groups. Both the controls and the F18-590.BioS scaffolds showed an increase of ALP activity from day 7 to day 14 (Figure 4.47). The increment being higher for the F18 glass-coated Biosilicate scaffolds than for the controls, supporting the hypothesis that these kinds of biomaterials help in the osteogenesis process not only because of the high bioactivity shown by Biosilicate and F18 glass, but also because of the surface properties of the material that can induce factors that regulate osteoblastic differentiation. Moreover, the highly interconnected porous structure mimics the morphology of trabecular bone, creating an appropriate environment for the migration, cellular growth, and differentiation of hASCs. When ALP activity was analyzed for the control, the dissolution product group, and the F18-BioS scaffolds (synthesis in Annex E) on day 14, all of them presented ALP activity lower than that of the F18-590.BioS scaffolds; this happened because they do not have a highly interconnected porous structure that imitates the ECM.

Scaffolds released different ions that can induce osteogenic expression. One of them is Si ions that are able to induce osteogenic differentiation in human bone marrow stromal cells through activation of osteogenic-related signaling pathways, which elevate ALP activity and expression of the osteocalcin, RUNX2, Col I, and osteopontin (YANG et al., 2018; YU et al., 2017). Other ions released for this biomaterial are phosphate, Na^+, and Ca^{2+}, which are necessary for the formation of hydroxyapatite and foster the expression of some osteoblastic genes (CROVACE et al., 2016; HOPPE; GÜLDAL; BOCCACCINI, 2011; JONES; GENTLEMAN; POLAK, 2007; RENNO et al., 2013). At day 21, ALP activities for the controls, the F18 glass-coated Biosilicate scaffolds, and the dissolution product group were downregulated, the same results were found with ALP staining, which qualitatively showed that all groups had a little amount of ALP (pale color); moreover, similar results were got in gene expression (section 4.4.6). In different studies have been found a similar behavior, ALP activity showed an increase for 14 days and a substantial decrease in the third week (MAHDAVI et al., 2017; SHU et al., 2017). Shu *et al.* found that ALP activity for cells cultured with the nano-doped calcium phosphate cement delivery system of IGF1 and BMP2 increased for 12 days (SHU et al., 2017). Mahdavi *et al.* found that ALP expression of equine adipose-derived stem cells cultured over nano-bioactive glass-coated poly(l-lactic acid) nanofibers scaffold increased for two weeks. They noted that enzymatic activity increased when the scaffold was coated with nano-bioactive glass and it peaked at 14 days, being downregulated at 21 days (MAHDAVI et al., 2017). Yu et al. found that ALP expression of the bone marrow-derived pericytes cultured with zinc-modified calcium silicate-coated Ti-6Al-4V implants was upregulated and peaked at 14 days; additionally, ALP activity decreased at day 21 (YU et al., 2017).

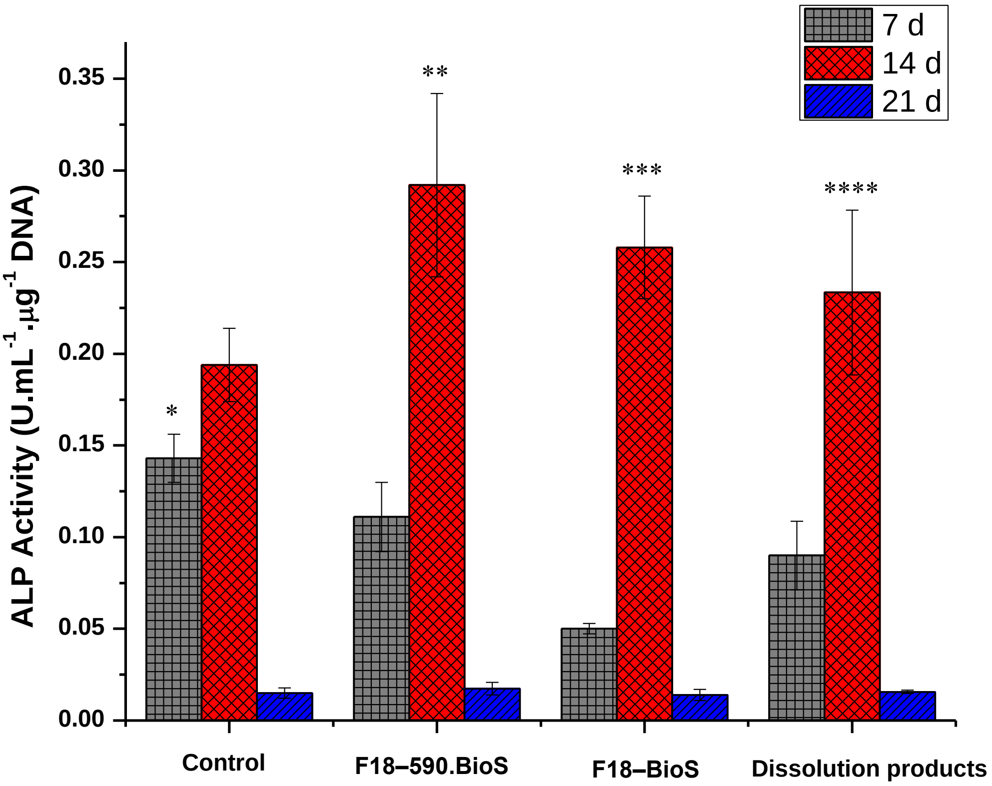

Figure 4.47 - ALP activity (µmol.min^{-1}.mL^{-1}.µg^{-1} DNA) for hASCs cultured with MODM (control), dissolution products, and F18-BioS and F18-590.BioS scaffolds at 7, 14, and 21 days, normalized with DNA content. $*$ $P < 0.05$ versus F18-590.BioS. $*$ $P < 0.05$ versus F18-BioS. $*$ $P < 0.05$ versus dissolution products. $**$ $P < 0.05$ versus control. $**$ $P < 0.05$ versus F18-BioS. $**$ $P < 0.05$ versus dissolution products. $***$ $P < 0.05$ versus control. $****$ $P < 0.05$ versus control.

4.4.5 Alizarin red staining (ARS) and quantification

First of all, staining with Alizarin Red for the controls, the F18-590.BioS scaffolds and the dissolution product group was done at day 7, 14, and 21 to assess calcium deposition. As can be seen in Figure 4.48 and 4.49, this assay permitted evaluating the formation of red nodules visually or by optical microscope, observing an increase of deposited calcium from day 7 to day 21 in all groups. Subsequently, the deposited calcium content was quantified on days 7, 14, and 21. Nevertheless, this assay is not appropriate to quantify calcium for hASCs passaged over F18-590.BioS scaffolds since this material contains calcium, and when the material is in contact with the medium, it begins releasing particles that accumulate on the bottom of the well increasing the quantity of calcium detected for this test. For that reason, it was only quantified the mineralization for the controls and the dissolution product group. The quantity of dye (ARS) extracted from cells was determined using the standard curve shown in Figure 4.50. At 7 and 14 days, calcium content of the controls and the dissolution product group were similar; but at day 21, the dissolution product group showed a higher amount of calcium than the control group (Figure 4.51). This difference may have been caused by ions released for scaffolds, which stimulated osteogenesis. As has been noted, the calcium content for both groups increased as time went by, this behavior have been observed in other studies (ATARI et al., 2012; BAGESHLOOYAFSHAR et al., 2019). Moreover, there are different factors that can lead to a better mineralization process, such as the material composition. Bagesholooyafshar *et al.* observed that Zn silicate mineral nanoparticles increased the mineralization of ASCs and Yang *et al.* found that silica nanoparticles were able to significantly increase mineralization, proliferation and differentiation of hMSCs at day 21 (BAGESHLOOYAFSHAR et al., 2019; YANG et al., 2017).

ALP and ARS tests have shown that hASCs were differentiated into osteoblasts for the controls, the F18-590.BioS scaffolds, and the dissolution product group.

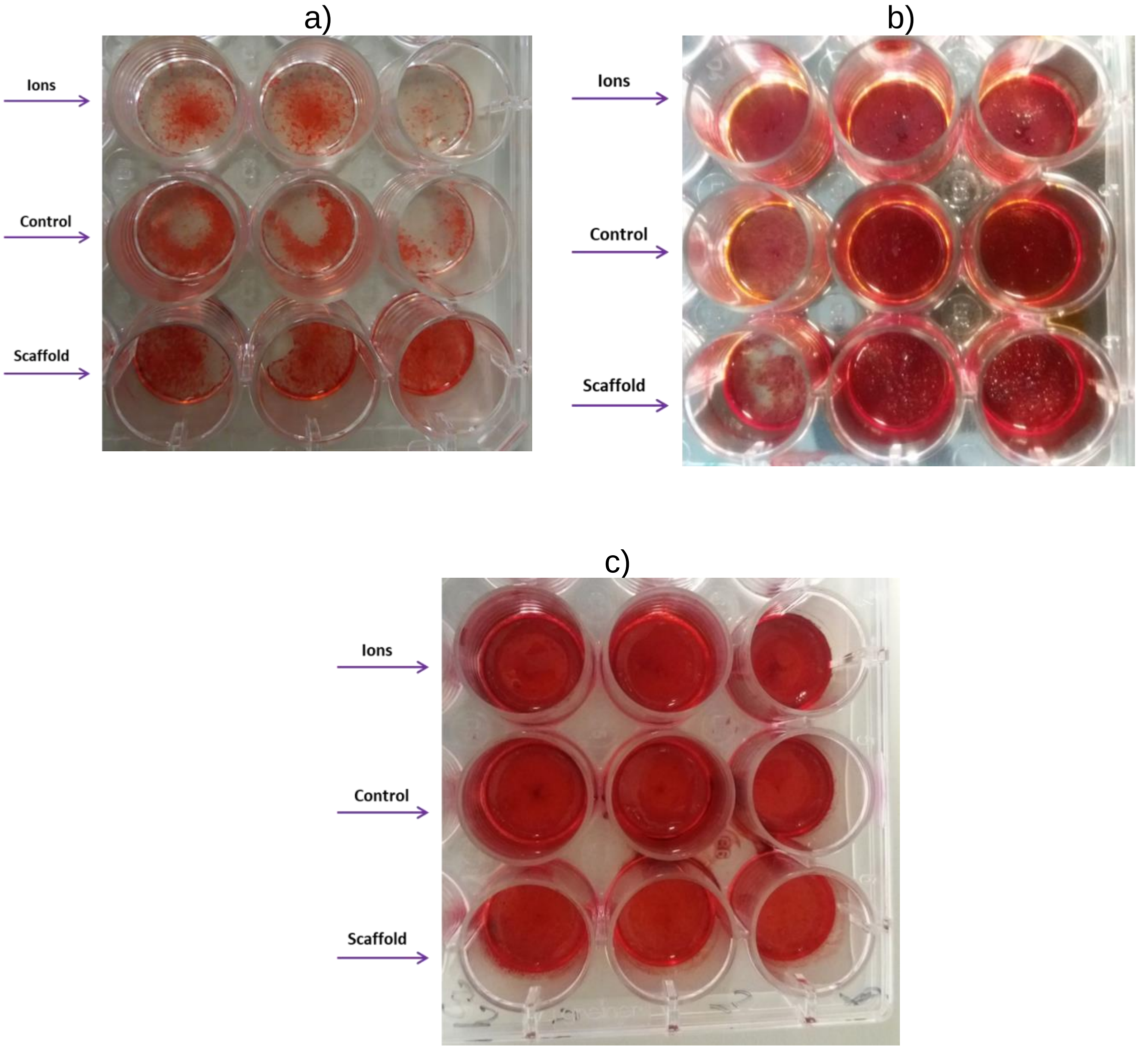

Figure 4.48 - Photos of hASCs stained with ARS. Cells were cultured in 24-well plate using MODM (control), the F18-590.BioS scaffolds, and the dissolution products at a) 7, b) 14, and c) 21 days.

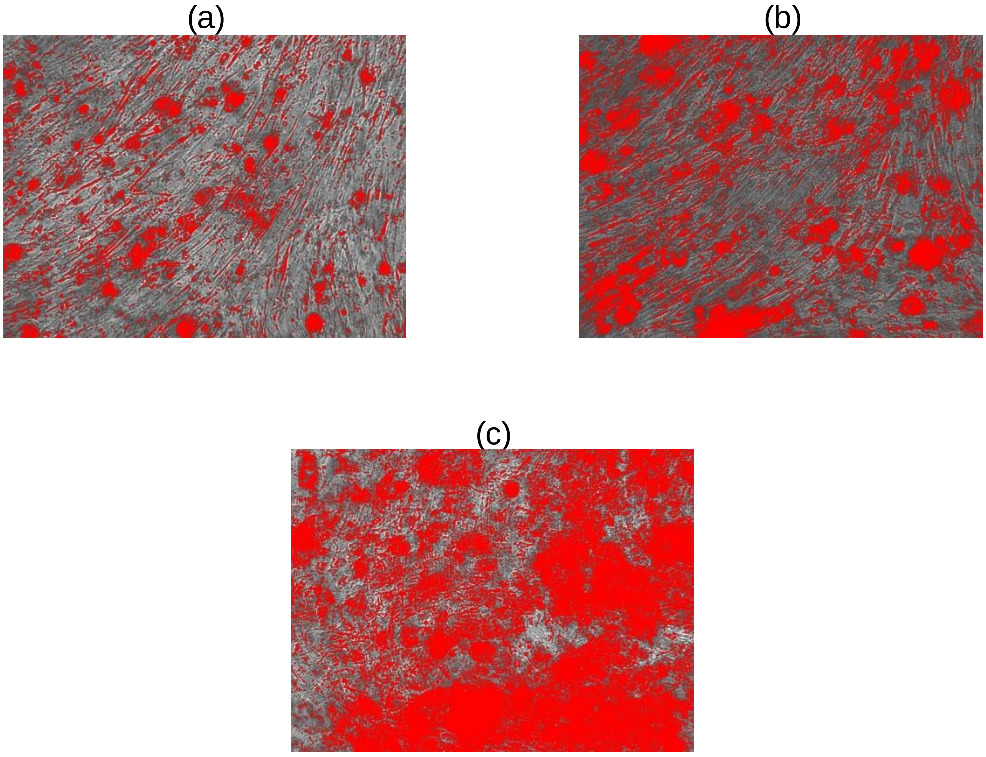

Figure 4.49 - Mineralization of hASCs. Cells cultured in osteogenic medium for 14 days and stained with ARS for a) the controls, b) the dissolution product group, and c) the F18-590.BioS scaffolds. Images were modified using the software imageJ.

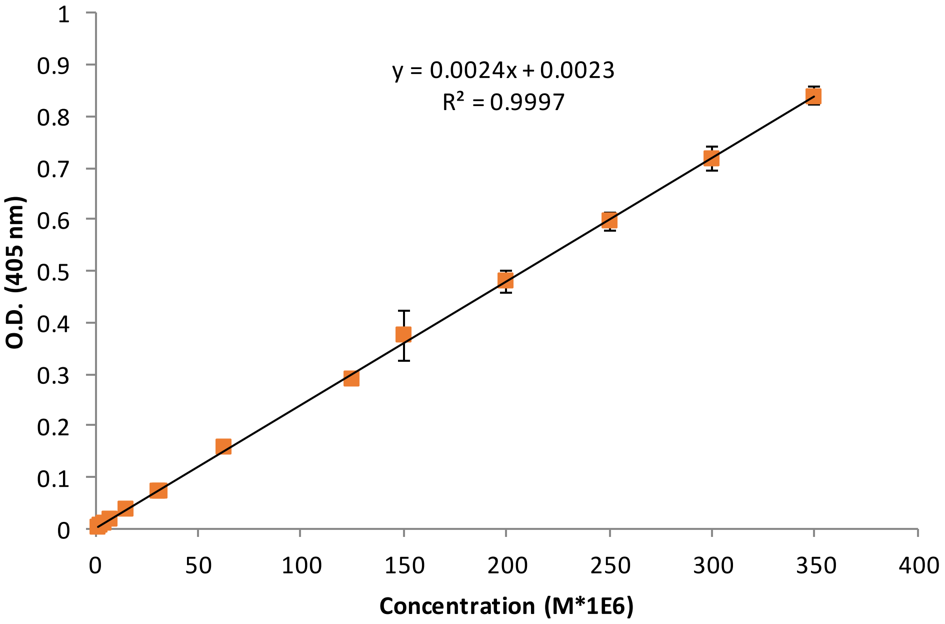

Figure 4.50 - Alizarin Red S standard curve.

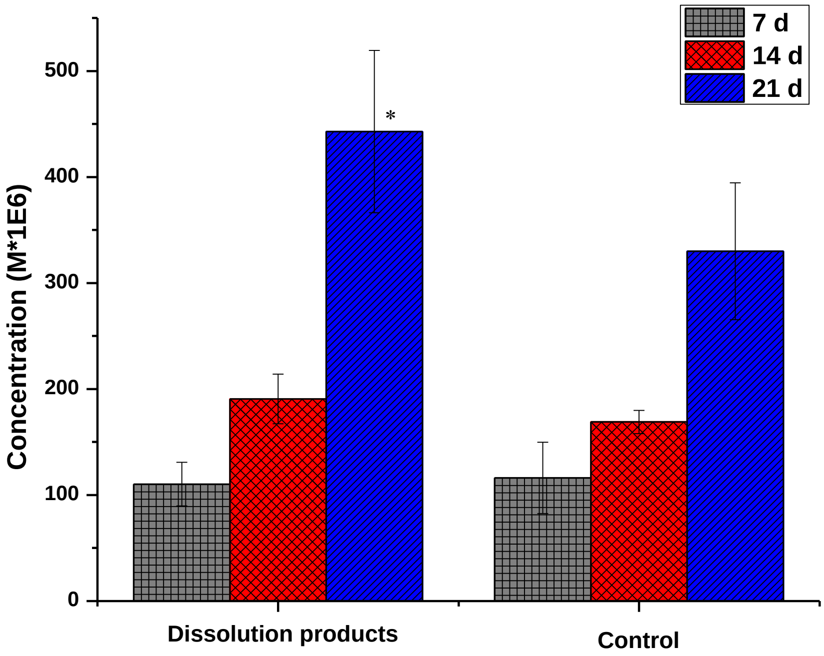

Figure 4.51 - Mineralization of hASCs using Alizarin Red S. Quantification of the calcium content of hASCs for the controls and the dissolution product group on days 7, 14, and 21. ∗ $P < 0.05$ versus control.

4.4.6 Gene expression

Differentiation is a complex process that involves the programmed induction of groups of differentiation specific genes. *In vitro* and *in vivo* differentiation is an intricate multistage cell process, which relies on the coordination of different signalling pathways such as FGFs, BMP and others that are vital for embryogenesis, pluripotency maintenance, cell fate determination, and tissue regeneration (LIU et al., 2009). In spite of this, the mechanisms that control all these cellular processes are not well understood. In this work was assayed the gene expression of 84 genes related to the osteogenesis in its different stages: proliferation, matrix maturation, and mineralization. The analysis was done on day 21, when normally the mineralization process has begun. Among these genes, only genes that exhibited at least reasonably detected gene expression were reported, these factors are recognized to perform essential roles during osteogenesis and are vital during the mineralization process. In general, these genes are related to the BMP signaling pathway, which is part of most cellular processes and is vital for the regulation of cell proliferation, differentiation, apoptosis, migration, and extracellular matrix remodeling (LIU et al., 2009).

For the dissolution product group was observed that among the 67 genes that were expressed, 22 were up-regulated, 25 were down-regulated, and 20 did not show any change with respect to the gene expression of the controls (Table 4.10). Among these, 6 were significantly up-regulated, and 5 were significantly down-regulated. For the scaffold group, among the 70 genes that were expressed, 32 genes were up-regulated, 28 were down-regulated, and 10 did not show any change (Table 4.10). Among these, 12 were significantly up-regulated, and 8 were significantly down-regulated. F18-590.BioS scaffolds showed a higher potential to induce a favorable genetic control in the osteogenic process than the controls and the dissolution product group. This could have occurred because the scaffolds have one more favorable environment that lead hASCs to an easier and faster osteogenic process. F18-590.BioS scaffold is highly porous with interconnected pore networks that facilitate nutrient and oxygen diffusion as well as waste removal, being able to support cell colonization, proliferation, and differentiation of hASCs. This structure can mimic *in vivo* bone environment stimulating cellular differentiation to generate a new bone tissue (CALABRESE et al., 2016). Moreover, the composition of F18 glass and Biosilicate is similar to the inorganic composition of bone; therefore, they are highly bioactive and stimulate the osteogenic process. Additionally, hydrophilic surface increases the cell adhesion getting better the cell spreading over scaffolds (ANSELME et al., 2004; KIESWETTER et al., 1996).

Table 4.10 - Gene expression of hASCs using the osteogenic medium (control group), the dissolution products and the F18-590.BioS scaffolds. Fold regulation values greater than 2 are up-regulated, fold regulation values less than 2 are down-regulated, fold regulation values between 2 and -2 indicate no change. *Measure with P-value < 0.05 is considered statistically significant. - means that the relative expression level is low in both the controls and the test samples.

Symbol	Fold Regulation Ion dissolution	Fold Regulation Scaffolds
Bone matrix proteins		
ALPL	-2.67	-97.98*
BGLAP	-282.82	-178.10
BGN	-	4.43
BMP superfamily		
BMP1	-1.95	28.62*
BMP2	80.87*	125.26*
BMP3	-1.18	-
BMP4	-	42.50
BMP5	33.82	11.55
BMP6	-	1.68
BMP7	1.42	4.65
TGFB1	1.78	5.67
TGFB2	-20.41*	-26.84*
TGFB3	36.74	6.65
Activin receptor		
ACVR1	-78.84	-12.20
Bone morphogenetic protein receptors		
BMPR1A	5.78	-1.23
BMPR1B	-	51.2755*
BMPR2	4.46	1.52
TGF receptors		
TGFBR1	2.07	-2.12
TGFBR2	-1.42	4.01*
Receptors		

CALCR	-187.51*	-256.34*
EGFR	-1.98	-
FGFR1	-2.76	-2.26
FGFR2	-1.33	-2.00
ICAM1	-1.14	-3.82
VCAM1	-	23.18*
VDR	-	2.06
PHEX	-3.23	-4.96
Growth factors		
EGF	-9.53	-18.40*
FGF1	-1.23	-
FGF2	124.84*	-
GDF10	7.28*	-
IGF2	-33.50*	-9.44*
PDGFA	1.37	-2.42
VEGFA	1.03	-1.58
VEGFB	-104.91*	-258.41*
CSF1	-	-2.41
CSF2	-5.43	1.30
CSF3	-3.20	-11.90
Integrin receptors		
ITGA1	5.13	11.32*
ITGA2	51.43	34.90*
ITGA3	-2.88	-3.94
ITGAM	-1.18	33.08
ITGB1	63.74	77.75*
Collagen		
COL10A1	1.01	-18.70
COL14A1	-1.78	-101.89
COL15A1	18.51	-
COL1A1	-1.57	1.09
COL1A2	23.17	76.78

COL3A1	-4.38	2.20
COL5A1	5.04	7.43
Cartilage-related genes		
COMP	2.70*	3.65
SOX9	-2.25	2.98
Metalloproteinases		
MMP10	29.89	34.97
MMP2	9.34	3.65
MMP8	-2.60	-1.79
MMP9	-11.63	-14.13
Transcription factors		
NFKB1	-11.93	-6.60
RUNX2	10.30	50.13
SMAD1	25.02*	9.45*
SMAD2	55.49*	87.07*
SMAD3	-3.19	-3.69
SMAD4	-	14.64
SMAD5	-4.41	-6.93
SP7	-25.44	-12.70
TWIST1	30.81	31.30*
Tumor necrosis factors		
TNF	-	48.52
TNFSF11	-25.09	-221.58
Other genes		
AHSG	17.76	-
ANXA5	-19.71*	-26.30*
CTSK	32.64	22.72
DLX5	-45.99	-351.83
FN1	1.07	14.08
GLI1	-4.49	1.101
IHH	-1.61	-2.27
NOG	-	-3.37*

SERPINH1	-1.30	1.93
SPP1	1.25	13.29*

It has been demonstrated that modifications in the material topography affect osteoblast differentiation using human mesenchymal stromal cells, since topography can affect several mechanisms including modulation of the signaling pathways of distinct growth factors, such as bone morphogenetic proteins (BMPs). Caustro-Raucci *et al.* found that modified surface may upregulate the endogenous expression of BMP2 in osteoblastic cells, which increases the osteogenic potential of the material (CASTRO-RAUCCI et al., 2016). In this work was found that cells passaged over F18-590.BioS scaffolds presented a higher statistically significant up-regulation of BMP2 (Table 4.10) than hASCs cultivated with ionic dissolution products, a factor that contributed to this fact was the topography of the scaffold. BMP2 is part of the major group of bone morphogenetic factors, which modulates diverse mesodermal developmental processes and intervenes in many processes involved in angiogenesis and has showed to be the most osteogenic bone morphogenetic protein, being able to foster bone formation around implants (VLACIC-ZISCHKE et al., 2011). Moreover, it helps in the regulation of postnatal development of mesenchymal skeletal tissues and skeletal repair (HERZOG et al., 2014; MAREDDY et al., 2010). Mareddy *et al.* found that BMP2 can increase bone nodule formation and calcium deposition and when this factor is used together with FGF2, *in vivo* and *in vitro* osteogenesis is stimulated (MAREDDY et al., 2010). As shown above, BMP2 was upregulated for the scaffolds and the dissolution product group, indicating that bone nodule formation and calcium deposition were stimulated in both conditions.

SOX9, RUNX2, and SP7 are the main transcriptional factors of proliferation and differentiation of MSCs into mature osteoblasts. In some studies have been found that RUNX2 exhibits a gradual increment during osteogenic process since this factor is a positive transcriptional regulator of genes such as COL1A1, ALP, and BGLAP, which are vital for matrix maturation and mineralization; moreover, RUNX2 is considered the key transcriptional factor to initiate bone formation (CALABRESE et al., 2016; OLIVEIRA et al., 2012). As can be seen in Table 4.10 RUNX2 was upregulated for both groups, RUNX2 is considering the most important factor during intramembranous ossification, which is the mechanism that leads the osteogenesis when MSCs are cultured *in vitro* using osteogenic medium. This factor is targeted in most of the pathways involved in osteogenesis, activating some genes that are essential for this process such as osteopontin and bone sialoprotein (OLIVEIRA et al., 2012). BMP2 is its major regulator, and during BMP pathway, the complex SMAD-1/5/8 forms a heterotrimeric transcription complex with SMAD4, which travels to the nucleus where it can interact with different factors such as RUNX2 to initiate different processes that encourage bone formation (HAQUE et al., 2008).

In contrast, SP7 or osterix was downregulated for the scaffolds and the dissolution product group. Calabresa *et al.* found that the level of this factor reached a peak of transcriptional activity from day 8 to day 11 and its gene expression diminished during matrix mineralization, being its reduction necessary to foster osteoblast differentiation in the late stage (CALABRESE et al., 2016). This zinc finger transcription factor is expressed for osteoblasts in mice during differentiation process, and in specimens with osterix deficiency were not generated both osteoblasts and bone tissue; moreover, the cartilage-matrix ossification was imperfect (NISHIMURA et al., 2012b; ZHU et al., 2012). Indeed, this factor in human is related to the bone density and RUNX2 regulates its transcription (ZHU et al., 2012). Moreover, this factor is an essential BMP2 specific transcription factor during osteogenesis and is expressed in all developing bones (NAKASHIMA et al., 2002). Additionally, osterix only has an important effect over differentiation if BMP6 signaling is activated (ZHU et al., 2012). As can be seen in Table 4.10, gene expression of BMP6 for the scaffold presented no change in comparison with the control and for the dissolution product group the relative expression level of BMP6 was low.

On the other hand, the gene expression of another class of relevant proteins for osteoblast differentiation was upregulated for the dissolution product group or the scaffolds, or both, especially BMP4, BMP5, SMAD1, SMAD2, and SMAD4. BMP4 is an important factor that regulates osteoblast differentiation through SMAD pathway activation (CANALIS; ECONOMIDES; GAZZERRO, 2003). BMP5 mediates in the regulation of the osteogenic differentiation and in the response that skeleton generates to mechanical stimulates (SHEN et al., 2018). BMPR1A was upregulated for the dissolution product group and for the scaffolds there was no change of BMPR1A expression in comparison with the control; during BMP pathway, the activation of this factor is necessary for the subsequent intracellular cascade inducing osteoblast differentiation (CASTRO-RAUCCI et al., 2016). SMAD3, an inhibitor of osteoblast differentiation, was downregulated by both groups suggesting that the material and dissolution products not only induce osteogenesis but also disrupt cell processes which alter it (OLIVEIRA et al., 2012). Among the genes that were downregulated for both groups, we can mention FGFR1 gene that is upregulated in early osteogenesis because it helps to promote differentiation; nevertheless, FGFR1 signaling in mature osteoblasts causes inhibition of mineralization (LONG, 2012). DLX5, which is an early transcription factor, is expressed before osteogenic commitment (ZAN et al., 2016). Other factor downregulated is MMP9, which is metalloproteinase that participates in angiogenesis and endochondral ossification, being important for alveolar bone formation and remodeling (MINAŘÍKOVÁ et al., 2015).

On the other side, COL1A2, COL15A1, COL3A1, and COL5A1 were upregulated for the scaffolds or the dissolution product group, or both. Collagens perform an important role in cell adhesion; they can induce the release of several growth factors that are necessary for osteoclasts and osteoblasts formation and cell recruitment during osteogenesis. Among them, type I collagen is the most abundant extracellular protein in bone (GRASSI et al., 2016; XUE et al., 2009). Moreover, Biglycan (BGN) was upregulated for the scaffolds; this is an ECM proteoglycan that modulates osteoblast differentiation and matrix mineralization, and BGN knockout mice presented deficient in bone mass (XU et al., 1998). Up-regulation of collagens, FN1, and BGN for the scaffolds indicates that matrix mineralization was favored in scaffolds group compared with the controls (LI; KAWAZOE; CHEN, 2015).

SOX9 is a transcriptional factor that is necessary for chondrocyte differentiation associated with growth factors (FGFs), but in general, the type of ossification *in vitro* is intramembranous ossification. In this type of bone formation is not well understood the function of this factor, although some researchers considered that this marker can be an early key regulator that determines the osteogenic potential of hMSCs (LOEBEL et al., 2014). This factor was upregulated for the scaffolds and downregulated for the dissolution product group.

Among the integrins, ITGA1, ITGA2, and ITGB1 were upregulated in both groups; these molecules are very important in cellular adhesion between the ECM or material surface and cells as well as in cell communication (MINAŘÍKOVÁ et al., 2015). ITGA1 was significantly upregulated in the scaffolds compared with the dissolution product group; this can be explained considering that scaffold surface can stimulate the up-regulation of this integrin. Olivares-Navarrete *et al.* found that human MSCs underwent osteoblastic differentiation on microstructured titanium surfaces, observing that ITGA1 up-regulation increased with the increment of surface roughness. The integrin family is characterized for mediating not only the interaction between cell and biomaterial through cell attachment and roughness recognition but also in osteoblast differentiation (OLIVARES-NAVARRETE et al., 2011). During the last stage of osteogenesis, genes related to cellular adhesion are activated. When the integrins mediate the adhesion between cells and the ECM, this produces cytoskeletal tension changes that induce different mechanochemical signal pathways, which are really important for differentiation (CALABRESE et al., 2016; SHEN et al., 2018).

ALP was downregulated for the scaffolds and the dissolution product group. ALP is one biochemical and histochemical marker used to identify and evaluate osteogenesis. This biomarker is presented in the early stages of osteoblast-mediated mineralization, which is involved in the removal of inorganic pyrophosphate, a potent inhibitor of mineralization. As previously mentioned (section 4.4.4), this enzyme showed the highest concentration on day 14, and then, it began decreasing.

SPP1 is vital for bone formation and can be produced during the whole osteogenic process, reaching a peak at about four weeks (CALABRESE et al., 2016). This factor is secreted into osteocytes, preosteoblasts, and osteoblasts (CALABRESE et al., 2016). The gene expression of SPP1 by cells cultivated using dissolution products had no change compared with control, but SPP1 were upregulated when cells were cultivated over scaffolds.

BGLAP, known as osteocalcin or bone gamma-carboxyglutamic acid-containing protein, is the most common marker when the osteoblasts are totally differentiated; synthesis of this protein is carried out by mature osteoblasts before mineralization (DE GODOY et al., 2015; ZAN et al., 2016). During intramembranous ossification *in vitro*, this factor is downregulated by osteocytes, together with ALP and COL1; by contrast, SPP1 is upregulated (FRANZ-ODENDAAL; HALL; WITTEN, 2006). In this study, BGLAP and ALP was downregulated for both groups and expression of COL1A1, for both groups, did not have any change compared with the controls; moreover, SPP1 was upregulated for scaffolds and no change was observed for the dissolution product group with respect to the control. This tendency can suggest that at 21 days, hASCs have reached the complete maturation of osteoblasts which are responsible for matrix deposition; meanwhile, some of these osteoblasts were embedded in the matrix becoming osteocytes (FRANZ-ODENDAAL; HALL; WITTEN, 2006; RUTKOVSKIY; STENSLØKKEN; VAAGE, 2016). Based on this, it can be concluded that both scaffolds and extracts were able to increase the stimulation of bone formation using osteogenic medium, reaching mineralization at 21 days.

5 CONCLUSIONS

- F18 glass coatings significantly improved the compressive strength of the Biosilicate scaffolds. The combination of Biosilicate glass-ceramic and F18 Bioglass is an interesting option for producing novel scaffolds for bone tissue engineering.
- Overall, F18-590.BioS scaffolds manufactured with a 35% (v/v) Biosilicate slurry and sintered at 900 °C for 180 minutes resulted in an optimal combination of porosity, morphology, mechanical resistance and strut microstructure.
- F18-590.BioS scaffolds are highly interconnected porous structures with cell size larger than 300 μm and porosity higher than 80%, which are essential for cell penetration, tissue ingrowth, new vascularization, and nutrient delivery. Moreover, they possess a compressive strength similar to that of trabecular bone (2-12 MPa), being enough for applications in dentistry in which bones do not bear high loads, such as sinus lifting and vertical augmentation surgeries.
- F18-590.BioS scaffolds have great potential for being used in jaw bone regeneration, presenting the same competitive features of commercial products such as ReproBone™ and Endobon®, with the advantage of being osteoinductive.
- The enzymatic activity of ALP was higher for F18-590.BioS scaffold group than for the controls and the dissolution product group.
- hASCs culture using osteogenic medium with both dissolution products and scaffolds exhibited detectable deposited calcium, and such activity was incremented as the days of differentiation period increased.
- Gene expression of some factors such as BMP2 and RUNX2 showed that osteogenic process is stimulated for both ions released by biomaterial and 3D highly interconnected porous F18-590.BioS scaffolds.
- Down-regulation of BGLAP and ALP together with the up-regulation of SPP1 suggests that hASCs culture using dissolution products and the scaffolds have begun the formation of osteocytes at day 21.

- F18-590.BioS scaffolds were able to upregulate more genes involved in mineralization compared with the dissolution product group and the controls, suggesting their higher potential to induce osteogenic differentiation.
- F18-590.BioS scaffold could be a biomaterial to foster the proliferation and osteogenic differentiation of stem cells and has promising potential for bone tissue engineering and regenerative medicine applications.
- Genes, such as, FGFR1 and TGFB2 that could inhibit mineralization were significantly down-regulation in hASCs grown on the scaffolds. Other studies must be done to determine if the F18-590.BioS scaffolds are more favorable towards matrix development and osteoblast differentiation than other bioactive materials.

6 FUTURE WORK

- One possible way to increase the compressive strength of the scaffolds is to use a 60 ppi foam, whose cell size is smaller; thinner struts of foam reduce the dimension of triangular voids inside the glass-ceramic struts. Moreover, slurries prepared with smaller particles could help to increase the penetration of slurries inside the hollow struts increasing their mechanical integrity. The infiltrations under vacuum generate better results.
- Gene expression can be done for certain specific markers such osteopontin, osteonectin, osteocalcin, and RUNX2 using a calibration curve and specific primers, which would make it possible to determine how their gene expression is changing over time. This can clarify how the osteogenesis is developing during the process.
- Osteogenic process interconnects diverse signalling pathways and the understanding of how the factors communicate among them to control the osteogenesis is vital to create biomaterials with higher osteogenic potential. A more extent genetic study would permit understanding how many signalling pathways are being activated by the scaffolds or theirs ions and how these are communicating.

7 REFERENCES

AKIYAMA, H. et al. The transcription factor Sox9 has essential roles in successive steps of the chondrocyte differentiation pathway and is required for expression of Sox5 and Sox6. **Genes and Development**, v. 16, n. 21, p. 2813-2828, 2002.

ALEXANDER, G. B.; HESTON, W. M.; ILER, R. K. The solubility of amorphous silica in water. **The Journal of Physical Chemistry**, v. 58, n. 6, p. 453-455, 1954.

ANSELME, K. Osteoblast adhesion on biomaterials. **Biomaterials**, v. 21, p. 667-681, 2000.

ANSELME, K. et al. Qualitative and quantitative study of human osteoblast adhesion on materials with various surface roughnesses. **Journal of Biomedical Materials Research**, v. 49, n. 2, p. 155-166, 2004.

ATARI, M. et al. The enhancement of osteogenesis through the use of dental pulp pluripotent stem cells in 3D. **Bone**, v. 50, n. 4, p. 930-941, 2012.

BAGESHLOOYAFSHAR, B. et al. Zinc silicate mineral-coated scaffold improved in vitro osteogenic differentiation of equine adipose-derived mesenchymal stem cells. **Research in Veterinary Science**, v. 124, p. 444-451, 2019.

BAINO, F.; NOVAJRA, G.; VITALE-BROVARONE, C. Bioceramics and scaffolds: a winning combination for tissue engineering. **Frontiers in Bioengineering and Biotechnology**, v. 3, p. 1-17, 2015.

BAINO, F.; VITALE-BROVARONE, C. Three-dimensional glass-derived scaffolds for bone tissue engineering: Current trends and forecasts for the future. **Journal of Biomedical Materials Research - Part A**, v. 97 A, n. 4, p. 514-535, 2011.

BI, L. et al. Effect of bioactive borate glass microstructure on bone regeneration, angiogenesis, and hydroxyapatite conversion in a rat calvarial defect model. **Acta Biomaterialia**, v. 9, n. 8, p. 8015-8026, 2013.

BILOUSOVA, G.; JUN, D.; KING, K. Osteoblasts derived from induced pluripotent stem cells form calcified structures in scaffolds both in vitro and in vivo. **Stem Cells**, p. 206-216, 2011.

BIOMET, Z. **Beta-bsm® Injectable Bone Substitute Material**. Available at:<www.zimmerbiomet.com/medical-professionals/biologics/product/beta-bsm-injectable-bone-substitute-material.html>. Acessed: 7-2019.

BLAIR, H. C. et al. Osteoblast differentiation and bone matrix formation. **Tissue Engineering: Part B**, v. 23, n. 3, p. 268-281, 2017.

BOCCACCINI, A. R. et al. Sintering, crystallisation and biodegradation behaviour of Bioglass®-derived glass-ceramics. **Faraday Discussions**, v. 136, p. 27, 2007.

BOCCACCINI, A. R.; CHEN, Q.; REZWAN, K. **Process for preparing a bioactive glass scaffold.**WO2007017756A2. USA, 2007.

BOCCARDI, E. et al. Study of the mechanical stability and bioactivity of Bioglass® based glass-ceramic scaffolds produced via powder metallurgy-inspired technology. **Biomedical Materials**, v. 11, n. 1, p. 1-11, 2016.

BORN, A. et al. Correlating cell architecture with osteogenesis: first steps towards live single cell monitoring. **European Cells and Materials**, v. 18, p. 49-62, 2009.

BOSE, S.; ROY, M.; BANDYOPADHYAY, A. Recent advances in bone tissue engineering scaffolds. **Trends in Biotechnology**, v. 30, n. 10, p. 546-554, 2012.

BOSSINI, P. S. et al. Biosilicate® and low-level laser therapy improve bone repair in osteoporotic rats. **Journal of Tissue Engineering and Regenerative Medicine**, v. 5, n. 3, p. 229-237, 2011.

CALABRESE, G. et al. Collagen-hydroxyapatite scaffolds induce human adipose derived stem cells osteogenic differentiation in vitro. **Plos One**, v. 11, n. 3, p. 1-17, 2016.

CAMERON, K. et al. Directed osteogenic differentiation of human mesenchymal stem/precursor cells on silicate substituted calcium phosphate. **Journal of Biomedical Materials Research Part A**, v. 101A, p. 13-22, 2012.

CANALIS, E.; ECONOMIDES, A. N.; GAZZERRO, E. Bone morphogenetic proteins, their antagonists, and the skeleton. **Endocrine Reviews**, v. 24, n. 2, p. 218-235, 2003.

CASTRO-RAUCCI, L. M. S. et al. Titanium with nanotopography induces osteoblast differentiation by regulating endogenous bone morphogenetic protein expression and signaling pathway. **Journal of Cellular Biochemistry**, v. 117, p. 1718-1726, 2016.

CERAMISYS. **Reprobon**. Available at:<https://www.ceramisys.com>. Acessed: 8-2019.

CHAN, B. P.; LEONG, K. W. Scaffolding in tissue engineering: general approaches and tissue-specific considerations. **European Spine Journal**, v. 17, n. SUPPL. 4, p. S467-S479, 2008.

CHEN, Q. et al. Fate decision of mesenchymal stem cells: adipocytes or osteoblasts? **Cell Death and Differentiation**, v. 23, p. 1128-1139, 2016.

CHEN, Q. Z. et al. Collagen release kinetics of surface functionalized 45S5 Bioglass®-based porous scaffolds. **Journal of Biomedical Materials Research Part A**, v. 86A, n. 4, p. 987-995, 2007.

CHEN, Q. Z.; THOMPSON, I. D.; BOCCACCINI, A. R. 45S5 Bioglass®-derived glass-ceramic scaffolds for bone tissue engineering. **Biomaterials**, v. 27, n. 11, p. 2414-2425, 2006.

CHIN, L. et al. Recent advances in 3D printing of porous ceramics : a review. **Current Opinion in Solid State & Materials Science**, v. 21, n. 6, p. 323-347, 2017.

CHO, Y. S. et al. A novel technique for scaffold fabrication: SLUP (salt leaching using powder). **Current Applied Physics**, v. 14, n. 3, p. 371-377, 2014.

CHRISTIANSEN, D. L.; HUANG, E. K.; SILVER, F. H. Assembly of type I collagen: fusion of fibril subunits and the influence of fibril diameter on mechanical properties. **Matrix Biology**, v. 19, n. 5, p. 409-420, 2000.

COLLINS, M. N.; BIRKINSHAW, C. Hyaluronic acid based scaffolds for tissue engineering - a review. **Carbohydrate Polymers**, v. 92, n. 2, p. 1262-1279, 2013.

COMESAÑA, R. et al. Toward smart implant synthesis: bonding bioceramics of different resorbability to match bone growth rates. **Scientific Reports**, v. 5, n. 1, p. 1-13, 2015.

COSTA-PINTO, A. R.; REIS, R. L.; NEVES, N. M. Scaffolds based bone tissue engineering: the role of chitosan. **Tissue Engineering Part B: Reviews**, v. 17, n. 5, p. 331-347, 2011.

CROVACE, M. C. et al. Biosilicate® — a multipurpose, highly bioactive glass-ceramic. In vitro, in vivo and clinical trials. **Journal of Non-Crystalline Solids**, v. 432, p. 90-110, 2016.

CUI, N. et al. Preparation, physicochemical properties and biocompatibility of PBLG/PLGA/bioglass composite scaffolds. **Materials Science and Engineering: C**, v. 71, p. 118-124, 2017.

DANKS, A. E.; HALL, S. R.; SCHNEPP, Z. The evolution of “sol-gel” chemistry as a technique for materials synthesis. **Materials Horizons**, v. 3, n. 2, p. 91-112, 2016.

DAROUICHE, R. O. Treatment of infections associated with surgical implants. **New England Journal of Medicine**, v. 350, n. 14, p. 1422-1429, 2004.

DARUS, F. et al. Techniques for fabrication and construction of three-dimensional bioceramic scaffolds: effect on pores size, porosity and compressive strength. **Ceramics International**, v. 44, n. 15, p. 18400-18407, 2018.

DE GODOY, R. F. et al. Silicate-substituted calcium phosphate with enhanced strut porosity stimulates osteogenic differentiation of human mesenchymal stem cells. **Journal of Materials Science: Materials in Medicine**, v. 26, n. 54, p. 1-12, 2015.

DE OLIVEIRA, N. K. et al. Can porous polymeric scaffolds be functionalized by stem cells leading to osteogenic differentiation? A systematic review of in vitro studies. **J Mater Sci (2018)**, v. 53, p. 15757-15768, 2018.

DEPUYSYNTHES. **chronOS® Bone Graft Substitute**. Available at:<https://www.depuysynthes.com/>. Acessed: 5-2019.

DESIMONE, D. et al. Biosilicate®-gelatine bone scaffolds by the foam replica technique: development and characterization. **Science and Technology of Advanced Materials**, v. 14, n. 4, p. 1-11, 2013.

DHANDAYUTHAPANI, B. et al. Polymeric scaffolds in tissue engineering application: a review. **International Journal of Polymer Science**, v. 2011, p. 1-

19, 2011.

DONALD, W.; HEANEY, R. **Remodeling, Growth, And Development Bone resorption and renewal**. Available at:<https://www.britannica.com/science/bone-anatomy/Vascular-supply-and-circulation#ref470935>. Acessed: 3-2019.

DONG, C.; YONGGANG, L. Application of collagen scaffold in tissue engineering: recent advances and new perspectives. **Polimers**, v. 8, n. 42, p. 1-20, 2016.

FERGUSON, C. et al. Does adult fracture repair recapitulate embryonic skeletal formation? **Mechanisms of Development**, v. 87, n. 1-2, p. 57-66, 1999.

FRANZ-ODENDAAL, T. A.; HALL, B. K.; WITTEN, P. E. Buried alive: how osteoblasts become osteocytes. **Developmental Dynamics**, v. 235, n. 1, p. 176-190, 2006.

FU, Q. et al. Toward strong and tough glass and ceramic scaffolds for bone repair. **Advanced Functional Materials**, v. 23, n. 44, p. 5461-5476, 2013.

GABBAI-ARMELIN, P. R. et al. Characterization and biocompatibility of a fibrous glassy scaffold. **Journal of Tissue Engineering and Regenerative Medicine**, v. 11, n. 4, p. 1141-1151, 2017.

GARCIA, M. **Identificación y caracterización de las células madre de la hipófisis**. 233 p. Thesis (Doctorate) - Medicine school: University of Santiago de Compostela, 2012.

GERHARDT, L.; BOCCACCINI, A. R. Bioactive glass and glass-ceramic scaffolds for bone tissue engineering. **Materials**, v. 3, n. 7, p. 3867-3910, 2010.

GHOLIPOURMALEKABADI, M. et al. In vitro and in vivo evaluations of three-dimensional hydroxyapatite/silk fibroin nanocomposite scaffolds. **Biotechnology and Applied Biochemistry**, v. 62, n. 4, p. 441-450, 2015.

GIBSON, L. J.; ASHBY, M. . **Cellular solids: structure and properties.** Cambridge: Cambridge University Press, 1999.

GIL, E. S. et al. Mechanical improvements to reinforced porous silk scaffolds. **Journal of Biomedical Materials Research - Part A**, v. 99 A, n. 1, p. 16-28, 2011.

GINER, M. et al. Differences in osteogenic and apoptotic genes between osteoporotic and osteoarthritic patients. **BMC Musculoskeletal Disorders**, v. 14, n. 41, p. 1-8, 2013.

GOLUB, E. E.; BOESZE-BATTAGLIA, K. The role of alkaline phosphatase in mineralization. **Current Opinion in Orthopaedics**, v. 18, n. 5, p. 444-448, 2007.

GONG, S. et al. Mechanical properties and in vitro biocompatibility of porous zein scaffolds. **Biomaterials**, v. 27, n. 20, p. 3793-3799, 2006.

GORUSTOVICH, A. A.; ROETHER, J. A.; BOCCACCINI, A. R. Effect of bioactive glasses on angiogenesis: a review of in vitro and in vivo evidences. **Tissue Engineering Part B: Reviews**, v. 16, n. 2, p. 199-207, 2010.

GOULART, C.; DE SOUZA, D. Critical analysis of aqueous tape casting, sintering, and characterization of planar Yttria-Stabilized Zirconia electrolytes for SOFC. **International Journal of Applied Ceramic Technology**, v. 14, n. 3, p. 413-423, 2017.

GRANITO, R. N. et al. Effects of biosilicate and bioglass 45S5 on tibial bone consolidation on rats: a biomechanical and a histological study. **Journal of Materials Science: Materials in Medicine**, v. 20, n. 12, p. 2521-2526, 2009.

GRANITO, R. N. et al. In vivo biological performance of a novel highly bioactive glass-ceramic (Biosilicate®): a biomechanical and histomorphometric study in rat tibial defects. **Journal of Biomedical Materials Research Part B: Applied Biomaterials**, v. 97B, n. 1, p. 139-147, 2011.

GRASSI, F. et al. T cell subsets differently regulate osteogenic differentiation of human mesenchymal stromal cells in vitro. **Journal of Tissue Engineering and Regenerative Medicine**, v. 10, p. 305-314, 2016.

GRZESIK, WOJCIECH J, ROBEY, P. G. Bone matrix RGD glycoproteins: immunolocalization bone cells in vitro. **Journal of bone and mineral research**, v. 9, n. 4, p. 487-496, 1994.

HAKKI, S. S.; BOZKURT, S. B.; HAKKI, E. E. Osteogenic differentiation of MC3T3-E1 cells on different titanium surfaces. **Biomedical Materials**, v. 7, p. 1-9, 2012.

HAQUE, T. et al. Characterizing the BMP pathway in a wild type mouse model of distraction osteogenesis. **Bone**, v. 42, p. 1144-1153, 2008.

HENCH, L. L. Third-generation biomedical materials. **science**, v. 295, n. 5557, p. 1014-1017, 2002.

HENCH, L. L. **An introduction to bioceramics.** 2nd. ed. London: Imperial College press, 2013.

HENCH, L. L.; BEST, S. M. Ceramics, glasses, and glass-ceramics: basic Principles. In: **Biomaterials science: an introduction to materials to materials in medicine**. Third ed. London: Elsevier, 2013. p. 128-151.

HERZOG, E. et al. Cell communication in a coculture system consisting of outgrowth endothelial cells and primary osteoblasts. **BioMed Research International**, v. 2014, p. 1-15, 2014.

HOLAND, W.; BEALL, G. Medical and dental glass-ceramics. In: **Glass ceramic technology**. Westerville: The American Ceramic Society, 2002. p. 276.

HOPPE, A. et al. Cobalt-releasing 1393 bioactive glass-derived scaffolds for bone tissue engineering applications. **ACS Applied Materials & Interfaces**, v. 6, n. 4, p. 2865-2877, 2014.

HOPPE, A.; GÜLDAL, N. S.; BOCCACCINI, A. R. A review of the biological response to ionic dissolution products from bioactive glasses and glass-ceramics. **Biomaterials**, v. 32, n. 11, p. 2757-2774, 2011.

HOUSCHYAR, K. et al. Wnt pathway in bone repair and regeneration - what do we know so far. **Frontiers in Cell and Developmental Biology**, v. 6, p. 1-13, 2019.

HURT, A. P. et al. Bioactivity, biocompatibility and antimicrobial properties of a chitosan-mineral composite for periodontal tissue regeneration. **Polimeros-Ciencia E Tecnologia**, v. 25, n. 3, p. 311-316, 2015.

HUSSEIN, K. H. et al. Biocompatibility evaluation of tissue-engineered decellularized scaffolds for biomedical application. **Materials Science and Engineering C**, v. 67, p. 766-778, 2016.

JANEBODIN, K. et al. Isolation and characterization of neural crest-derived stem cells from dental pulp of neonatal mice. **Plos One**, v. 6, n. 11, p. 2-21, 2011.

JAYAKUMAR, R. et al. Biomedical applications of chitin and chitosan based nanomaterials - a short review. **Carbohydrate Polymers**, v. 82, n. 2, p. 227-232, 2010.

JIANG, W. et al. Purification of biosilica from living diatoms by a two-step acid cleaning and baking method. **Journal of Applied Phycology**, v. 26, n. 3, p. 1511-1518, 2014.

JODATI, H.; BENGI, Y.; EVIS, Z. A review of bioceramic porous scaffolds for hard tissue applications : effects of structural features. **Ceramics International**, v. 46, p. 15725-15739, 2020.

JOHNELL, O.; KANIS, J. A. An estimate of the worldwide prevalence, mortality and disability associated with hip fracture. **Osteoporosis International**, v. 15, n. 11, p. 897-902, 2004.

JONES, J. R.; GENTLEMAN, E.; POLAK, J. Bioactive glass scaffolds for bone regeneration. **Elements**, v. 3, n. 6, p. 393-399, 2007.

JUKES, J. M. et al. Endochondral bone tissue engineering using embryonic stem cells. **Proceedings of the National Academy of Sciences**, v. 105, n. 19, p. 6840-6845, 2008.

KAARTINEN, M. T. et al. Tissue transglutaminase and its substrates in bone. **Journal of Bone and Mineral Research**, v. 17, n. 12, p. 2161-2173, 2002.

KARAGEORGIOU, V.; KAPLAN, D. Porosity of 3D biomaterial scaffolds and osteogenesis. **Biomaterials**, v. 26, n. 27, p. 5474-5491, 2005.

KARGOZAR, S. et al. Bone tissue engineering using human cells: a comprehensive review on recent trends, current prospects, and recommendations. **Applied Sciences**, v. 9, n. 1, p. 174, 2019.

KARSENTY, G.; KRONENBERG, H. M.; SETTEMBRE, C. Genetic control of bone formation. **Annual Review of Cell and Developmental Biology**, v. 25, n. 1, p. 629-648, 2009.

KHALILI, A. A.; AHMAD, M. R. A Review of cell adhesion studies for biomedical and biological applications. **International Journal of Molecular Sciences**, v. 16, n. 8, p. 18149-18184, 2015.

KIDO, H. W. et al. Histopathological, cytotoxicity and genotoxicity evaluation of Biosilicate® glass-ceramic scaffolds. **Journal of Biomedical Materials Research - Part A**, v. 101 A, n. 3, p. 667-673, 2013.

KIESWETTER, K. et al. Surface roughness modulates the local production of growth factors and cytokines by osteoblast-like MG-63 cells. **Journal of Biomedical Materials Research**, v. 32, n. 1, p. 55-63, 1996.

KIM, J. et al. Comparable efficacy of silk fibroin with the collagen membranes for guided bone regeneration in rat calvarial defects. **The Journal of Advanced Prosthodontics**, v. 6, p. 539-546, 2014.

KNAUSS, K. G.; WOLERY, T. J. The dissolution kinetics of quartz as a function of pH and time at 70°C. **Geochimica et Cosmochimica Acta**, v. 52, n. 1, p. 43-53, 1988.

KNOTT, L.; BAILEY, A. J. Collagen cross-links in mineralizing tissues: a review of their chemistry, function, and clinical relevance. **Bone**, v. 22, n. 3, p. 181-187, 1998.

KNOWLES, J. C. Phosphate based glasses for biomedical applications. **Journal of Materials Chemistry**, v. 13, n. 10, p. 2395-2401, 2003.

KOKABU, S. et al. BMP3 suppresses osteoblast differentiation of bone marrow stromal cells via interaction with Acvr2b. **Molecular Endocrinology**, v. 26, n. 1, p. 87-94, 2012.

KOMAROVA, S. et al. Mathematical model for bone mineralization. **Frontiers in Cell and Developmental Biology**, v. 3, p. 1-11, 2015.

KRETLOW, J. D.; MIKOS, A. G. Review: Mineralization of synthetic polymer scaffolds for bone tissue engineering. **Tissue Engineering**, v. 13, n. 5, p. 927-938, 2007.

KULTERER, B. et al. Gene expression profiling of human mesenchymal stem cells derived from bone marrow during expansion and osteoblast differentiation. **BMC Genomics**, v. 8, n. 1, p. 70, 2007.

KUMAR, N.; GILULA, N. The gap junction communication channel. **Cell**, v. 84, p. 381-388, 1996.

KURIEN, T.; PEARSON, R. G.; SCAMMELL, B. E. Bone graft substitutes currently available in orthopaedic practice: the evidence for their use. **The Bone & Joint Journal**, v. 95B, n. 5, p. 583-597, 2013.

LARROUTURE, Q. C. et al. Chloride - hydrogen antiporters ClC-3 and ClC-5 drive osteoblast mineralization and regulate fine-structure bone patterning in vitro. **Physiological Reports**, v. 3, n. 11, p. e12607-e12607, 2015.

LATTANZI, W.; BERNARDINI, C. Genes and molecular pathways of the osteogenic process. In: **Osteogenesis**. Rome: IntechOpen, 2011. p. 1-20.

LI, J.; KAWAZOE, N.; CHEN, G. Gold nanoparticles with different charge and moiety induce differential cell response on mesenchymal stem cell osteogenesis. **Biomaterials**, v. 54, p. 226-236, 2015.

LINDEN, E.; CRAIG. Bones and joints. In: **Jubb, Kennedy and Palmer's pathology of domestic Animals**. 5th. ed. Edinburgh: Elsevier Saunders, 2007. p. 220.

LIU, L. et al. Stem cell regulatory gene expression in human adult dental pulp and periodontal ligament cells undergoing odontogenic/osteogenic differentiation. **Journal of Endodonotics**, v. 35, n. 10, p. 1368-1376, 2009.

LIU, X.; RAHAMAN, M. N.; FU, Q. Bone regeneration in strong porous bioactive glass (13-93) scaffolds with an oriented microstructure implanted in rat calvarial defects. **Acta Biomaterialia**, v. 9, n. 1, p. 4889-4898, 2013.

LIU, Y.; LIM, J.; TEOH, S. H. Review: development of clinically relevant scaffolds for vascularised bone tissue engineering. **Biotechnology Advances**, v. 31, n. 5, p. 688-705, 2013.

LO, B.; PARHAM, L. Ethical issues in stem cell research. **Endocrine Reviews**, v. 30, n. 3, p. 204-213, 2009.

LOEBEL, C. et al. In vitro osteogenic potential of human mesenchymal stem cells is predicted by Runx2/Sox9 ratio. **Tissue Engineering Part A**, v. 21, n. 1-2, p. 115-123, 2014.

LONG, F. Building strong bones: molecular regulation of the osteoblast lineage. **Nature Reviews Molecular Cell Biology**, v. 13, n. 1, p. 27-38, 2012.

LONG, T. et al. Fabrication of three-dimensional porous scaffold based on collagen fiber and bioglass for bone tissue engineering. **Journal of Biomedical Materials Research Part B: Applied Biomaterials**, v. 103, n. 7, p. 1455-1464, 2015.

LOPES, D. et al. Bone physiology as inspiration for tissue regenerative therapies. **Biomaterials**, v. 185, p. 240-275, 2018.

MAHDAVI, F. S. et al. Bioactive glass ceramic nanoparticles-coated poly(L-lactic acid) scaffold improved osteogenic differentiation of adipose stem cells in equine. **Tissue and Cell**, v. 49, n. 5, p. 565-572, 2017.

MAJI, K. et al. Preparation and evaluation of gelatin-chitosan-nanobioglass 3D porous scaffold for bone tissue engineering. **International Journal of Biomaterials**, v. 2016, p. 1-14, 2016.

MAO, X. Recent advances in porous ceramics. In: **Processing of ceramic foams**. Kuala Lumpur: Intechopen, 2017. p. 8-10.

MAREDDY, S. et al. Stem cell-related gene expression in clonal populations. **Tissue engineering. Part A**, v. 16, n. 2, p. 749-759, 2010.

MARSELL, R.; EINHORN, T. A. The biology of fracture healing. **Injury**, v. 42, n. 6, p. 551-555, 2011.

MARTINS, C. H. G. et al. Assessment of antimicrobial effect of Biosilicate® against anaerobic, microaerophilic and facultative anaerobic microorganisms. **Journal of Materials Science: Materials in Medicine**, v. 22, n. 6, p. 1439-1446, 2011.

MATASSI, F. et al. New biomaterials for bone regeneration. **Clinical Cases in Mineral and Bone Metabolism**, v. 8, n. 1, p. 21-24, 2011.

MEHRABANIAN, M.; NASR-ESFAHANI, M. HA/nylon 6,6 porous scaffolds fabricated by salt-leaching/solvent casting technique: effect of nano-sized filler content on scaffold properties. **International journal of nanomedicine**, v. 6, p. 1651-1659, 2011.

MELLI, V. et al. Resorbability of a Bioglass®-based glass-ceramic scaffold produced via a powder metallurgy approach. **Ceramics International**, v. 43, p. 8625-8635, 2017.

MESQUITA-GUIMARÃES, J. et al. Evaluation of in vitro properties of 3D micro-macro porous zirconia scaffolds coated with 58S bioactive glass using MG-63 osteoblast-like cells. **Journal of the European Ceramic Society**, v. 39, n. 7, p. 2545-2558, 2019.

MIGLIARESI, C.; MOTTA, A.; DIBENEDETTO, A. T. Injectable scaffolds for bone and cartilage regeneration. In: **Engineering of functional skeletal**

tissues. Third ed. London: Springer, 2018. p. 97-100.

MILLIPORE, C. **Osteogenesis Assay Kit**. Available at:<http://www.merckmillipore.com/BR/pt/product/Osteogenesis-Quantitation-Kit,MM_NF-ECM815#anchor_UG>. Acessed: 3-2019.

MINAŘÍKOVÁ, M. et al. Osteogenic profile of mesenchymal cell populations contributing to alveolar bone formation. **Cells Tissues Organs**, v. 200, p. 339-348, 2015.

MIRON, R. J.; ZHANG, Y. F. Osteoinduction: a review of old concepts with new standards. **Journal of Dental Research**, v. 91, n. 8, p. 736-744, 2012.

MITRA, J. et al. Scaffolds for bone tissue engineering: role of surface patterning on osteoblast response. **RSC Advances**, v. 3, n. 28, p. 11073-11094, 2013.

MORI-AKIYAMA, Y. et al. Sox9 is required for determination of the chondrogenic cell lineage in the cranial neural crest. **Proceedings of the National Academy of Sciences**, v. 100, n. 16, p. 9360-9365, 2003.

NAKASHIMA, K. et al. The novel zinc finger-containing transcription factor osterix is required for osteoblast differentiation and bone formation. **Cell**, v. 108, p. 17-29, 2002.

NASERI, S. et al. Fabrication and characterization of zein-bioactive glass scaffolds. **Bioinspired, Biomimetic and Nanobiomaterials**, v. 4, n. 1, p. 73-78, 2015.

NAVARRO, M. et al. New macroporous calcium phosphate glass ceramic for guided bone regeneration. **Biomaterials**, v. 25, n. 18, p. 4233-4241, 2004.

NISHIMURA, R. et al. Regulation of bone and cartilage development by network between BMP signalling and transcription factors. **JB Review**, v. 151, n. 3, p. 247-254, 2012a.

NISHIMURA, R. et al. Osterix regulates calcification and degradation of chondrogenic matrices through matrix metalloproteinase 13 (MMP13) expression in association with transcription factor Runx2 during endochondral ossification. **Journal of Biological Chemistry**, v. 287, n. 40, p. 33179-33190, 2012b.

NORIAN, I. **Norian SRS Rotary Mix: calcium phosphate bone void**

filler. Available at:<https://www.slideshare.net/MichelleLapus/norian-srs-rotary-mix-64500080>. Acessed: 5-2019.

NOROWSKI, P. A.; BUMGARDNER, J. D. Biomaterial and antibiotic strategies for peri-implantitis: a review. **Journal of Biomedical Materials Research Part B: Applied Biomaterials**, v. 88B, n. 2, p. 530-543, 2009.

OLIVARES-NAVARRETE, R. et al. Mediation of osteogenic differentiation of human mesenchymal stem cells on titanium surfaces by a Wnt-integrin feedback loop. **Biomaterials**, v. 32, n. 27, p. 6399-6411, 2011.

OLIVEIRA, F. S. et al. Hedgehog signaling and osteoblast gene expression are regulated by purmorphamine in human mesenchymal stem. **Journal of Cellular Biochemistry**, v. 113, p. 204-208, 2012.

ORIMO, H. The mechanism of mineralization and the role of alkaline phosphatase in health and disease. **Journal of Nippon Medical School**, v. 77, n. 1, p. 4-12, 2010.

ORTEGA, F. S.; SEPULVEDA, P.; PANDOLFELLI, V. C. Monomer systems for the gelcasting of foams. **Journal of the European Ceramic Society**, v. 22, p. 1395-1401, 2002.

PARK, H. J. et al. Fabrication of microporous three-dimensional scaffolds from silk fibroin for tissue engineering. **Macromolecular Research**, v. 22, n. 6, p. 592-599, 2014.

PARK, J. S. et al. Biodegradable polycaprolactone/cuttlebone scaffold composite using salt leaching process. **Korean Journal of Chemical Engineering**, v. 29, n. 7, p. 931-934, 2012.

PATEL, M.; FISHER, J. P. Biodegradable materials for tissue engineering. In: **Research Reviews**. 6. ed. Surat: McGraw-Hill, 2008. p. 80.

PEITL, O.; DUTRA ZANOTTO, E.; HENCH, L. L. Highly bioactive P2O5-Na2O-CaO-SiO2 glass-ceramics. **Journal of Non-Crystalline Solids**, v. 292, n. 1-3, p. 115-126, 2001.

PEITL, O.; LATORRE, G. P.; HENCH, L. L. Effect of crystallization on apatite layer formation of bioactive glass 45S5. **Journal of Biomedical Materials Research**, v. 30, p. 509-514, 1996.

PESCE, V. et al. Surgical approach to bone healing in osteoporosis.

Clinical Cases in Mineral and Bone Metabolism, v. 6, n. 2, p. 131-135, 2009.

PHILIP, L. Membrane Receptors. In: **The membranes of cells**. 3rd. ed. New York: Academic Press, 2016. p. 15.

PROSECKÁ, E. et al. Collagen/hydroxyapatite scaffold enriched with polycaprolactone nanofibers, thrombocyte-rich solution and mesenchymal stem cells promotes regeneration in large bone defect in vivo. **Journal of Biomedical Materials Research - Part A**, v. 103, n. 2, p. 671-682, 2015.

RAHAMAN, M.; DAY, D. E.; BAL, B. Bioactive glass in tissue engineering. **Acta Biomaterialia**, v. 7, n. 6, p. 2355-2373, 2011.

RAHMAN, S. et al. TGF-b/BMP signaling and other molecular events : regulation of osteoblastogenesis and bone formation. **Bone Research**, v. 3, p. 1-20, 2015.

RAMEZANIFARD, R. et al. Biomimetic scaffolds containing nanofibers coated with willemite nanoparticles for improvement of stem cell osteogenesis. **Materials Science and Engineering C**, v. 62, p. 398-406, 2016.

RENNO, A. C. M. et al. Characterization and in vivo biological performance of biosilicate. **BioMed Research International**, v. 2013, p. 1-7, 2013.

ROBINSON, M. et al. Optimizing differentiation protocols for producing dopaminergic neurons from human induced pluripotent stem cells for tissue engineering applications. **Acta Biomaterialia**, v. 4, p. 61-70, 2015.

ROHANOVÁ, D. et al. TRIS buffer in simulated body fluid distorts the assessment of glass-ceramic scaffold bioactivity. **Acta Biomaterialia**, v. 7, n. 6, p. 2623-2630, 2011.

ROSS, E. A. et al. Tissue adhesion to bioactive glass-coated silicone tubing in a rat model of peritoneal dialysis catheters and catheter tunnels. **Kidney International**, v. 63, p. 702-708, 2003.

RUTKOVSKIY, A.; STENSLØKKEN, K.-O.; VAAGE, I. J. Osteoblast differentiation at a glance. **Medical Science Monitor Basic Research**, v. 22, p. 95-106, 2016.

RYSHKEWITCH, E. Compression strength of porous sintered Alumina and Zirconia. **Journal of the American Ceramic Society**, v. 36, n. 2, p. 65-68, 1953.

SABIR, M. I.; XU, X.; LI, L. A review on biodegradable polymeric materials for bone tissue engineering applications. **Journal of Materials Science**, v. 44, n. 21, p. 5713-5724, 2009.

SCIENCELL. **Alizarin Red S Staining Quantification Assay**. Available at:<https://www.sciencellonline.com/PS/8678.pdf>. Acessed: 1-2019.

SCOTT, G. **Developmental biology**. 6th. ed. Sunderland: Sinauer Associates, 2000.

SELIMOVIĆ, Š. et al. Microfluidic systems for controlling stem cells microenvironments. In: **Microfluidic cell culture systems**. 1th. ed. Oxford: William Andrew, 2013. p. 192.

SHEN, Y. et al. The effect of β-aminopropionitrile on skeletal micromorphology and osteogenesis. **Calcified Tissue International**, v. 103, n. 4, p. 411-421, 2018.

SHU, X. et al. Combined delivery of bone morphogenetic protein-2 and insulin-like growth factor-1 from nano-poly(γ-glutamic acid)/β-tricalcium phosphate-based calcium phosphate cement and its effect on bone regeneration in vitro. **Journal of Biomaterials Applications**, v. 32, n. 5, p. 547-560, 2017.

SIFONTES, A. et al. Preparation of γ-alumina foams of high surface area employing the polyurethane sponge replica method. **Latin American Applied Research**, v. 40, n. 2, p. 185-191, 2010.

SIGMA. **Product information: SIGMAFAST BCIP/NBT tablet**. Available at:<www.sigmaaldrich.com/content/dam/sigma-aldrich/docs/Sigma/Datasheet/b5655dat.pdf>. Acessed: 4-2020a.

SIGMA. **Colorimetric Alkaline Phosphatase and Peroxidase Substrate Detection Systems**. Available at:<www.sigmaaldrich.com/technical-documents/articles/biofiles/colorimetric-alkaline.html>. Acessed: 3-2019b.

ŚMIESZEK, A. et al. Enhanced cytocompatibility and osteoinductive properties of sol-gel-derived silica/zirconium dioxide coatings by metformin functionalization. **Journal of Biomaterials Applications**, v. 32, n. 5, p. 570-586, 2017.

SOUTO, R. et al. Prevalence of “non-oral” pathogenic bacteria in subgingival biofilm of subjects with chronic periodontitis. **Brazilian Journal of Microbiology**, v. 37, n. 3, p. 208-215, 2006.

SOUZA, M. **Desenvolvimento e caracterização de tecidos vítreos flexíveis altamente bioativos**. 227 p. Thesis (doctorate). Materials Science and Engineering: Federal University of São Carlos, 2015.

SOUZA, M. T. et al. New highly bioactive crystallization-resistant glass for tissue engineering applications. **Translational Materials Research**, v. 4, n. 1, p. 7-10, 2017.

STAINS, J. P.; CIVITELLI, R. Cell-cell interactions in regulating osteogenesis and osteoblast function. **Birth Defects Research Part C**, v. 75, n. 1, p. 72-80, 2005.

STEVENS, B. et al. A review of materials, fabrication methods, and strategies used to enhance bone regeneration in engineered bone tissues. **Journal of Biomedical Materials Research - Part B Applied Biomaterials**, v. 85, n. 2, p. 573-582, 2008.

TAHERKHANI, S.; MOZTARZADEH, F. Fabrication of a poly(ε-caprolactone)/starch nanocomposite scaffold with a solvent-casting/salt-leaching technique for bone tissue engineering applications. **Journal of Applied Polymer Science**, v. 133, n. 23, p. 19-21, 2016.

THEOCHARIS, A. D. et al. Extracellular matrix structure. **Advanced Drug Delivery Reviews**, v. 97, p. 4-27, 2016.

THOMPSON, E. et al. Recapitulating endochondral ossification: a promising route to in vivo bone regeneration. **Journal of Tissue Engineering and Regenerative Medicine**, v. 9, p. 889-902, 2015.

TIAINEN, H.; WIEDMER, D.; HAUGEN, H. J. Processing of highly porous TiO2 bone scaffolds with improved compressive strength. **Journal of the European Ceramic Society**, v. 33, n. 1, p. 15-24, 2013.

TILOCCA, A. Structural models of bioactive glasses from molecular dynamics simulations. **Procedings of the Royal Society A**, v. 465, p. 1003-1027, 2009.

TORTELLI, F. et al. The development of tissue-engineered bone of different origin through endochondral and intramembranous ossification following the implantation of mesenchymal stem cells and osteoblasts in a murine model. **Biomaterials**, v. 31, n. 2, p. 242-249, 2010.

VATS, A. et al. Scaffolds and biomaterials for tissue engineering: a review of clinical applications. **Clinical Otolaryngology and Allied Sciences**, v. 28, n. 3, p. 165-172, 2003.

VLACIC-ZISCHKE, J. et al. The influence of surface microroughness and hydrophilicity of titanium on the up-regulation of TGFb/BMP signalling in osteoblasts . **Biomaterials**, v. 32, p. 665-671, 2011.

WANG, X.; RUAN, J. M.; CHEN, Q. Y. Effects of surfactants on the microstructure of porous ceramic scaffolds fabricated by foaming for bone tissue engineering. **Materials Research Bulletin**, v. 44, n. 6, p. 1275-1279, 2009.

WANG, Y. K.; CHEN, C. S. Cell adhesion and mechanical stimulation in the regulation of mesenchymal stem cell differentiation. **Journal of Cellular and Molecular Medicine**, v. 17, n. 7, p. 823-832, 2013.

WANG, Z. et al. Analysis of factors influencing bone ingrowth into three-dimensional printed porous metal scaffolds : a review. **Journal of Alloys and Compounds**, v. 717, p. 271-285, 2017.

WANPENG, C.; HENCH, L. L. Bioactive materials. **Ceramics International**, v. 22, p. 493-507, 1996.

WIEDING, J.; JONITZ, A.; BADER, R. The effect of structural design on mechanical properties and cellular response of additive manufactured titanium scaffolds. **Materials**, v. 5, n. 8, p. 1336-1347, 2012.

WILLERTH, S. M. Neural tissue engineering using embryonic and induced pluripotent stem cells. **Stem Cell Research & Therapy**, v. 2, n. 17, p. 1-9, 2011.

WU, C. et al. Structure-property relationships of silk-modified mesoporous bioglass scaffolds. **Biomaterials**, v. 31, n. 13, p. 3429-3438, 2010.

WU, C.; LU, H. Smad signal pathway in BMP-2-induced osteogenesis－a mini review. **Journal of Dental Sciences**, v. 3, n. 250, p. 13-21, 2008.

WU, S. et al. Biomimetic porous scaffolds for bone tissue engineering.

Materials Science and Engineering: R, v. 80, p. 1-36, 2014.

XU, T. et al. Targeted disruption of the biglycan gene leads to an osteoporosis-like phenotype in mice. **Nature Genetics**, v. 20, p. 78-82, 1998.

XUE, Y. et al. Endothelial cells influence the osteogenic potential of bone marrow stromal cells. **Biomedical Engineering Online**, v. 8, p. 1-9, 2009.

XYNOS, I. D. et al. Bioglass ®45S5 stimulates osteoblast turnover and enhances bone formation in vitro: implications and applications for bone tissue engineering. **Calcified Tissue International**, v. 67, n. 4, p. 321-329, 2000.

XYNOS, I. D. et al. Gene-expression profiling of human osteoblasts following treatment with the ionic products of Bioglass 45S5 dissolution. **Journal of Biomedical Materials Research**, v. 55, n. 2, p. 151-157, 2001.

YANG, G. et al. Counterionic biopolymers-reinforced bioactive glass scaffolds with improved mechanical properties in wet state. **Materials Letters**, v. 75, p. 80-83, 2012.

YANG, X. et al. The stimulatory effect of silica nanoparticles on osteogenic differentiation of human mesenchymal stem cells. **Biomedical Materials**, v. 12, p. 1-11, 2017.

YANG, X. et al. Incorporation of silica nanoparticles to PLGA electrospun fibers for osteogenic differentiation of human osteoblast-like cells. **Regenerative Biomaterials**, p. 229-238, 2018.

YU, J. et al. Zinc-modified calcium silicate coatings promote osteogenic differentiation through TGF-β/Smad pathway and osseointegration in osteopenic rabbits. **Scientific Reports**, v. 7, p. 1-13, 2017.

YUAN, H. et al. Bone induction by porous glass ceramic made from Bioglass (45S5). **Journal of Biomedical Materials Research**, v. 58, n. 3, p. 270-276, 2001.

YUN, H.; KIM, S.; PARK, E. K. Bioactive glass-poly (ε-caprolactone) composite scaffolds with 3 dimensionally hierarchical pore networks. **Materials Science and Engineering: C**, v. 31, n. 2, p. 198-205, 2011.

YUNOS, M. D.; BRETCANU, O.; BOCCACCINI, A. R. Polymer-bioceramic composites for tissue engineering scaffolds. **Journal of Materials Science**, v. 43, n. 13, p. 4433-4442, 2008.

YUSOP, A. H. et al. Porous biodegradable metals for hard tissue scaffolds: a review. **International Journal of Biomaterials**, v. 2012, p. 1-10, 2012.

ZAN, X. et al. Effect of roughness on in situ biomineralized CaP-Collagen coating on the osteogenesis of mesenchymal stem cells. **Langmuir**, v. 32, p. 1808-1817, 2016.

ZHAI, W. et al. Stimulatory effects of the ionic products from Ca-Mg-Si bioceramics on both osteogenesis and angiogenesis in vitro. **Acta Biomaterialia**, v. 9, n. 8, p. 8004-8014, 2013.

ZHU, F. et al. The transcription factor osterix (SP7) regulates BMP6-induced human osteoblast differentiation. **Journal of Cellular Physiology**, v. 227, n. 6, p. 2677-2685, 2012.

ZIMMERBIOMET. **βBeta-bsm®**. Available at:<https://www.zimmerbiometdental.com>. Acessed: 3-2019.

ZOHORA, F. T.; YOUSUF, A.; ANWARUL, M. Biomaterials as porous scaffolds for tissue engineering applications: a review. **European Scientific Journal**, v. 10, n. 21, p. 186-209, 2014.

ZUK, P. et al. Multilineage cells from human adipose tissue: implications for cell-based therapies. **Tissue Engineering**, v. 7, n. 2, p. 211-228, 2001.

ANNEXES

ANNEX A: deflocculation curves

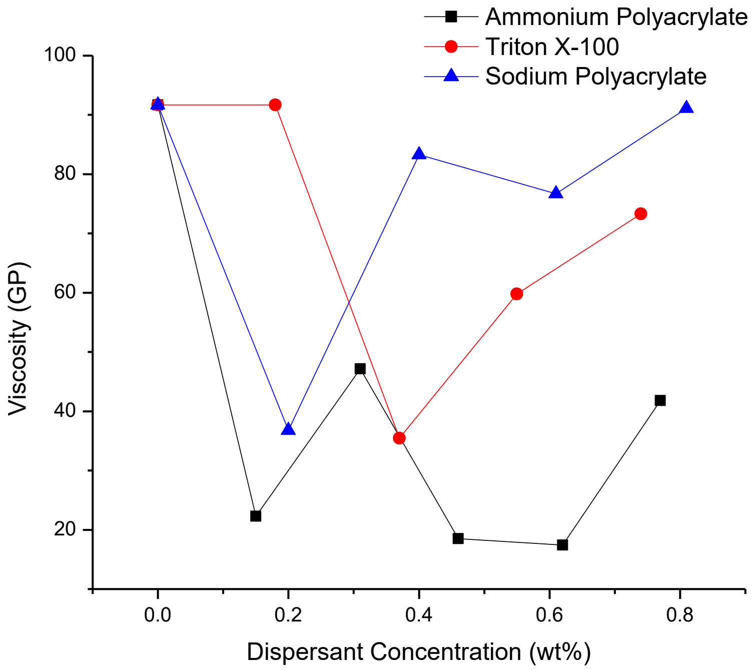

Figure 1 - Deflocculation curves for 30% (v/v) Biosilicate slurry without PVB.

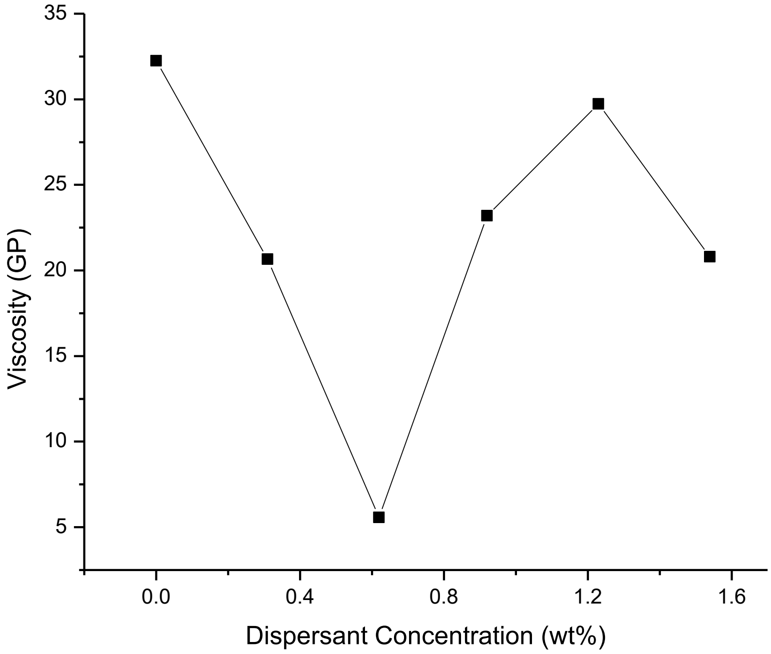

Figure 2 - Deflocculation curve for 30% (v/v) F18 slurry without PVB using ammonium polyacrylate.

ANNEX B: immunohistochemistry

Day one

1. Old medium was removed and each well was washed with 1 mL (PBS pH 7.4).
2. 600 µL of 3.7% formaldehyde (formalin) was added to each well to fix cells.
3. Cells were fixed for one hour at room temperature.
4. Formalin was removed after one hour and rinsed with 1 mL of PBS.
5. Cells were permeabilized by adding 0.1% Triton-X:
    - 500 µL of 0.1% Triton-X was added to each well.
    - Plate was incubated at room temperature for 45 minutes.
6. Meanwhile, NGS was thawed in warm water bath.
7. Wells were blocked with 5% NGS.
    - It was mixed 2.5 mL NGS in 50 mL PBS to get one 5% solution.
    - It was added 600 µL to each well and incubated at room temperature for two hours.
8. It was added primary antibody vimentin (Rb mAb to Vimentin (abcam)):
    - It was diluted (2400/500) 4.8 µL of vimentin in 24 mL of PBS.
    - 800 µL of primary antibody solution was added to each well.
    - Plate was incubated at 4 ˚C overnight.

Second day

9. Wells were washed three times with 0.5 mL of PBS to each well.
10. Plate was incubated in fridge for 15 minutes after each wash.
11. Apply secondary antibody Alexa fluor TM 568 goat anti-Rabbit (Invitrogen).
    - It was added 800 µL of secondary solution to each well
    - Plate was wrapped with foil and incubated for 4 hours at room temperature.
12. Each well was washed with PBS three times for 15 minutes and took photos.
13. After this procedure was done other antibody over the same wells that had been used before:

- In a tube was put 3 mL of PBS and was added 6.3 µL of DAPI to get a concentration of 50µl/mL and added to each well.
- The plate was incubated for 5 minutes, washed and took photos.

ANNEX C: culture of fibroblasts over scaffolds

1. Vial with fibroblasts type PCS-201-012 was thawed at room temperature. It was used one vial to passage in four wells of 24-well plate (controls and scaffolds).
2. Content of vial (1 mL) was put in a 15 mL tube and added 8 mL of DMEM.
3. Tube was centrifuged for 5 minutes at 300 x g and discarded the supernatant.
4. It was added 6 mL of AM medium (High Glucose DMEM with glutamine, 10% FBS, and 1% Pen/Strep) in the tube and mixed.
5. It was put 1 mL of cells in each well with scaffolds and 0.5 mL in controls and incubated at 37 °C.
6. Change medium was done every three days until complete confluence.

ANNEX D: determination of cell live and died

After two days in osteogenic media, hASCs cultured with F18 glass-coated Biosilicate scaffolds were detached and resuspended with PBS. Then, cell suspensions based on the Table 1 was done. After incubation, lectures were done with flow cytometer.

Table 1 - Cell suspensions with ViaCount™ Reagent.

Original cell suspension Cell/mL	Cell suspension Volume (µL)	ViaCount™ Reagent Volume (µL)
$1 \times 10^5 - 1 \times 10^6$	50	450
$1 \times 10^6 - 1 \times 10^7$	20	380
$1 \times 10^7 - 1 \times 10^8$	20	780

ANNEX E: synthesis of F18-BioS scaffolds

The Biosilicate® scaffolds were manufactured by a method based on the addition of a porogen agent. This method was described with details in a previous work (KIDO et al., 2013). This method is, therefore, shortly described: initially, 100 mL of a suspension containing 67% vol. of isopropyl alcohol anhydrous (QHEMIS), 3% vol. of polyvinyl butyral (Butvar B-98), 24% vol. of carbon black (CABOT BP-120), and 6% vol. of Biosilicate®, was prepared. Then isopropyl alcohol, PVB, and Biosilicate® were mixed in an agate jar and milled in a planetary ball mill (Pulverisette6-FRITSCH) at 550 rpm for 1 h. The agate spheres were removed from the suspension, and the pre-sieved carbon black spheres (300-600 µm) were added and then mixed for 5 minutes at 150 rpm. The suspension was poured into a plastic container and dried with a heat gun (DEKEL DK1210). The resulting granulated powder was pressed in two steps, the first uniaxial using a cylindrical steel mold, and the second isostatic. Finally, the cylindrical samples were heat-treated for organics burnout and Biosilicate sintering (900ºC/3h). Scaffolds with approximately 5 mm (diameter) by 2 mm (thickness) were obtained. Then, the Biosilicate scaffolds were infiltrated with an F18 bioglass suspension (20% vol.) under vacuum and again sintered at 800ºC/3h. Before *in vitro* test, the scaffolds were sterilized at 180 ºC/3h in a laboratory drying oven.